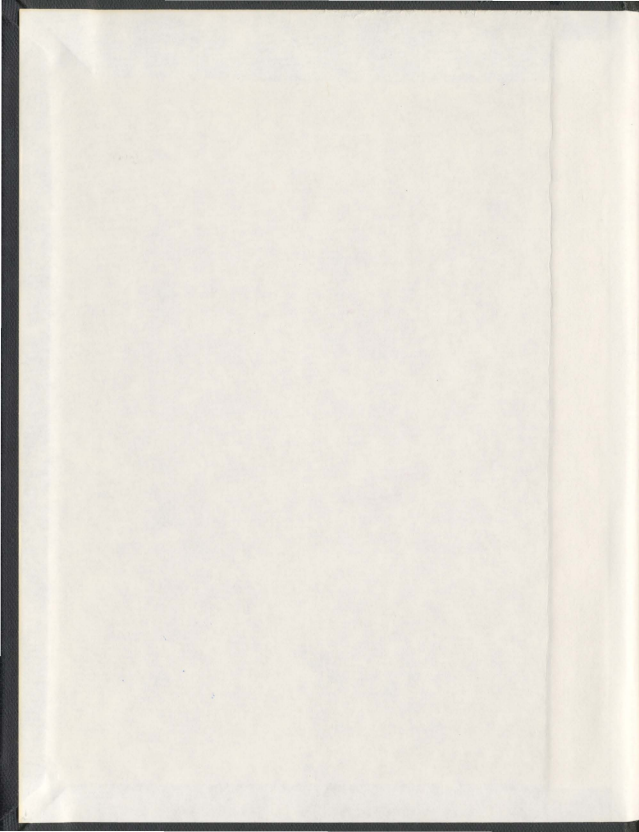
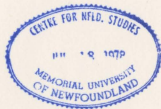


CONDUCTING POLYMERS, METAL OXIDES,
AND THEIR EFFECTS ON THE OXIDATION OF
ORGANIC FUELS AT Pt OR Pd

REZA BEIRAMZADEH MOGHADDAM



001311



**Conducting polymers, metal oxides, and their
effects on the oxidation of organic fuels at Pt
or Pd**

by

Reza Beiramzadeh Moghaddam

B.Sc., Urmia University, Urmia-Iran, 2003

M.Sc., K.N. Toosi University of Technology, Tehran-Iran, 2006

A thesis submitted to the School of Graduate Studies in partial
fulfillment of the requirements for the degree of Doctor of Philosophy

Department of Chemistry
Memorial University of Newfoundland
St. John's, Newfoundland, Canada

April 2012

Abstract

The ideas explored in this thesis originate from the significant role of the support material in the performance of anodes in organic fuel cells. This text describes a variety of approaches to provide insight into the synthesis, structure, and roles of various supports in organic fuel oxidation at Pt or Pd.

Potentiodynamic, potentiostatic, and galvanostatic regimes were used to polymerize pyrrole on carbon black (CB) electrodes. It was found that the electrochemical properties and structures of the CB/polypyrrole composites (PPCB) depended on the polymerization conditions. While potential-controlled polymerization regimes produced resistive PPCB films, constant current polymerization resulted in PPCB composites with high conductivity over a wide potential range.

Extended reaction zone anodes for formic acid (FA) oxidation were prepared by depositing Pd on polyaniline modified carbon fiber paper (CFP/PANI). It was shown that while a potentiodynamically deposited polymer support (CFP/PD-PANI) resulted in formation of smaller Pd nanoparticles, the activity of the resulting composite was inferior to anodes with either potentiostatically (CFP/P-PANI/Pd) or galvanostatically (CFP/G-PANI/Pd) prepared supports.

A methodology was developed to study support effects, based on the use of polyaniline (PANI) or various metal oxides (MOs) on glassy carbon (GC) as supports for organic fuel oxidation at Pt and Pd nanoparticles. Methanol oxidation at a GC/Ru oxide/Pt electrode was compared to GC/Pt, while a GC/PANI/Pt electrode did not show any enhancement. The same GC/PANI support (made in 0.1 M H₂SO₄), and also

GC/PANI electrodes made in two other media (CF_3COOH and $\text{CF}_3\text{SO}_3\text{H}$), coated with Pd nanoparticles gave lower onsets and higher FA oxidation currents than at GC/Pd, providing unambiguous evidence for effects of PANI on this reaction at Pd. The method was further extended to ethanol oxidation at Pt supported on various MOs, where InSn oxide/Pt, GC/Ru oxide/Pt, GC/Sn oxide/Pt, and GC/RuSn oxide/Pt electrodes were superior to GC/Pt at all potentials. Sn oxide was effective at low potentials ($E < +0.4$ V/SCE), resulting in higher activities of the Sn oxide-containing electrodes over this range. At more positive potentials GC/Ru oxide/Pt gave superior activity due to the effectiveness of Ru oxide for CO oxidation.

Acknowledgements

My greatest appreciation goes to my supervisor, Dr. Peter Pickup, whose knowledge, generosity, and patience made my time in his group a delightful and invaluable experience.

I would like to thank Dr. Sunil Pansare and Dr. Christopher Kozak for their input as part of supervisory committee.

I am grateful to NSERC, Defence Research and Development Canada, Tekion, the Department of Chemistry, and the School of Graduate Studies for financial support.

I thank my colleagues in the Pickup group for their assistance, Mr. Michael Shaffer for SEM experiments, Ms. Julie Collins for AFM training, Dr. Wanda Aylward for XRD analysis, and Dr. Louise Weaver at the University of New Brunswick for TEM images.

At last but not least, I wish to express my deepest gratitude to my parents, Nayyereh and Dariush, and my wife, Ameneh, for their endless encouragement and devotion.

Table of Contents

| | |
|---|------|
| Abstract..... | i |
| Acknowledgements..... | iii |
| Table of Contents..... | iv |
| List of Tables..... | x |
| List of Figures and Schemes..... | xi |
| List of Abbreviations..... | XXIV |
| Chapter 1. Introduction..... | 2 |
| 1.1. Fuel cells..... | 2 |
| 1.1.1. Classification of fuel cells..... | 4 |
| 1.1.2. Fuel cell reactions..... | 5 |
| 1.1.2.1. Hydrogen oxidation..... | 5 |
| 1.1.2.2. Methanol oxidation..... | 6 |
| 1.1.2.3. Formic acid oxidation..... | 6 |
| 1.1.2.4. Ethanol oxidation..... | 7 |
| 1.1.2.5. Oxygen reduction..... | 8 |
| 1.1.3. Catalysts..... | 10 |
| 1.1.4. Typical voltammetric observations for fuel cell reactions..... | 18 |

| | |
|--|----|
| 1.1.4.1. Electrochemistry of Pt..... | 18 |
| 1.1.4.2. Electrocatalytic oxidation of methanol at Pt..... | 19 |
| 1.1.4.3. Electrocatalytic oxidation of formic acid..... | 20 |
| 1.1.4.4. Electrocatalytic oxidation of ethanol at Pt..... | 22 |
| 1.1.5. Supports | 23 |
| 1.1.5.1. Carbon..... | 24 |
| 1.1.5.2. Conducting polymers..... | 25 |
| 1.1.5.3. Metals and metal oxides..... | 27 |
| 1.2. Scope and outline of this thesis..... | 28 |
| 1.3. Electrochemical techniques | 29 |
| 1.3.1. Cyclic voltammetry..... | 29 |
| 1.3.2. Chronoamperometry | 31 |
| 1.3.3. Electrochemical impedance spectroscopy | 31 |
| References..... | 37 |
| Chapter 2. Electrochemical impedance study of the polymerization of pyrrole on high surface area carbon electrodes | 48 |
| 2.1. Introduction..... | 48 |
| 2.2. Experimental..... | 51 |
| 2.2.1. Chemicals..... | 51 |

| | |
|--|------------|
| 2.2.2. Instrumentation | 51 |
| 2.2.3. Electrochemical polymerization of pyrrole | 52 |
| 2.3. Results and discussion | 53 |
| 2.3.1. Potentiodynamic polymerization | 53 |
| 2.3.2. Potentiostatic polymerization..... | 75 |
| 2.3.3. Galvanostatic polymerization | 84 |
| 2.4. Concluding remarks | 97 |
| References..... | 100 |
| Chapter 3. Electrocatalytic oxidation of formic acid at Pd nanoparticles incorporated into polyaniline modified carbon fibre paper..... | 107 |
| 3.1. Introduction..... | 107 |
| 3.2. Experimental | 111 |
| 3.2.1. Chemicals..... | 111 |
| 3.2.2. Electrochemical Instrumentation | 112 |
| 3.2.3. Working electrode preparation | 112 |
| 3.2.3.1. Electropolymerization of aniline..... | 112 |
| 3.2.3.2. Spontaneous deposition of Pd..... | 112 |
| 3.2.3.3. Drop coating of PANI films with Pd nanoparticle (Pd NP) solution..... | 113 |
| 3.2.4. Characterization of the working electrodes | 113 |

| | |
|---|-----|
| 3.3. Results and discussion | 115 |
| 3.3.1. Characterization of the CPF/PANI | 115 |
| 3.3.2. Characterization of the CPF/PANI/Pd _{SP} composites | 116 |
| 3.3.3. Formic acid oxidation at CPF/PANI/Pd _{SP} composites | 119 |
| 3.3.4. Formic acid oxidation at CPF/PANI/Pd _{NP} composites | 122 |
| 3.3.5. Impedance spectroscopy | 132 |
| 3.4. Concluding remarks | 138 |
| References | 140 |
| Chapter 4. Support effects on the oxidation of methanol at Pt nanoparticles | 145 |
| 4.1. Introduction | 145 |
| 4.2. Experimental | 147 |
| 4.2.1. Chemicals | 147 |
| 4.2.2. Preparation of Pt nanoparticles | 148 |
| 4.2.3. Working electrode preparation | 148 |
| 4.2.4. Instrumentation | 149 |
| 4.3. Results and discussion | 150 |
| 4.3.1. Characterization of the Pt nanoparticles | 150 |
| 4.3.2. Polyaniline supported Pt | 156 |
| 4.3.3. Ru oxide supported Pt | 160 |

| | |
|--|-----|
| 4.3.4. Mechanistic insights..... | 173 |
| 4.4. Concluding remarks..... | 175 |
| References..... | 176 |
| Chapter 5. Support effects on the oxidation of formic acid at Pd nanoparticles | 180 |
| 5.1. Introduction..... | 180 |
| 5.2. Experimental..... | 183 |
| 5.2.1. Chemicals..... | 183 |
| 5.2.2. Synthesis of Pd nanoparticles | 184 |
| 5.2.3. Preparation of working electrodes | 184 |
| 5.2.4. Instrumentation | 185 |
| 5.3. Results and discussion | 185 |
| 5.3.1. Characterization of the Pd nanoparticles | 185 |
| 5.3.2. Formic acid oxidation at Pd nanoparticles..... | 195 |
| 5.3.3. Mechanistic insights..... | 204 |
| 5.4. Concluding remarks | 205 |
| References..... | 207 |
| Chapter 6. Support effects on the oxidation of ethanol at Pt nanoparticles..... | 211 |
| 6.1. Introduction..... | 211 |
| 6.2. Experimental..... | 214 |

| | |
|--|-----|
| 6.2.1. Chemicals..... | 214 |
| 6.2.2. Preparation of Pt nanoparticles | 214 |
| 6.2.3. Working electrode preparation | 215 |
| 6.2.4. Instrumentation | 216 |
| 6.3. Results and discussion | 217 |
| 6.3.1. Characterization of the nanoparticles and electrodes..... | 217 |
| 6.3.2. Ethanol oxidation..... | 222 |
| 6.3.3. Mechanistic insights..... | 235 |
| 6.4. Concluding remarks | 240 |
| References | 242 |
| Chapter 7. Summary | 246 |
| References | 251 |
| Appendix..... | 252 |

List of Tables

| | |
|--|----|
| Table 2-1 Parameters from impedance data for the PPCB-cv electrodes..... | 67 |
| Table 2-2. Parameters from impedance data for a PPCB-cp electrode..... | 78 |
| Table 2-3. Parameters from impedance data for a PPCB-cc2 electrode..... | 88 |

List of Figures and Schemes

| | |
|---|----|
| Figure 1-1. Cyclic voltammogram of a Pt electrode (0.071 cm^2 ; CH Instruments) in 1 M H_2SO_4 at 100 mV s^{-1} | 18 |
| Figure 1-2. A typical voltammogram (10 mV s^{-1}) of ca. 0.1 mg cm^{-2} Pt nanoparticle (see section 4.2.2 for the preparation method) coated on a glassy carbon electrode in 0.1 M H_2SO_4 containing 0.2 M methanol..... | 20 |
| Figure 1-3. A typical voltammogram (10 mV s^{-1}) of ca. $10 \text{ }\mu\text{g cm}^{-2}$ Pt nanoparticles (see section 4.2.2 for the preparation method) coated on a glassy carbon electrode in 0.1 M H_2SO_4 containing 0.5 M formic acid. | 21 |
| Figure 1-4. A typical voltammogram (10 mV s^{-1}) of ca. $15 \text{ }\mu\text{g cm}^{-2}$ Pd nanoparticles (see section 5.2.2 for the preparation method) coated on a glassy carbon electrode in 0.1 M H_2SO_4 containing 0.5 M formic acid. | 22 |
| Figure 1-5. A typical voltammogram (10 mV s^{-1}) of ca. $5 \text{ }\mu\text{g cm}^{-2}$ Pt nanoparticles (see section 4.2.2 for the preparation method) coated on a glassy carbon electrode in 0.1 M H_2SO_4 containing 0.2 M ethanol..... | 23 |
| Scheme 1-1. Typical structures for polyaniline, polypyrrole, and polythiophene. | 26 |
| Figure 1-6. Voltammogram (20 mV s^{-1}) of a Pt disk electrode (0.05 cm^2) in 1 M KNO_3 containing 0.01 M $\text{K}_3\text{Fe}(\text{CN})_6$ | 29 |
| Figure 1-7. Typical waveform (A) and waveshape (B) for a Pt disk electrode (0.05 cm^2) in 1 M KNO_3 containing 0.01 M $\text{K}_3\text{Fe}(\text{CN})_6$ | 30 |

| | |
|---|----|
| Figure 1-8. A simulated (ZView2, Scribner Associates Inc.) Nyquist plot and the equivalent circuit (inset) used for the simulation: $R_{\Omega} = 6 \Omega$; $R_{CT} = 1000 \Omega$; $C_{DL} = 1.31 \times 10^{-5} \text{ S s}$ | 33 |
| Figure 1-9. A simulated (ZView2, Scribner Associates Inc.) Nyquist plot displaying Warburg-type and capacitive impedances; $R_{\Omega} = 6 \Omega$; $C_{DL} = 1.31 \times 10^{-2} \text{ S s}$; $R_L = 50 \Omega$; $C_L = 10 \text{ mF}$ | 34 |
| Figure 1-10. Equivalent circuit compatible with the Nyquist plot shown in figure 1-9. .. | 35 |
| Figure 1-11. Capacitance as a function of the real impedance for the Nyquist data shown in figure 1-9..... | 35 |
| Figure 2-1. Schematic diagrams of two of the limiting structures possible for the electrodeposition of polypyrrole on a carbon black layer. A: Uniform deposition over the carbon black (CB) particles; B: Deposition on the outer surface of the CB layer..... | 50 |
| Figure 2-2. Polymerization voltammograms (50 mV s^{-1}) for 0.5 M pyrrole in 0.5 M $\text{NaClO}_4(\text{aq})$ at a bare GC electrode..... | 54 |
| Figure 2-3. Polymerization voltammograms (50 mV s^{-1}) for 0.5 M pyrrole in 0.5 M $\text{NaClO}_4(\text{aq})$ at a CB-coated GC electrode. | 55 |
| Figure 2-4. SEM image (cross sectional/ 45° view) for a CB coated GC electrode ($\sim 1 \text{ mg cm}^{-2}$)..... | 57 |
| Figure 2-5. Comparative CVs at 200 mV s^{-1} of the PPCB-cv2, PPCB-cv4, PPCB-cv6 and PPCB-cv8 electrodes in 0.5 M $\text{NaClO}_4(\text{aq})$ | 58 |
| Figure 2-6. Cyclic voltammograms for a PPCB-cv8 electrode at various potential sweep rates..... | 60 |

| | |
|--|----|
| Figure 2-7. Nyquist profiles recorded at $E = +0.3$ V in 0.5 M $\text{NaClO}_4(\text{aq})$ for the PPCB-cv2, PPCB-cv4, PPCB-cv6 and PPCB-cv8 electrodes; inset: expanded high frequency region. | 62 |
| Figure 2-8. Capacitance plots (series capacitance as a function of the real impedance) recorded at $E = +0.3$ V in 0.5 M $\text{NaClO}_4(\text{aq})$ for the PPCB-cv2, PPCB-cv4, PPCB-cv6 and PPCB-cv8 electrodes. | 63 |
| Figure 2-9. Equivalent circuit used to fit the impedance data. | 65 |
| Figure 2-10. Comparison of experimental and simulated (ZView2, Scribner Associates Inc.) impedance data for PPCB-cv4 at -0.1 V. The fitting parameters were: $R_S = 43.3 \Omega$, $R_{CT} = 251 \Omega$, $\text{CPE-T}(Q_0 \text{ or } Y_0) = 5.7 \times 10^{-5} \text{ S s}^{0.67}$, $\text{CPE-P}(\alpha \text{ or } n) = 0.67$, $R_L = 552 \Omega$, $C_L = 6.6 \text{ mF}$ and $W-P = 0.42$ | 66 |
| Figure 2-11. Nyquist plot for a polypyrrole coated glassy carbon electrode at +0.1 V in 0.5 M $\text{NaClO}_4(\text{aq})$ | 69 |
| Figure 2-12. Nyquist plot for a carbon black coated glassy carbon electrode at +0.1 V in 0.5 M $\text{NaClO}_4(\text{aq})$ | 71 |
| Figure 2-13. SEM images of a CB coated electrode (A and B) and similar electrodes coated with polypyrrole by using 2 (C; PPCB-cv2) and 6 (D; PPCB-cv6) polymerization cycles. | 73 |
| Figure 2-14. Typical cyclic voltammograms of a PPCB-cp electrode recorded at various potential sweep rates in 0.5 M NaClO_4 | 74 |
| Figure 2-15. Complex-plane plots for a PPCB-cp electrode in 0.5 M NaClO_4 at various dc-offset potentials; inset: expanded high frequency region. | 76 |

| | |
|---|----|
| Figure 2-16. Series capacitance as a function of the real impedance for a PPCB-cp electrode in 0.5 M NaClO ₄ at various dc-offset potentials. | 79 |
| Figure 2-17. Typical cyclic voltammograms of a PPCB-pp electrode recorded at various potential sweep rates in 0.5 M NaClO ₄ | 81 |
| Figure 2-18. Complex-plane plots for a PPCB-pp electrode in 0.5 M NaClO ₄ at various dc-offset potentials; capacitance profiles (inset)..... | 82 |
| Figure 2-19. Scanning electron micrographs for the PPCB-cp and PPCB-pp composite films. | 83 |
| Figure 2-20. Cyclic voltammograms of a PPCB-cc2 electrode in 0.5 M NaClO ₄ | 85 |
| Figure 2-21. Complex-plane (Nyquist) profiles for the PPCB-cc2 electrode at +0.3, -0.1, -0.3, -0.5 V. | 87 |
| Figure 2-22. Series capacitance as a function of real impedance for the PPCB-cc2 electrode at +0.3, -0.1, -0.3, -0.5 V..... | 89 |
| Figure 2-23. Representative SEM images for a PPCB-cc2. | 91 |
| Figure 2-24. Cyclic voltammograms in 0.5 M NaClO ₄ at 200 mV s ⁻¹ for the PPCB-cc1, PPCB-cc2, and PPCB-cc3 electrodes. | 92 |
| Figure 2-25. SEM images for the PPCB-cc1 and PPCB-cc3 electrodes. | 93 |
| Figure 2-26. Complex-plane diagrams in 0.5 M NaClO ₄ at +0.3 V for the PPCB-cc1, PPCB-cc2, and PPCB-cc3 electrodes. | 94 |
| Figure 2-27. Capacitance plots for the PPCB-cc1, PPCB-cc2, PPCB-cc3, and PPCB-cv2 electrodes at +0.3 V. | 96 |

| | |
|--|-----|
| Figure 3-1. Cyclic voltammograms (10 mV s^{-1}) of CFP/PD-PANI, CFP/P-PANI, and CFP/G-PANI electrodes in $0.5 \text{ M H}_2\text{SO}_4$ | 114 |
| Figure 3-2. SEM images of the CFP/PD-PANI, CFP/G-PANI, and CFP/P-PANI electrodes. | 115 |
| Figure 3-3. Cyclic voltammograms (10 mV s^{-1}) of CFP/PD-PANI/Pd, CFP/P-PANI/Pd, and CFP/G-PANI/Pd electrodes in $0.5 \text{ M H}_2\text{SO}_4$ | 117 |
| Figure 3-4. TEM images of PANI/Pd _{SP} deposits scraped from CFP/PD-PANI/Pd _{SP} , CFP/G-PANI/Pd _{SP} , and CFP/P-PANI/Pd _{SP} electrodes. | 118 |
| Figure 3-5. Cyclic voltammograms (10 mV s^{-1}) of CFP/PD-PANI/Pd _{SP} , CFP/P-PANI/Pd _{SP} , and CFP/G-PANI/Pd _{SP} electrodes in $0.5 \text{ M H}_2\text{SO}_4$ containing 0.5 M HCOOH | 119 |
| Figure 3-6. Chronoamperometric responses at $E = -0.2 \text{ (A)}$, -0.1 (B) , 0 (C) , and $+0.1 \text{ (D)}$ V for CFP/PD-PANI/Pd _{SP} , CFP/P-PANI/Pd _{SP} , and CFP/G-PANI/Pd _{SP} electrodes in $0.5 \text{ M H}_2\text{SO}_4$ containing 0.5 M FA | 121 |
| Figure 3-7. Cyclic voltammograms (10 mV s^{-1}) of CFP/PD-PANI/Pd _{NP} , CFP/P-PANI/Pd _{NP} , and CFP/G-PANI/Pd _{NP} electrodes in $0.5 \text{ M H}_2\text{SO}_4$ and in the absence (A) and presence (B) of 0.5 M FA | 124 |
| Figure 3-8. Comparative voltammetric responses of CFP/G-PANI/Pd _{SP} and CFP/G-PANI/Pd _{NP} electrodes at 10 mV s^{-1} in $0.5 \text{ M H}_2\text{SO}_4$ containing 0.5 M FA | 126 |
| Figure 3-9. Chronoamperometric responses at $E = -0.1 \text{ (A)}$, 0 (B) , and $+0.1 \text{ V (C)}$ for CFP/PD-PANI/Pd _{NP} , CFP/P-PANI/Pd _{NP} , and CFP/G-PANI/Pd _{NP} electrodes in $0.5 \text{ M H}_2\text{SO}_4$ containing 0.5 M FA | 127 |

| | |
|--|-----|
| Figure 3-10. Cyclic voltammograms of CFP/Pd _{NP} , CFP/G-PANI/Pd _{NP} , and CFP/PD-PANI/Pd _{NP} in the absence (A) and presence (B) of 0.5 M FA in 0.5 M H ₂ SO ₄ at a scan rate of 10 mV s ⁻¹ | 129 |
| Figure 3-11. Chronoamperometric responses of CFP/Pd _{NP} , CFP/G-PANI/Pd _{NP} , CFP/P-PANI/Pd _{NP} , and CFP/PD-PANI/Pd _{NP} in 0.5 M H ₂ SO ₄ containing 0.5 M FA at +0.1 V. 131 | |
| Figure 3-12. Complex plane impedance plots at +0.1 V for PD-PANI, P-PANI, and G-PANI coated CFP electrodes in 0.5 M H ₂ SO ₄ | 133 |
| Figure 3-13. Complex plane impedance plots at -0.1 V for PD-PANI, P-PANI, and G-PANI coated CFP electrodes in 0.5 M H ₂ SO ₄ (inset: expanded high frequency region) 134 | |
| Figure 3-14. Series capacitance plots for CFP/PD-PANI (A), CFP/P-PANI (B), and CFP/G-PANI (C) coated CFP electrode in 0.5 M H ₂ SO ₄ . Potentials are vs. SCE. | 136 |
| Figure 4-1. Transmission electron microscopy images of colloidal Pt nanoparticles (deposited on a Cu grid)..... | 147 |
| Figure 4-2. Voltammogram of a GC/Pt electrode in 0.1 M H ₂ SO ₄ at a potential sweep rate of 10 mV s ⁻¹ | 151 |
| Figure 4-3. Scanning electron microscopy images for 10 μg cm ⁻² Pt nanoparticles + 5% Nafion coated on a GC plate. | 152 |
| Figure 4-4. Atomic force microscopy (B; 10 × 10 μm × 128 nm) images of ca. 10 μg cm ⁻² of Pt nanoparticles + 5% Nafion on a GC plate..... | 153 |
| Figure 4-5. Cyclic voltammograms (10 mV s ⁻¹) of a GC/Pt electrode in 0.1 M H ₂ SO ₄ in the absence (solid line) and presence (dashed line) of 0.005 M CuSO ₄ | 154 |

| | |
|---|-----|
| Figure 4-6. Cyclic voltammograms (10 mV s^{-1}) of GC (solid line) and GC/PANI (dashed line) electrodes coated with ca. $10 \mu\text{g cm}^{-2}$ of Pt nanoparticles in $0.1 \text{ M H}_2\text{SO}_4$. | 157 |
| Figure 4-7. Cyclic voltammograms (10 mV s^{-1}) of a GC/PANI/Pt electrode in $0.1 \text{ M H}_2\text{SO}_4$ in the absence (solid line) and presence (dashed line) of 0.005 M CuSO_4 . | 158 |
| Figure 4-8. Multiple cycle voltammograms (10 mV s^{-1}) of GC (solid line; 10 cycles) and GC/PANI (dashed line; cycles 1 and 15 are shown) electrodes coated with ca. $10 \mu\text{g cm}^{-2}$ of Pt nanoparticles in $0.1 \text{ M H}_2\text{SO}_4$ containing 0.2 M methanol. | 159 |
| Figure 4-9. Cyclic voltammograms (10 mV s^{-1}) of GC (light) and GC/Ru oxide (heavy) electrodes coated with ca. $10 \mu\text{g cm}^{-2}$ of Pt nanoparticles in $0.1 \text{ M H}_2\text{SO}_4$. | 161 |
| Figure 4-10. Cyclic voltammograms (10 mV s^{-1}) of a GC/Ru oxide/Pt electrode in $0.1 \text{ M H}_2\text{SO}_4$ in the absence (solid line) and presence (dashed line) of 0.005 M CuSO_4 . | 162 |
| Figure 4-11. Cyclic voltammograms (10 mV s^{-1}) of GC (light) and GC/Ru oxide (heavy) electrodes coated with ca. $10 \mu\text{g cm}^{-2}$ of Pt nanoparticles in $0.1 \text{ M H}_2\text{SO}_4$ containing 0.2 M methanol. | 164 |
| Figure 4-12. (A) Cyclic voltammograms (10 mV s^{-1}) of a GC/Ru oxide electrode in $0.1 \text{ M H}_2\text{SO}_4$; (B) Overlaid CVs of a GC/Ru oxide electrode in $0.1 \text{ M H}_2\text{SO}_4$ in the presence (dashed line) and absence of 0.2 M methanol (solid line). | 166 |
| Figure 4-13. Chronoamperometric responses of GC/Pt and GC/Ru oxide/Pt at $+0.2 \text{ V}$ in $0.1 \text{ M H}_2\text{SO}_4$ containing 0.2 M methanol. | 168 |
| Figure 4-14. Chronoamperometric responses of GC/Pt and GC/Ru oxide/Pt at $+0.3 \text{ V}$ in $0.1 \text{ M H}_2\text{SO}_4$ containing 0.2 M methanol. | 169 |

| | |
|---|-----|
| Figure 4-15. Chronoamperometric responses of GC/Pt and GC/Ru oxide/Pt at +0.4 V in 0.1 M H ₂ SO ₄ containing 0.2 M methanol..... | 170 |
| Figure 4-16. Chronoamperometric responses of GC/Pt and GC/Ru oxide/Pt at +0.5 (A) and +0.6 (B) in 0.1 M H ₂ SO ₄ containing 0.2 M methanol..... | 171 |
| Figure 4-17. Chronoamperometric responses of GC/Pt and GC/Ru oxide/Pt at +0.85 (A) and +0.95 (B) V in 0.1 M H ₂ SO ₄ containing 0.2 M methanol..... | 172 |
| Figure 5-1. Transmission electron microscopy images for Pd nanoparticles coated on a Cu grid..... | 183 |
| Figure 5-2. SEM images of a GC plate coated with ca. 5.4 μg cm ⁻² of Pd nanoparticles + Nafion..... | 186 |
| Figure 5-3. AFM (B; 10 × 10 μm × 94 nm) images of ca. 5.4 μg cm ⁻² of Pd nanoparticles + Nafion on GC..... | 188 |
| Figure 5-4. Cyclic voltammograms (10 mV s ⁻¹) in 0.1 M H ₂ SO ₄ of a GC electrode coated with ca. 5.4 μg cm ⁻² of Pd nanoparticles..... | 189 |
| Figure 5-5. Cyclic voltammogram (10 mV s ⁻¹) of a GC/Pd electrode in 0.1 M H ₂ SO ₄ in the presence (solid line) and absence (dashed line) of 0.005 M CuSO ₄ | 190 |
| Figure 5-6. Cyclic voltammograms (10 mV s ⁻¹) in 0.1 M H ₂ SO ₄ of GC, GC/PANI-CF ₃ SO ₃ H, GC/PANI-SO ₄ , and GC/PANI-CF ₃ COOH electrodes coated with ca. 5.4 μg cm ⁻² of Pd nanoparticles..... | 192 |
| Figure 5-7. Cyclic voltammograms (10 mV s ⁻¹) of GC/PANI-SO ₄ /Pd (A) GC/PANI-CF ₃ SO ₃ H (B), and GC/PANI-CF ₃ COOH (C) electrodes in 0.1 M H ₂ SO ₄ in the presence (solid line) and absence (dashed line) of 0.005 M CuSO ₄ | 193 |

| | |
|---|-----|
| Figure 5-8. Cyclic voltammograms (10 mV s^{-1}) in $0.1 \text{ M H}_2\text{SO}_4 + 0.5 \text{ M FA}$ of GC, GC/PANI-CF ₃ SO ₃ H, GC/PANI-SO ₄ , and GC/PANI-CF ₃ COOH electrodes coated with ca. $5.4 \mu\text{g cm}^{-2}$ of Pd nanoparticles..... | 196 |
| Figure 5-9. Chronoamperometry at -0.1 V for GC/Pd, GC/PANI-CF ₃ COOH/Pd, GC/PANI-CF ₃ SO ₃ H/Pd, and GC/PANI-SO ₄ /Pd electrodes in $0.1 \text{ M H}_2\text{SO}_4$ containing 0.5 M FA | 198 |
| Figure 5-10. Chronoamperometry at 0 V for GC/Pd, GC/PANI-CF ₃ COOH/Pd, GC/PANI-CF ₃ SO ₃ H/Pd, and GC/PANI-SO ₄ /Pd electrodes in $0.1 \text{ M H}_2\text{SO}_4$ containing 0.5 M FA | 199 |
| Figure 5-11. Chronoamperometry at $+0.1 \text{ V}$ for GC/Pd, GC/PANI-CF ₃ COOH/Pd, GC/PANI-CF ₃ SO ₃ H/Pd, and GC/PANI-SO ₄ /Pd electrodes in $0.1 \text{ M H}_2\text{SO}_4$ containing 0.5 M FA | 200 |
| Figure 5-12. Normalized Chronoamperometric profiles at -0.1 V for GC/Pd, GC/PANI-CF ₃ COOH/Pd, GC/PANI-CF ₃ SO ₃ H/Pd, and GC/PANI-SO ₄ /Pd electrodes in $0.1 \text{ M H}_2\text{SO}_4$ containing 0.5 M FA | 201 |
| Figure 5-13. Normalized Chronoamperometric profiles at 0 V for GC/Pd, GC/PANI-CF ₃ COOH/Pd, GC/PANI-CF ₃ SO ₃ H/Pd, and GC/PANI-SO ₄ /Pd electrodes in $0.1 \text{ M H}_2\text{SO}_4$ containing 0.5 M FA | 202 |
| Figure 5-14. Normalized Chronoamperometric profiles at $+0.1 \text{ V}$ for GC/Pd, GC/PANI-CF ₃ COOH/Pd, GC/PANI-CF ₃ SO ₃ H/Pd, and GC/PANI-SO ₄ /Pd electrodes in $0.1 \text{ M H}_2\text{SO}_4$ containing 0.5 M FA | 203 |
| Figure 6-1. SEM image of ca. $4.3 \mu\text{g cm}^{-2}$ of Pt nanoparticles + Nafion on GC (A) and ITO (B) plates..... | 217 |

| | |
|--|-----|
| Figure 6-2. AFM ($2 \times 2 \mu\text{m} \times 74 \text{ nm}$) image of <i>ca.</i> $4.3 \mu\text{g cm}^{-2}$ of Pt nanoparticles + Nafion on GC..... | 218 |
| Figure 6-3. Cyclic voltammograms (10 mV s^{-1}) in $0.1 \text{ M H}_2\text{SO}_4$ of GC/Ru oxide, GC/Sn oxide and GC/Ru _{0.85} Sn _{0.15} oxide electrodes. | 219 |
| Figure 6-4. Cyclic voltammograms (10 mV s^{-1}) in $0.1 \text{ M H}_2\text{SO}_4$ of GC, ITO, GC/Ru oxide, GC/Sn oxide and GC/Ru _{0.85} Sn _{0.15} oxide electrodes coated with $4.3 \mu\text{g cm}^{-2}$ of Pt nanoparticles. | 221 |
| Figure 6-5. Cyclic voltammogram (10 mV s^{-1} ; 1st scan solid, 2nd scan dashed) in $0.1 \text{ M H}_2\text{SO}_4$ containing 0.2 M ethanol of a GC electrode coated with $4.3 \mu\text{g cm}^{-2}$ of Pt nanoparticles. | 222 |
| Figure 6-6. First anodic scans of cyclic voltammograms (10 mV s^{-1}) for GC/Pt, ITO/Pt, GC/Ru oxide/Pt, GC/Sn oxide/Pt and GC/Ru _{0.85} Sn _{0.15} oxide/Pt electrodes in $0.1 \text{ M H}_2\text{SO}_4$ containing 0.2 M ethanol. | 224 |
| Figure 6-7. Second anodic scans of cyclic voltammograms (10 mV s^{-1}) for GC/Pt, ITO/Pt, GC/Ru oxide/Pt, GC/Sn oxide/Pt and GC/Ru _{0.85} Sn _{0.15} oxide/Pt electrodes in $0.1 \text{ M H}_2\text{SO}_4$ containing 0.2 M ethanol. | 227 |
| Figure 6-8. Chronoamperometry at 0 V for for GC/Pt, ITO/Pt, GC/Ru oxide/Pt, GC/Sn oxide/Pt and GC/Ru _{0.85} Sn _{0.15} oxide/Pt electrodes in $0.1 \text{ M H}_2\text{SO}_4$ containing 0.2 M ethanol..... | 228 |
| Figure 6-9. Chronoamperometry at $+0.1 \text{ V}$ for for GC/Pt, ITO/Pt, GC/Ru oxide/Pt, GC/Sn oxide/Pt and GC/Ru _{0.85} Sn _{0.15} oxide/Pt electrodes in $0.1 \text{ M H}_2\text{SO}_4$ containing 0.2 M ethanol..... | 230 |

| | |
|---|-----|
| Figure 6-10. Chronoamperometry at +0.2 V for for GC/Pt, ITO/Pt, GC/Ru oxide/Pt, GC/Sn oxide/Pt and GC/Ru _{0.85} Sn _{0.15} oxide/Pt electrodes in 0.1 M H ₂ SO ₄ containing 0.2 M ethanol..... | 231 |
| Figure 6-11. Chronoamperometry at +0.3 V for GC/Pt, ITO/Pt, GC/Ru oxide/Pt, GC/Sn oxide/Pt and GC/Ru _{0.85} Sn _{0.15} oxide/Pt electrodes in 0.1 M H ₂ SO ₄ containing 0.2 M ethanol..... | 233 |
| Figure 6-12. Chronoamperometry at +0.4 V for for GC/Pt, ITO/Pt, GC/Ru oxide/Pt, GC/Sn oxide/Pt and GC/Ru _{0.85} Sn _{0.15} oxide/Pt electrodes in 0.1 M H ₂ SO ₄ containing 0.2 M ethanol..... | 234 |
| Figure A-1. Comparison of experimental and simulated (ZView2, Scribner Associates Inc.) impedance data for PPCB-cv2 at -0.1 V. | 252 |
| Figure A-2. Comparison of experimental and simulated (ZView2, Scribner Associates Inc.) impedance data for PPCB-cv2 at +0.3 V..... | 253 |
| Figure A-3. Comparison of experimental and simulated (ZView2, Scribner Associates Inc.) impedance data for PPCB-cv4 at +0.3 V..... | 254 |
| Figure A-4. Comparison of experimental and simulated (ZView2, Scribner Associates Inc.) impedance data for PPCB-cv6 at -0.1 V. | 255 |
| Figure A-5. Comparison of experimental and simulated (ZView2, Scribner Associates Inc.) impedance data for PPCB-cv6 at +0.3 V..... | 256 |
| Figure A-6. Comparison of experimental and simulated (ZView2, Scribner Associates Inc.) impedance data for PPCB-cv8 at -0.1 V. | 257 |

| | |
|---|-----|
| Figure A-7. Comparison of experimental and simulated (ZView2, Scribner Associates Inc.) impedance data for PPCB-cv8 at +0.3 V..... | 258 |
| Figure A-8. Comparison of experimental and simulated (ZView2, Scribner Associates Inc.) impedance data for PPCB-cp at -0.3 V. | 259 |
| Figure A-9. Comparison of experimental and simulated (ZView2, Scribner Associates Inc.) impedance data for PPCB-cp at -0.1 V. | 260 |
| Figure A-10. Comparison of experimental and simulated (ZView2, Scribner Associates Inc.) impedance data for PPCB-cp at +0.3 V..... | 261 |
| Figure A-11. Comparison of experimental and simulated (ZView2, Scribner Associates Inc.) impedance data for PPCB-cc2 at -0.5 V..... | 262 |
| Figure A-12. Comparison of experimental and simulated (ZView2, Scribner Associates Inc.) impedance data for PPCB-cc2 at -0.3 V..... | 263 |
| Figure A-13. Comparison of experimental and simulated (ZView2, Scribner Associates Inc.) impedance data for PPCB-cc2 at -0.1 V..... | 264 |
| Figure A-14. Comparison of experimental and simulated (ZView2, Scribner Associates Inc.) impedance data for PPCB-cc2 at +0.3 V..... | 265 |
| Figure A-15. Multiple scan CVs (10 mV s^{-1}) for a GC/Pt electrode in 0.1 M H_2SO_4 containing 0.2 M ethanol. | 266 |
| Figure A-16. Multiple scan CVs (10 mV s^{-1}) for a GC/Ru oxide/Pt electrode in 0.1 M H_2SO_4 containing 0.2 M ethanol..... | 267 |
| Figure A-17. Multiple scan CVs (10 mV s^{-1}) for an ITO/Pt electrode in 0.1 M H_2SO_4 containing 0.2 M ethanol. | 268 |

| | |
|--|-----|
| Figure A-18. Multiple scan CVs (10 mV s^{-1}) for a GC/Sn oxide/Pt electrode in 0.1 M H_2SO_4 containing 0.2 M ethanol..... | 269 |
| Figure A-19. Multiple scan CVs (10 mV s^{-1}) for a GC/ $\text{Ru}_{0.85}\text{Sn}_{0.15}$ oxide/Pt electrode in 0.1 M H_2SO_4 containing 0.2 M ethanol..... | 270 |

List of Abbreviations

- R_S (or R_Ω): uncompensated ohmic resistance
- R_{CT} : charge transfer resistance
- R_L : layer resistance
- C_{DL} : double layer capacitance
- C_L : layer capacitance
- Z : impedance
- Z_{real} : real impedance
- Z_{imag} : imaginary impedance
- C_{Series} : series capacitance
- W_R : Warburg-type resistance (45° line)
- CPE: constant phase element
- Q_σ : solitary constant phase element
- Y_σ : conductance
- Ω : ohm
- ω : radial frequency
- E: potential
- V: volt (potential unit)
- V_m : voltage, maximum voltage (sinusoidal wave amplitude)
- I_m : maximum current (sinusoidal wave amplitude)
- I: current
- A: ampere (current unit)

t: time

s: second (time unit)

v: sinusoidal potential

i: sinusoidal current

f: frequency

θ : phase shift (between the voltage and the current)

RHE: Reversible Hydrogen Electrode

SCE: Saturated Calomel Electrode

Chapter 1

Introduction

Chapter 1. Introduction

1.1. Fuel cells

On account of the large natural resources and key role of fossil fuels in the advancement of technology, they have served as the main sources of energy for centuries. In 2010, the US Energy Information Administration reported an 85% contribution of fossil fuels to primary energy consumption between 2004 and 2008.¹ As such, oil as the most useful fossil fuel is being increasingly used by both developed and developing countries.² However, although fossil fuels are attractive materials because of their high energy content and ease of use, there are several major drawbacks associated with them. First of all, they are by definition not renewable on a practical timescale (i.e. their renewal takes centuries). In addition, a significant portion of the energy produced by their oxidation is converted to heat; that is, the efficiency of a fossil fuel-driven combustion machine typically cannot exceed 20-30% at best. Furthermore, the products of the oxidation of fossil fuels are often harmful to the environment and can accelerate undesirable modern-life processes such as the greenhouse effect and global warming.³

Hence, there has always been a great need to replace fossil fuels with more renewable, efficient, and environment-friendly sources of energy. In this regard, over the past decades many countries have attempted to replace fossil fuels with alternative sources of energy to meet these requirements.² Fuel cells,^{4, 5} capacitors,^{5, 6} and batteries⁵ have gained much attention as components of renewable energy strategies. As a result of their unique properties, fuel cells have attracted a greater deal of attention in this

category. Fuel cells are interesting devices in that their common reactants (H_2 , CH_3OH , C_2H_5OH , and $HCOOH$) are renewable through microbial processes on biomass, and they can work very efficiently (close to 100% energy efficiency in theory), and theoretically they can produce only H_2O (and CO_2 for carbon-containing fuels). Moreover, as fuel cells can operate over a longer period of time (e.g. thousands of hours), they can provide much larger energy densities than capacitors and batteries. Nevertheless, having all the above advantages, fuel cells produce limited power densities, and also they are rather expensive devices. Therefore, it is obvious why a large body of research has been increasingly focussed on studying catalysts, electrolytes, supports, etc. that form fuel cells, all of which have been targeted not only to lower the cost of fuel cells but also to improve their performances.^{4,5}

In general, fuel cells are efficient devices that can continuously convert chemical energy of a fuel into a usable form of electrical energy.⁴ In a typical view, a fuel cell consists of three main parts, the anode and cathode between which there is an electrolyte.⁵ This electrolyte is most commonly a proton exchange membrane (PEM) that not only serves to transport protons between the anode and cathode but also separates the two electrodes and their reactants.⁵ An oxidation reaction takes place at the anode releasing electrons that are drawn to the cathode through an external circuit.⁵ Simultaneously, protons produced during the anodic reaction will pass through the electrolyte to the cathode where they participate in a reduction reaction (e.g. oxygen reduction).⁵

1.1.1. Classification of fuel cells

Generally, fuel cells can be classified as direct and indirect. In direct fuel cells, fuel is directly fed to the anode. Depending on the temperature of operation, direct fuel cells are further subcategorized as low (25°C-100°C), intermediate (100 °C-500 °C), and high (500 °C-1000 °C) temperature fuel cells. The other class comprises indirect fuel cells in which an external source such as hydrocarbons has to be reformed or otherwise converted to a simpler and more reactive compound (normally hydrogen) for introduction into the fuel cell. There is also another classification method based on the type of the electrolyte. Herein, fuel cells can be further classified as proton exchange membrane fuel cells (PEMFCs), alkaline fuel cells (AFCs), direct methanol fuel cells (DMFCs), phosphoric acid fuel cells (PAFCs), molten carbonate fuel cells (MCFCs), and solid oxide fuel cell (SOFC).^{4, 7-11} Only PEM fuel cells are considered and discussed in this thesis.

The other classification can be envisaged based on the injected fuel. Here, H₂,^{2, 4} methanol,¹¹⁻¹³ ethanol,^{4, 8} and formic acid^{4, 10} are the most commonly-used fuels. Each of these fuels has advantages and disadvantages; H₂-fed fuel cells give impressive energy and power densities but H₂ is a hazardous molecule (i.e. highly explosive), and safe transportation and storage of which are problematic.^{2, 4} Methanol is easy to store and transport and gives good energy and power densities but it is highly combustible and poisonous. Furthermore, fuel crossover (undesirable crossover of the fuel from the anode through the proton exchange membrane to the cathode), which is a common source of lowering efficiency, is highest in DMFCs.⁸ In contrast, ethanol oxidation is a 12-electron

process and does produce higher energy densities than methanol oxidation (6-electron process) and it is safe in transportation and non-toxic. However, although fuel crossover is lower than DMFCs, direct ethanol fuel cells (DEFCs) have lower efficiencies.⁸ More recently, formic acid fuel cells (FAFCs) were introduced as potential alternatives to overcome some of the drawbacks of the H₂-fed and alcohol-based fuel cells.¹⁰ In fact, formic acid is not highly combustible, gives acceptable energy and power densities, and is easy to store and transport. However, formic acid is very corrosive and hazardous in case of inhalation and skin contact.¹⁰

1.1.2. Fuel cell reactions

In this section, general mechanisms for the oxidation (hydrogen, methanol, formic acid, and ethanol) and reduction (oxygen) of commonly used reactants are provided.

1.1.2.1. Hydrogen oxidation

The hydrogen oxidation reaction (HOR) is the central reaction at the anode of a H₂-fed PEM fuel cell. Owing to the fast kinetics of the HOR at Pt, this reaction typically contributes only a small fraction of the overall polarization of a H₂ fuel cell. The HOR at Pt¹⁴⁻¹⁶ catalysts initiates through dissociative adsorption of H₂ molecules (eq. 1-1) and/or partial oxidation of H₂ (eq. 1-2).



These parallel reactions, which are the rate limiting steps, are followed by a fast charge transfer step, eq. 1-3.



Reactions 1-1 through 1-3 are well-known as the Tafel, Heyrovsky, and Volmer reactions, respectively. Therefore, the two pathways for the HOR can be described as Tafel-Volmer and Tafel-Heyrovsky reactions.

1.1.2.2. Methanol oxidation

The methanol oxidation reaction (MOR) in acidic media and at noble metals (e.g. Pt) proceeds through a preliminary decomposition step (eq. 1-5) which follows the electroless adsorption of methanol at Pt sites, eq. 1-4.^{13, 17, 18}



The Pt-CO_{ads} species, which stands for an adsorbed CO intermediate at a Pt site, can be further oxidized to CO₂, equations 1-6 and 1-7.^{17, 18}



Reactions 1-6 and 1-7 require high potentials to occur; that is, oxidative removal of the adsorbed CO, eq. 1-6, occurs at $E > +0.6$ V (vs. RHE), parallel to the catalytic oxidation of CO in the presence of the PtO species formed at high potentials.

1.1.2.3. Formic acid oxidation

Formic acid oxidation can be pictured as a dual pathway reaction. The desirable pathway which is the direct oxidation of formic acid proceeds through a dehydrogenation reaction during which no poisoning species are formed, eq. 1-8.^{10, 19}

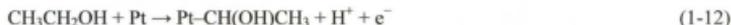


On the other hand, the other common pathway includes a preliminary dehydration step, eq. 1-9, which produces a blocking CO_{ads} intermediate at the catalyst sites. The CO_{ads} will be oxidized yielding CO_2 gas as the final product, eq. 1-10.^{10, 19}



1.1.2.4. Ethanol oxidation

In the ethanol oxidation reaction (EOR), ethanol dissociates to form various $-\text{CH}_x$ and oxygen containing species, equations 1-13 and 1-14, following its oxidative adsorption at the reaction sites (i.e. Pt), equations 1-11 and 1-12.²⁰⁻²³



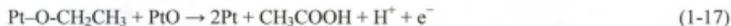
The EOR is continued by oxidation of the adsorbed Pt-CH_x and $\text{Pt-CH}_y\text{O}$ species to adsorbed CO (e.g. eq. 1-15) and then to CO_2 (eq. 1-16) as the final reaction product.²¹⁻

23



Recently, Wieckowski *et al.*²³ employed potentiodynamic sum-frequency generation (SFG) spectroscopy to study the reaction pathways for ethanol oxidation at polycrystalline Pt. They showed that adsorbed CO was the dominant intermediate at E <

+0.4 V (vs. Ag/AgCl), after which oxidative removal of the adsorbed CO and the oxidation of ethanol to acetate were active. Thus in the presence of the excess H⁺ (acidic medium), acetic acid could be a possible product at potentials higher than +0.4 V (vs. Ag/AgCl) (eq. 1-17).



It was also proposed that the C-C bond cleavage occurred extensively at potentials typically below 0 V (vs. Ag/AgCl), leading to formation of the Pt-CH_x and Pt-CH_yO species (reaction 1-14). However, these two species tend to undergo different subsequent reactions; that is, formation of the adsorbed CO originate, mainly, from oxidation of the Pt-CH_yO (eq. 1-15), while majority of the Pt-CH_x can be reduced to methane at E < 0 V²⁴. It is noteworthy to stress that, based on Wieckowski *et al.*'s report,²³ acetaldehyde is not a stable product for ethanol oxidation at Pt. As a matter of fact, their results suggested that the oxidative adsorption of ethanol to acetaldehyde, depending on the potential, will be followed by formation of Pt-CH_yO and Pt-CH_x, and/or acetic acid.

It is obvious that the reaction pathway for the EOR is much more complex than that for the MOR. In fact, the key challenge for the EOR is the efficiency of the C-C bond cleavage (eq. 1-14), which can significantly limit production of CO₂ and results in low overall efficiency for EOR as a fuel cell reaction.

1.1.2.5. Oxygen reduction

Even though efforts are being made to find alternative cathodic reactants (e.g. CO₂), oxygen is the reactant of choice for use in the cathodes of fuel cells. The oxygen

reduction reaction (ORR) mechanism has long been a challenge and is believed to consist of two parallel pathways, as follows.²⁵

1. The dissociative mechanism which begins with cleavage of the O=O bond followed by protonation, eq. 1-18 through 1-20.

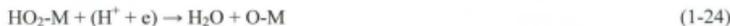


The complete reduction of O₂ to produce two H₂O is a 4-electron process which is the desirable pathway for the ORR.

2. The associative mechanism in which the protonation step precedes O=O bond cleavage, eq. 1-21 and 1-22.



Then, the HO₂-M intermediate can proceed through two different pathways: one leading to production of H₂O₂ (eq. 1-23), and the other leading to complete reduction of O₂ to H₂O (eq. 1-24 through 1-26).



Unfortunately, the complete reduction of O₂ to H₂O only occurs to a large extent at a few precious metals such as Pt and Pd. Note that production of H₂O₂ is

disadvantageous to the efficiency of fuel cells since not only can it be seriously harmful to the cathode components (i.e. corrosive to the catalyst layer), but also incomplete reduction of O_2 to H_2O_2 occurs at markedly less positive potentials, lowering the fuel cell potential, which can lead to significant energy and density losses.²⁵

1.1.3. Catalysts

An extensive amount of research has been focussed on the development of efficient and active catalysts for both the anodes and cathodes of fuel cells. In this regard, under the acidic conditions of PEM fuel cells, precious metals such as Pt and Pd are considered as metals of choice for both anode and cathode catalysts. This is owed to their markedly higher activity for the common fuel cell reactions, including the oxidation of organic fuels at the anode and the oxygen reduction reaction (ORR) at the cathode.

Even though the study of the ORR as the inefficient cathodic reaction has been intense for decades, it was only in 1999 that a systematic study on ORR at highly improved Pt-based catalysts was reported.²⁶ Since then, many possible ways to enhance the activities of Pt and Pd have been investigated. There are a number of papers reporting the catalytic activity of conducting polymers towards the ORR^{27, 28} and their synergetic effects on ORR at metallic catalysts,²⁹⁻³² enhanced activity of ORR due to the use of various carbon supports,³³⁻³⁵ and introduction of Pt-non-noble metal alloys as prominent catalysts for ORR.^{26, 36} More recently, the promotional effects of non-noble 3d metals on the ORR on Pt have been systematically studied by Stamenkovic and coworkers.³⁷⁻⁴⁰ They found that addition of a 3d transition metal such as Ni, Co, or Fe in a controlled

ratio would accelerate ORR at Pt through modification of the electronic properties of Pt. It was also suggested that the improved electronic effects could be attributed to the optimal d-vacancy brought about by alloying with 3d metals. The optimal d-vacancy gives rise to an adjusted adsorption energy of O₂ on Pt. That is, O₂ adsorption becomes less exothermic after which the first electron-proton transfer step becomes less endothermic. Therefore, the first electron-proton transfer step will require a lower overpotential.³⁷⁻⁴⁰

On the other hand, electrocatalytic oxidation of hydrogen, short-chain alcohols, and formic acid are the most commonly studied fuel cell anodic reactions.⁴ Pt is the metal of choice for the oxidation of hydrogen, methanol, and ethanol while Pd is much more active than Pt in formic acid oxidation.^{7, 8, 10, 11} However, large overpotentials and slow kinetics for the oxidation of ethanol and methanol at Pt,^{8, 11} unstable catalytic activity for formic acid oxidation at Pd (due to gradual formation of poisoning intermediates), and low activity of Pt towards formic acid oxidation¹⁰ (due to the fast formation of poisoning intermediates) have caused considerable attention to be paid to the development of more efficient catalysts to overcome these issues (i.e. more activity and higher catalytic stability). In this respect, alloying Pt and Pd with various metals, use of conducting polymers (CPs) as additives, and altering supports in terms of structure and composition have been widely practiced to achieve these goals.^{7, 8, 10, 11}

CPs such as polyaniline (PANI), polypyrrole (PPy), and polythiophene (PTh) have been extensively investigated as additive materials to Pt and Pd for improving their performances as anode catalysts.⁴¹ Croissant *et al.*⁴² showed that incorporating Pt into a

PANI matrix greatly increased the activity of Pt for the oxidation of hydrogen. In an early report by Gholamian *et al.*,⁴³ it was suggested that a 10-fold increase in formic acid oxidation activity of a PANI-Pt composite compared to pure Pt was due to the weakened bond of poisoning species with Pt leading to a lower number of reaction sites being blocked with such intermediates. Similarly, Kost *et al.*⁴⁴ reported that methanol oxidation at Pt was promoted by deposition of Pt within a 3-dimensional PANI substrate. They showed that the presence of PANI was effective in lowering the coverage of blocking intermediates. Kost *et al.*⁴⁴ also showed that even though the oxidation of methanol at Pt typically gave decaying currents typical for the catalytic oxidation of alcohols at Pt, the PANI-Pt composite became stable after 5 hours in a sharp contrast to the pure Pt electrode which showed decaying activity at all times. This superior long-term performance was suggested to be a consequence of limited formation of blocking intermediates at the Pt particles supported on PANI. Consistently, Salavagione *et al.*⁴⁵ reported a similar effect for a PANI-Pt system in the oxidation of methanol.

To commence discussion of formic acid oxidation at either Pt or Pd, it is noteworthy to stress that formic acid and methanol oxidation at Pt follow quite similar mechanisms including oxidative removal of adsorbed CO (see section 1.1.2); therefore, any means of preventing formation/strong attachment of such intermediates should accelerate both reactions at Pt. Hence, a similar explanation could apply to the promotional effects of PANI on formic acid oxidation at Pt. Nevertheless, in contrast, whereas PANI is known to promote formic acid oxidation at Pd which essentially follows the direct oxidation pathway (i.e. one-step production of CO₂ as final product without

significant formation of intermediates; see section 1.1.2.3), its synergetic effects on the system were suggested to originate from formation of oxygen donor agents which can accelerate the oxidation.⁴⁶

Unlike methanol and formic acid oxidation, the oxidation of ethanol at Pt supported on CPs has not been studied extensively. In a recent work, Gavrilov *et al.*⁴⁷ reported a promotional effect of a composite of PANI and carbon nanotubes on ethanol oxidation at Pt nanoparticles. In support of the effects of CPs on the oxidation of anodic fuels, one may also find a number of reports on hydrogen oxidation at Pt-PPy,^{41, 48} methanol oxidation at Pt and PtRu supported on PPy,^{41, 49-51} formic acid and formaldehyde oxidation at Pt-based catalysts supported on PPy-carbon nanotube composites,^{41, 52} oxidation of methanol, ethanol and formic acid at Pt supported on PANI networks,^{41, 53} and a number of papers^{41, 54-56} demonstrating metal-PTh systems as anode catalysts.

Fabrication of metallic mixtures is an important approach in the development of efficient catalysts for anodic reactions,^{10, 11, 57, 58} Over the past decades, various methods have been developed to make binary and ternary alloyed structures, codeposited, coreduced, and decorated multimetallic catalysts, and physical mixtures of metals.⁵⁷ As noted earlier, due to their superior performances, Pt and Pd based catalysts have remained unchallenged in the oxidation of anodic fuels.

In the mid 70s, Ross *et al.* systematically investigated the oxidation of hydrogen in the presence of dissolved CO at Pt-based metallic catalysts.^{59, 60} Interestingly, they showed that for a Pt-Rh system,⁵⁹ the larger catalytic activity was not due to a higher

degree of CO tolerance for the alloyed catalyst but was due to acceleration of the oxidation of hydrogen in the presence of Rh. In contrast, their second work on alloyed Pt-Ru catalysts showed that active oxidative removal of CO in the presence of Ru played a key role in enhancement of the catalytic oxidation of hydrogen. These early studies provide a suitable platform to begin discussion of Pt-Ru systems as highly active catalysts in methanol oxidation. Due to the widespread use of Pt-Ru catalysts in the development of DMFCs, the oxidation of methanol at these catalytic assemblies has been widely studied.^{11, 61, 62} As shown in section 1.1.2.2, oxidation of methanol at Pt has to proceed through a CO oxidation step. As an example, in 1995 Markovic *et al.*⁶³ showed that for a Pt-Ru alloy trace amounts of Ru in the vicinity of Pt species lowered the CO coverage (CO tolerance increase) and increased the activity for methanol oxidation through Ru oxide assisted oxidation of CO. Therefore, in the light of previous work on this system and as a result of the high activity of the Pt-Ru system for the oxidation of methanol, much interest has been increasingly devoted to optimizing Pt-Ru catalysts to improve the performances of DMFC anodes. Hiromi *et al.*⁶⁴ recently showed that a 50% atomic content of Ru (Pt:Ru) gave the highest methanol oxidation activity at their Pt-Ru alloy catalysts. In another study, Inoue *et al.*⁶⁵ used the "polygonal barrel-sputtering method"⁶⁶ to synthesize Pt-Ru mixtures of various particle sizes. They showed that uniformity of the nanoparticles (optimized 50:50 atomic content for Pt and Ru) was important to obtain a sharp and low-onset CO oxidation peak. In fact, their method seems appropriate to produce Pt-Ru combinations of controlled size and ratio with superior performances to commercial Pt-Ru catalysts.

The electrochemical oxidation of ethanol is different from methanol oxidation in that the former necessitates a C-C bond cleavage step for completion (i.e. CO₂ production). However, similar to methanol oxidation, Pt has long been considered the metal of choice for ethanol oxidation. Even so, much effort has been made for further improvement. In this respect, it has been shown that binary catalysts of Pt with Ru, Sn, W, Pd, Rh, Re, Mo, Ti, Ce showed superior performances to pure Pt, with Pt-Ru and particularly Pt-Sn being the best known binary catalysts for ethanol oxidation.⁵⁸ Antolini *et al.*⁶⁷ reported that while Pt-Sn is truly the prominent binary combination for ethanol oxidation, addition of Ru oxide in a certain ratio improved the activity significantly, presumably due to synergetic effects of Sn and Ru. However, they showed that a 1:1:1 atomic ratio of the three metals is inferior to both Pt-Ru and Pt-Sn, since it seemed that Pt tended to interact solely with Ru and not with Sn in the presence of high loadings of Ru. This can clearly provide evidence for the important role of Sn in ethanol oxidation at Pt. Similarly, Cunha *et al.*⁶⁸ showed that addition of Ru and Sn to Pt remarkably decreased the onset potential for CO oxidation since oxides of these two metals can promote oxidation of CO at less positive potentials than Pt. The results presented by both Antolini *et al.*⁶⁷ and Cunha *et al.*⁶⁸ are in disagreement with Wang *et al.*'s report.⁶⁹ Wang *et al.* developed a differential electrochemical mass spectrometry (DEMS) comparative analysis on Pt, Pt-Ru, Pt-Sn, and Pt-Sn-Ru. They suggested that while the presence of Sn and Ru or both caused a negative shift in the CO oxidation onset, the CO₂ yield remained almost unchanged. Therefore, they concluded that the main issue in ethanol oxidation is not CO oxidation but breaking the C-C bond. In fact, complete oxidation of ethanol

occurred to only a small extent with these combinations, and the yield of CO_2 did not change for any of the catalysts. These somehow conflicting results clearly indicate that the electrochemical oxidation of ethanol is still not a well understood reaction and should be explored further. Meanwhile, it is always an interesting idea to develop less expensive catalysts for fuel cell reactions.^{70, 71} Du *et al.*⁷¹ have recently demonstrated a "surfactant-free method" to synthesize an iridium/iridium-tin/tin oxide catalyst for ethanol oxidation; their report is very significant in that not only have they used a more economic base metal⁷² (Ir with ~ half price as Pt per gram) for catalyst preparation, but they have obtained a catalyst with superior activity to Pt.

Research in the field of formic acid oxidation was systematically started when this fuel was introduced as a serious alternative to methanol.⁷³⁻⁷⁶ In this regard, various catalysts, mainly based on Pd and Pt as the most active metals for formic acid oxidation, have been developed.¹⁰ It is noteworthy that these two metals behave differently in formic acid oxidation; Pd and Pt oxidize formic acid through direct and indirect pathways (see section 1.1.2.3), respectively.^{10, 19} Consequently, they show different catalytic features. Formic acid oxidation at Pt results in rapid accumulation of adsorbed CO (dehydration of formic acid), so as a result the initial activity dramatically decays in a manner of seconds. In contrast, formation of adsorbed CO at Pd during formic acid oxidation is a very slow process.^{77, 78} This difference can reasonably account for the different constant potential oxidation behaviours of formic acid at Pd and Pt; that is, the polarization at Pt shows a sharp drop at very short times followed by a somewhat stable catalytic pattern, while the chronoamperometric profile for Pd normally displays a

continuous decay over an experimental timescale of hours (but with a much lower rate of decay with time initially compared to Pt).¹⁰ On this basis, research on the development of efficient catalysts for formic acid oxidation has been essentially devoted to increasing long term activity of both Pd and Pt. Yu *et al.*⁷⁹ synthesized a carbon black supported PdSb catalyst for use in DFAFCs which was greatly resistant to the time-dependent deactivation. Consistent with some earlier report of Haan *et al.*,⁸⁰ Yu *et al.* interpreted the effect based on the promoted (i.e. negative shift in the oxidation onset) oxidation of CO at their PdSb/C catalyst rather than inhibited formation of CO in the presence of Sb. However, there are still concerns about the actual origin of this deactivation. In a mechanistic study, Yu *et al.*⁷⁸ suggested that the deactivation can be basically ascribed to buildup of adsorbed CO which agreed well with Miyake *et al.*'s⁷⁷ conclusion in an earlier paper. Nevertheless, Miyake *et al.* showed that bridge-bonded formate and the counter anion of the electrolyte (e.g. sulfate for H₂SO₄) were also involved in the deactivation. Yu *et al.* have also studied making combinations of Pt with metals such as Pb,⁸¹ Sb,^{81, 82} and Bi.⁸³ It was shown that formation of blocking CO adsorbate at Pt was inhibited in the presence of all three metals (Pb, Sb, and Bi) although the effect of Bi was stronger and somewhat controversial and suggested to be due to "selective blocking of sites at which CO is formed".⁸³ Earlier on, Lopez-Cudero *et al.*⁸⁴ showed that while formic acid oxidation at Pt was promoted by Bi, the effect was not attributed to inhibited CO adsorption. This result is contrary to Hayden's report⁸⁵ suggesting that a high coverage of Bi greatly decreased CO adsorption. Research into the development of Pd-based and Pt-based catalysts for formic acid oxidation continues to be very active not

only to unambiguously address conflicting issues but also to make catalysts that can efficiently catalyze complete oxidation of formic acid without significant deactivation.

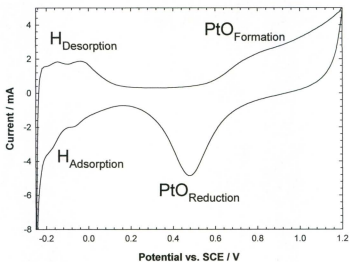


Figure 1-1. Cyclic voltammogram of a Pt electrode (0.071 cm^2 ; CH Instruments) in 1 M H_2SO_4 at 100 mV s^{-1} .

1.1.4. Typical voltammetric observations for fuel cell reactions

1.1.4.1. Electrochemistry of Pt

Metals such as Ir, Rh, Pd, and Pt produce similar voltammetric patterns which consist of two main regions.^{17, 86, 87} First, they all show hydrogen electrochemistry at the cathodic tail identified with hydrogen desorption (H_{des}) on the anodic leg and hydrogen adsorption (H_{ads}) on the cathodic leg. The typical sharp rising current at the extreme of

the cathodic limit is indicative of the hydrogen evolution reaction (HER). Another characteristic region at more positive potentials ($E > +0.5$ V vs. SCE) encompasses formation and stripping of a metal oxide layer. Here formation of an oxide layer normally gives a broad wave on the anodic sweep which is followed by a well-defined reduction peak on the cathodic scan due to the oxide layer stripping. These features are illustrated in figure 1-1 which is a typical voltammogram for a disc Pt electrode in a sulfuric acid solution.

1.1.4.2. Electrocatalytic oxidation of methanol at Pt

As described in section 1.1.2.2, the methanol oxidation reaction (MOR) at Pt involves formation of adsorbed CO intermediates followed by oxidative production of CO_2 . Figure 1-2, which illustrates MOR at Pt, presents typical voltammetric features of this process. The peak A_1 is mainly due to the oxidative removal of the adsorbed CO intermediates (reactions 1-6 and/or 1-7) formed during the adsorptive decomposition of methanol at the Pt nanoparticles (reactions 1-4 and 1-5). As seen in the anodic extreme of the forward scan, the sharp rising current can be attributed to the direct oxidation of methanol at $E > +0.8$ V vs. SCE (peak A_2). On the reverse scan, rapid oxidation of methanol occurs at sufficiently less positive potentials where the oxide layer is stripped off and reaction sites are free of the blocking intermediates (peak A_3).¹⁷

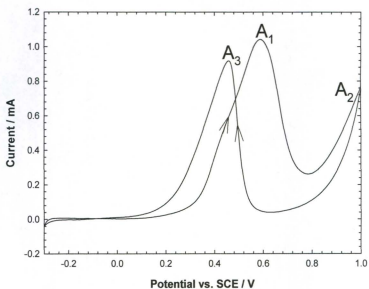


Figure 1-2. A typical voltammogram (10 mV s^{-1}) of ca. 0.1 mg cm^{-2} Pt nanoparticle (see section 4.2.2 for the preparation method) coated on a glassy carbon electrode in $0.1 \text{ M H}_2\text{SO}_4$ containing 0.2 M methanol.

1.1.4.3. Electrocatalytic oxidation of formic acid

Figure 1-3 shows a typical cyclic voltammogram of the oxidation of formic acid at Pt. The forward scan initiates with a weak signal (A_1) at low potentials attributed to the direct oxidation of formic acid (reaction 1-8), which is followed by a stronger signal (A_2) due to the oxidative removal of the adsorbed CO intermediates (reaction 1-10). The reverse scan is dominated by signals (A_3 and A_4) presumably due to the oxidation of the adsorbed intermediates and/or the direct oxidation of formic acid. Voltammetric

oxidation of formic acid (figure 1-4) at Pd gives different features; in contrast to formic acid oxidation at Pt, the A_1 signal for Pd is strong and dominates the forward scan, and is indicative of the prevailing direct pathway. However, the weak A_2 shoulder likely originates from the oxidative removal of the adsorbed intermediates formed as a result of the incomplete oxidation of formic acid. The reverse scan for Pd appear with somewhat similar characteristics to that for Pt displaying the oxidation of the adsorbed intermediates and/or the direct oxidation of formic acid (figure 1-4; A_3 region).^{10, 88}

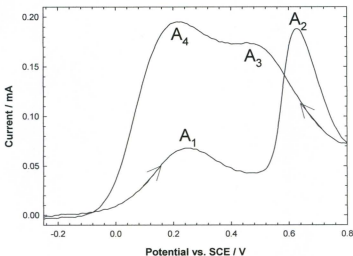


Figure 1-3. A typical voltammogram (10 mV s^{-1}) of ca. $10 \mu\text{g cm}^{-2}$ Pt nanoparticles (see section 4.2.2 for the preparation method) coated on a glassy carbon electrode in $0.1 \text{ M H}_2\text{SO}_4$ containing 0.5 M formic acid.

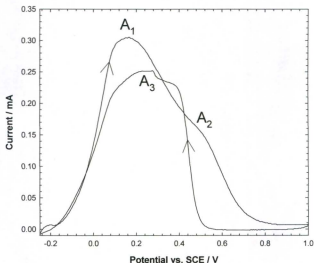


Figure 1-4. A typical voltammogram (10 mV s^{-1}) of ca. $15 \mu\text{g cm}^{-2}$ Pd nanoparticles (see section 5.2.2 for the preparation method) coated on a glassy carbon electrode in $0.1 \text{ M H}_2\text{SO}_4$ containing 0.5 M formic acid.

1.1.4.4. Electrocatalytic oxidation of ethanol at Pt

The ethanol oxidation reaction (EOR) at Pt typically gives similar observations to the MOR at Pt. The A_1 peak (figure 1-5) can be ascribed largely to the oxidative removal of the adsorbed CO intermediates (and probably CH_xO_y species) formed during the adsorptive decomposition of ethanol. The A_2 region ($E > +0.8 \text{ V vs. SCE}$) in the EOR at Pt consists of a peak overlapping a rising current (only a rising current for methanol oxidation). The reverse scan of the EOR at Pt, which accommodates rapid oxidation of ethanol, displays similar observations to the MOR at Pt (peak A_3).²¹⁻²³

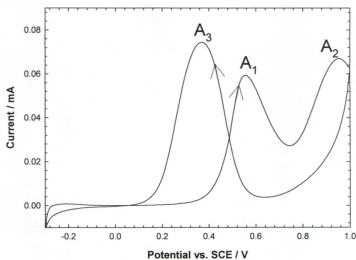


Figure 1-5. A typical voltammogram (10 mV s^{-1}) of ca. $5 \mu\text{g cm}^{-2}$ Pt nanoparticles (see section 4.2.2 for the preparation method) coated on a glassy carbon electrode in $0.1 \text{ M H}_2\text{SO}_4$ containing 0.2 M ethanol.

1.1.5. Supports

Carbonaceous substances, conducting polymers, metals, and metal oxides are well-known support materials for fuel cell catalysts.⁴¹ Ideally, fuel cell catalyst supports should possess a large surface/volume ratio to accommodate highly dispersed catalyst particles (i.e. high loadings in lower volumes) which can improve catalytic activity, and size-controlled porosity to enhance gas flow rates (for the cathode where the reactant is typically a gas such as O_2 in air). Moreover, it is of high importance to develop supports

with high electronic and ionic conductivity to increase the efficiency of the fuel cell reactions through providing fast electron/proton transport and unimpeded accessibility of the fuel to the catalyst species. This also decreases inevitable means of voltage losses such as ohmic drop. Finally, long-term operation of fuel cells necessitates development of highly stable supports. That is, suitable supports are expected to tolerate the operational conditions of fuel cells which are highly acidic and oxidative (large potentials).^{41, 89-91}

1.1.5.1. Carbon

Carbon supports have long been considered as important materials in the development of nanostructured catalysts for fuel cells.⁴¹ They possess large surface areas (i.e. large surface/volume ratio), high electrical conductivity, and can be highly porous, all of which are desired properties for a potential fuel cell support.⁹² Consequently, they can accommodate high loadings of a catalyst (e.g. Pt, Pd etc.) in a small volume and establish fast (even accelerated) electronic communication between the catalyst and electrode.^{41, 92} However, the rate of proton transport with carbon supports is limited since carbon is intrinsically a poor ionic conductor.⁴¹ Furthermore, catalyst species loaded into a typical carbon black support cannot be accessed efficiently by the fuel due to the presence of the ultrafine pores (~ 2 nm diameter) in the structure.⁴¹ Another drawback associated with the use of carbon blacks as fuel cell catalyst supports is their low resistance to highly corrosive environments.^{89, 90} As an alternative to carbon blacks, carbon nanotubes (CNTs) have been used more recently as catalyst supports^{41, 93, 94} offering somewhat improved properties (e.g. larger surface area, faster electronic conductivity, and more stability against corrosion). Nevertheless, they inherit the problem

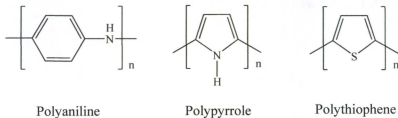
of the intrinsic low proton conductivity of carbonaceous materials. Moreover, CNTs are very expensive materials and consequently inappropriate for economic mass production.

1.1.5.2. Conducting polymers

Conducting polymers (CPs) are a class of organic compounds with an extended π -orbital network that facilitates electron transfer along polymeric chains.^{41, 95} The doping process in CPs consists of oxidation causing electron deficiencies, compensated for by incorporation of an equal number of anion charges from the oxidizing medium for charge neutrality. In this state, the CP is electronically conductive and the counter ion inserted for charge neutrality is termed the dopant.⁹⁶

Possessing excellent electron transfer characteristics and in some cases good proton conductivities, CPs have been extensively used as either additive or alternatives to carbon materials as supports for fuel cell catalysts.^{41, 97} Materials of this class are typically easy to prepare and have three-dimensional structures that can provide large accessible surface areas for incorporation of metallic catalysts.⁴¹ It was reported in a number of studies that composites of metallic catalysts with CPs showed substantially improved electrochemical properties.⁴¹ Additional to their excellent electronic conductivity, CPs are beneficial in inhibiting the formation and/or strong attachment of the poisoning intermediates (mainly CO) formed in the oxidation of alcohols and formic acid at Pt or Pd.⁴¹ It is discussed in section 1.1.2 that one important issues associated with the oxidation of carbon-containing fuels is formation of poisoning intermediates. These intermediates seriously block active sites of the catalyst, and as a result deteriorate catalytic performance.

Polyaniline (PANI), polypyrrole (PPy), and polythiophene (PTh) are the most commonly used and studied CPs in the development of fuel cell supports.⁴¹ Scheme 1-1 displays typical structures of these polymers.



Scheme 1-1. Typical structures for polyaniline, polypyrrole, and polythiophene.

Among all CPs, PANI has been studied most extensively.⁴¹ It is easy to prepare, environmental stable, and has simple redox chemistry. Furthermore, PANI presents impressive electrical conductivity ($\sim 5 \text{ S cm}^{-1}$)⁹⁸ and significant ion conductivity.⁹⁹ The potential-dependent conduction mechanism of PANI encompasses electron and proton exchanges, the speeds of which approach a maximum at 0.3 - 0.5 V vs. SCE.¹⁰⁰ The other nitrogen-rich CP is PPy which has typically similar qualities to PANI but appreciably higher conductivity.¹⁰¹ In both oxidative chemical and electrochemical methods for the polymerization of pyrrole, the counter ion of the oxidizing agent plays a key role in the conductivity of the resulting film.¹⁰² The conductivity of PPy doped with either aromatic or very large amphiphilic sulfonate dopants can reach 120 S cm^{-1} , while PPy doped with perchlorate gives conductivities of only ca. 15 S cm^{-1} . Besides, PPy possesses exciting chemical stability, and also it can withstand temperatures as high as $300 \text{ }^\circ\text{C}$.¹⁰³ The latter

property is critical in the development of catalysts for high temperature fuel cells. Moreover, in contrast to PANI, PPy has the highest conductivity in the range of -0.2 to 0.2 V vs. SCE, and is therefore potentially more suitable as a catalyst support for fuel cells which are operational over this range.¹⁰⁴ The other CP considered here is PTh which can be made either by oxidative chemical synthesis or electrochemical polymerization.¹⁰⁵ While having interesting redox characteristics, PTh offers limited applications compared to PANI and PPy. In fact, although it can reversibly change oxidation state from negatively to positively charged, the stability of the n-doped form is not satisfactory.¹⁰⁵

1.1.5.3. Metals and metal oxides

Metals and metal oxides form the other class of supports for fuel cell catalysts.⁹¹⁰⁶ The development of metals and metal oxides as support materials has been targeted not only to improve the activity of the catalyst species in a typical fuel cell reaction, but they also can decrease the use of precious metals (e.g. Pt and Pd) while maintaining a desirable level of performance. Furthermore, these support materials can provide a high area platform for embedding the catalyst particles, which can greatly improve the efficiency of the catalytic reactions.¹⁰⁶ Above all, metal-based supports are known to impart synergetic effects (e.g. bifunctional, third-body effect, etc) on fuel cell reactions through establishing strong electronic interactions with the catalyst particles and causing changes in the physicochemical properties of the catalyst.^{82, 83, 107-111} As an instance, Ru (i.e. Ru oxide) is unambiguously known as a strong CO oxidation promoter¹¹² and therefore it should enhance activity for any fuel cell reactions that involves a CO

oxidation step. As such, the Pt-Ru system is, to date, the most active combination for the oxidation of methanol.^{57, 106}

1.2. Scope and outline of this thesis

The present thesis essentially deals with fundamental studies of conducting polymers as potential support materials for fuel cell applications, methods for preparation of conducting polymer and metal oxide supports for use as support materials in fuel cells, and a systematic study of support effects on the oxidation of well-known organic fuels (methanol, ethanol, and formic acid). The research objectives for this thesis are summarized as follows:

1. Electrochemical impedance spectroscopy as a powerful tool to probe the formation of polypyrrole by means of various electrochemical techniques on high surface area carbon electrodes;
2. Study of the oxidation of formic acid at Pd nanoparticles (spontaneously deposited and drop coated) incorporated into various polyaniline coated carbon fibre paper electrodes;
3. Introduction of drop coating as a powerful methodology to study support effects on the oxidation of methanol at Pt nanoparticles;
4. Extension of the drop coating method to study the role of polyaniline supports on the oxidation of formic acid at Pd nanoparticles;
5. A mechanistic study of the oxidation of ethanol at Pt nanoparticles drop coated on various metal oxide modified electrodes.

1.3. Electrochemical techniques

We used cyclic voltammetry, chronoamperometry, and electrochemical impedance spectroscopy as powerful electrochemical techniques for our studies. Thus, we describe in this section fundamentals and general theories of these techniques to provide a background for readers of this thesis.

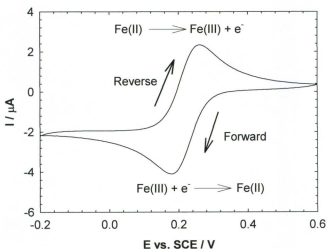


Figure 1-6. Voltammogram (20 mV s^{-1}) of a Pt disk electrode (0.05 cm^2) in 1 M KNO_3 containing $0.01 \text{ M K}_3\text{Fe(CN)}_6$.

1.3.1. Cyclic voltammetry

Cyclic voltammetry (CV) is an electrochemical technique in which the potential of a working electrode (relative to a reference electrode) is cycled between two values

(normally at a constant potential scan rate), and the response, in the form of an electrical current, is recorded.¹¹³ This technique is a powerful diagnostic tool to provide significant thermodynamic and kinetic data, as well as important information such as chemical/electrochemical reversibility. Figure 1-6 shows a cyclic voltammogram for the well-known reversible system of $\text{Fe}^{2+}/\text{Fe}^{3+}$. The forward scan is dominated by a sharp cathodic signal due to reduction of Fe^{3+} (sweeping from more positive to more negative potentials) following which a sharp anodic peak on the reverse scan showing the oxidation of Fe^{2+} (sweeping from more negative to more positive potentials).

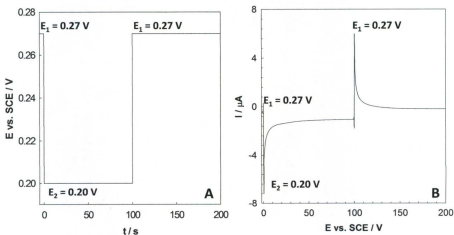


Figure 1-7. Typical chronoamperometric waveform (A) and waveshape (B) for a Pt disk electrode (0.05 cm^2) in 1 M KNO_3 containing $0.01 \text{ M K}_3\text{Fe}(\text{CN})_6$.

1.3.2. Chronoamperometry

Constant potential polarization or chronoamperometry (CA) is a powerful technique to explore short and long term (i.e. time-dependent) operation of electrochemical systems. This technique, which is central to fuel cell tests, involves measuring the current over a certain timescale at a fixed potential. Figure 1-7 illustrates profiles of a stimulus and response for typical chronoamperometry as a function of time where the initial potential of E_1 is stepped to E_2 at which the electrochemical reaction is active. The decay pattern for the CA is because of the decrease of the current components (both charging and faradaic) with time and depletion of the diffusion layer from electroactive species. As can be seen, stepping back to E_1 from E_2 would generate current due to the oxidation of Fe^{2+} species, which was absent at the electrode surface at the beginning of the chronoamperometry.¹¹⁴

1.3.3. Electrochemical impedance spectroscopy

Electrochemical impedance spectroscopy (EIS) is an important technique which can be employed to obtain a variety of information (capacitance, resistance/conductivity, kinetics, etc). By definition,¹¹⁵ a frequency-dependent sinusoidal stimulus, potential (v) (or current), eq. 1-26, is applied to the working electrode, and the sinusoidal response in the form of a current (i) (or potential), eq. 1-27, is analyzed by a frequency response analyzer.

$$v(t) = V_m \sin(\omega t) \quad (1-26)$$

$$i(t) = I_m \sin(\omega t + \theta) \quad (1-27)$$

Here t , v , V_m , i , I_m , ω ($= 2\pi f$), and θ ($= \tan^{-1} \frac{Z_{imag}}{Z_{real}}$) are time, voltage, maximum voltage (sinusoidal wave amplitude), current, maximum current (sinusoidal wave amplitude), radial frequency (f = frequency), and phase shift (between the voltage and the current), respectively.

Taking into account the stimulus (potential; v / volt) and the response (current; i / ohm), the total impedance (Z / ohm) which has components of a resistance can be derived (eq. 1-28).

$$Z = \frac{V_m \sin(\omega t)}{I_m \sin(\omega t + \theta)} = Z_m \frac{\sin(\omega t)}{\sin(\omega t + \theta)} \quad (1-28)$$

$$Z = Z_{real} + jZ_{imag} \quad (1-29)$$

$$|Z| = [(Z_{real})^2 + (Z_{imag})^2]^{1/2} \quad (1-30)$$

$$Z_{real} = |Z| \cos \theta \quad (1-31)$$

$$Z_{imag} = |Z| \sin \theta \quad (1-32)$$

Here j , the imaginary number, accounts for anticlockwise rotation of the imaginary impedance (Z_{imag}) relative to the real impedance Z_{real} .¹¹⁵

As shown in eq. 1-29, the impedance (in ohm) consists of two components: real impedance (Z_{real}) and imaginary impedance (Z_{imag}). Combination of these two components (both functions of frequency) forms a complex-plane diagram (Nyquist).¹¹⁵ In the study of EIS, the response of a typical electrochemical reaction is translated to various electrical elements, each of which corresponds to a specific behaviour of the system. In fact, electrical elements in an equivalent circuit represent characteristic features of the system under study. For example, equivalent circuits include a resistor

(R_{Ω} ; connected in series) representing the resistances of the solutions and wires which always have a nonzero value; as well, a charge transfer resistance (R_{CT}) represents a resistance to the electron transfer (i.e. in an electrochemical reaction).¹¹⁶

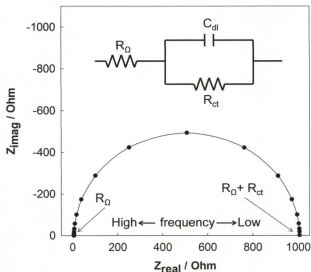


Figure 1-8. A simulated (ZView2, Scribner Associates Inc.) Nyquist plot and the equivalent circuit (inset) used for the simulation: $R_{\Omega} = 6 \Omega$; $R_{CT} = 1000 \Omega$; $C_{DL} = 1.31 \times 10^{-5} \text{ S s}$.

Figure 1-8 displays the circuit (inset) that is equivalent to the Nyquist plot shown below it. Therein, elements such as an R_{Ω} , an R_{CT} , and a C_{DL} (capacitance of an electrical double layer) are seen, which together produce a semi-circle on the Nyquist profile. Apart from this simplified example, electrochemical systems are often more complex and therefore need sophisticated equivalent circuits.

One complication that occurs to the impedance of porous electrodes is the appearance of a 45° line in the midrange frequencies, namely a Warburg line, which essentially indicates an ionic resistance (or mixed ionic/electronic resistance).¹¹⁷ Figure 1-9 displays a simulated Nyquist plot consisting of R_Ω and a Warburg-type line at high frequencies and capacitive behaviour at lower frequencies.

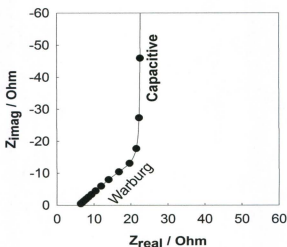


Figure 1-9. A simulated (ZView2, Scribner Associates Inc.) Nyquist plot displaying Warburg-type and capacitive impedances; $R_\Omega = 6 \Omega$; $C_{DL} = 1.31 \times 10^{-2} \text{ S s}$; $R_L = 50 \Omega$; $C_L = 10 \text{ mF}$.

Figure 1-10 exhibits a typical transmission line equivalent circuit,^{117, 118} containing a R_Ω , and a number of paralleled R_L and C_L for simulating Warburg-type behaviour. In a Warburg-type element, the R_L represents ionic/electronic resistance of the electroactive layer (e.g. for a porous electrode) at high frequencies, and the C_L gives the

capacitance at low frequencies. Assuming uniformity of the electroactive layer, it consists of countless number of the equal paralleled R_L and C_L .^{117, 118}

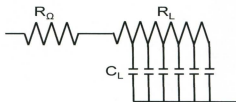


Figure 1-10. Equivalent circuit compatible with the Nyquist plot shown in figure 1-9.

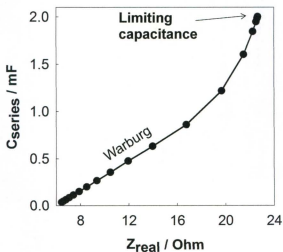


Figure 1-11. Capacitance as a function of the real impedance for the Nyquist data shown in figure 1-9.

As shown in figure 1-9, another important aspect of impedance is the appearance of capacitive behaviour which is particularly significant for highly capacitive materials

such as porous carbons, CPs, and Ru oxide.¹¹⁷⁻¹¹⁹ This type of impedance appears as a $\sim 90^\circ$ line at low frequencies in Nyquist plots. Such capacitive behaviour is best visualized by plotting series capacitance (C_{series} ; in farad) as a function of the real impedance. Figure 1-11 illustrates a “capacitance plot” for the impedance shown in figure 1-9. Here the real impedance at the highest frequency, obviously, gives the ohmic resistance (R_Ω), while no charge transfer resistance (R_{CT}) was included in the simulation circuit model. In a capacitance plot, a charge transfer resistance (R_{CT} paralleled to a C_{DL}) is characterized by offset of the Warburg region along the Z_{real} axis (insignificant increase in capacitance with frequency),¹¹⁷ as shown in figure 1-11. The slope of the rising part of the capacitance plot, demonstrating the Warburg-type behaviour, is proportional to the conductivity.^{117,118} The lowest frequencies give the limiting capacitance.^{117,118} In an ideal system, the limiting capacitance following the Warburg-type region would consist of the points overlaying each other at the same capacitance and real impedance (representing the 90° line in a Nyquist plot with no further increase in the real impedance with frequency). However, the limiting capacitance can form a plateau-type feature at low frequencies in real systems. Ren *et al.*¹¹⁷ and Lefebvre *et al.*¹¹⁸ suggested that this “non-ideality” could originate from a large ionic resistance in some parts of the porous electrode.

References

1. U.S. EIA International Energy Statistics;
<http://205.254.135.7/cneaff/solar.renewables/page/trends/rentrends.html>, 2010.
2. H.-J. Neef, *Energy*, 2009, **34**, 327-333.
3. A. J. Cavallo, *Nat. Resour. Res.*, 2004, **13**, 211-221.
4. Y. Wang, K. S. Chen, J. Mishler, S. C. Cho and X. C. Adroher, *Appl. Energy*, 2010, **88**, 981-1007.
5. M. Winter and R. J. Brodd, *Chem. Rev.*, 2004, **104**, 4245-4270.
6. B. E. Conway, *Electrochemical supercapacitors: scientific fundamentals and technological applications*, Plenum Press, New York, 1999.
7. E. R. Gonzalez and E. Antolini, in *Encyclopedia of Electrochemical Power Sources*, Elsevier, Amsterdam, 2009, pp. 402-411.
8. C. Lamy, S. Rousseau, E. M. Belgsir, C. Coutanceau and J. M. Leger, *Electrochim. Acta*, 2004, **49**, 3901-3908.
9. T. Michael C., *J. Power Sources*, 2010, **195**, 4570-4582.
10. X. Yu and P. G. Pickup, *J. Power Sources*, 2008, **182**, 124-132.
11. X. Zhao, M. Yin, L. Ma, L. Liang, C. Liu, J. Liao, T. Lu and W. Xing, *Energy Environ. Sci.*, 2011, **4**, 2736-2753.
12. S. Basri and S. K. Kamarudin, *Int. J. Hydrogen Energy*, 2011, **36**, 6219-6236.
13. S. Wasmus and A. Kuever, *J. Electroanal. Chem.*, 1999, **461**, 14-31.
14. L. Bai, D. A. Harrington and B. E. Conway, *Electrochim. Acta*, 1987, **32**, 1713-1731.

15. B. E. Conway and L. Bai, *J. Electroanal. Chem. Interfacial Electrochem.*, 1986, **198**, 149-175.
16. N. M. Markovic, B. N. Grgur and P. N. Ross, *J. Phys. Chem. B*, 1997, **101**, 5405-5413.
17. J. Jiang and A. Kucernak, *J. Electroanal. Chem.*, 2005, **576**, 223-236.
18. C. Roth, A. J. Papworth, I. Hussain, R. J. Nichols and D. J. Schiffrin, *J. Electroanal. Chem.*, 2005, **581**, 79-85.
19. E. H. J.M. Feliu, in: W. Vielstich, H.A. Gasteiger, A. Lamm (Eds.), *Handbook of Fuel Cells*, Wiley, New York, 2003, **2**, 679.
20. F. Vigier, C. Coutanceau, A. Perrard, E. M. Belgsir and C. Lamy, *J. Appl. Electrochem.*, 2004, **34**, 439-446.
21. K. B. Kokoh, F. Hahn, E. M. Belgsir, C. Lamy, A. R. de Andrade, P. Olivi, A. J. Motheo and G. Tremiliosi-Filho, *Electrochim. Acta*, 2004, **49**, 2077-2083.
22. H. Wang, Z. Jusys and R. J. Behm, *Fuel Cells*, 2004, **4**, 113-125.
23. R. B. Kutz, B. Braunschweig, P. Mukherjee, R. L. Behrens, D. D. Dlott and A. Wieckowski, *J. Catal.*, 2011, **278**, 181-188.
24. T. Iwasita and E. Pastor, *Electrochim. Acta*, 1994, **39**, 531-537.
25. J. K. Norskov, J. Rossmeisl, A. Logadottir, L. Lindqvist, J. R. Kitchin, T. Bligaard and H. Jonsson, *J. Phys. Chem. B*, 2004, **108**, 17886-17892.
26. T. Toda, H. Igarashi, H. Uchida and M. Watanabe, *J. Electrochem. Soc.*, 1999, **146**, 3750-3756.

27. V. G. Khomenko, V. Z. Barsukov and A. S. Katashinskii, *Electrochim. Acta*, 2005, **50**, 1675-1683.
28. N. Gavrilov, M. Vujković, I. A. Pasti, G. Ćirić-Marjanović and S. V. Mentus, *Electrochim. Acta*, 2011, **56**, 9197-9202.
29. E. K. W. Lai, P. D. Beattie and S. Holdcroft, *Synth. Met.*, 1997, **84**, 87-88.
30. E. K. W. Lai, P. D. Beattie, F. P. Orfino, E. Simon and S. Holdcroft, *Electrochim. Acta*, 1999, **44**, 2559-2569.
31. E. Rios, S. Abarca, P. Daccarett, H. Nguyen Cong, D. Martel, J. F. Marco, J. R. Gancedo and J. L. Gautier, *Int. J. Hydrogen Energy*, 2008, **33**, 4945-4954.
32. D. Nguyen-Thanh, A. I. Frenkel, J. Wang, S. O'Brien and D. L. Akins, *Appl. Catal., B*, 2011, **105**, 50-60.
33. H. Gharibi, R. A. Mirzaie, E. Shams, M. Zhiani and M. Khairmand, *J. Power Sources*, 2005, **139**, 61-66.
34. D. Sebastian, M. J. Lazaro, I. Suelves, R. Moliner, V. Baglio, A. Stassi and A. S. Arico, *Int. J. Hydrogen Energy*, 2011, 6253-6260.
35. F. Jaouen, S. Marcotte, J.-P. Dodelet and G. Lindbergh, *J. Phys. Chem. B*, 2003, **107**, 1376-1386.
36. U. A. Paulus, A. Wokaun, G. G. Scherer, T. J. Schmidt, V. Stamenkovic, V. Radmilovic, N. M. Markovic and P. N. Ross, *J. Phys. Chem. B*, 2002, **106**, 4181-4191.
37. V. Stamenkovic, T. J. Schmidt, P. N. Ross and N. M. Markovic, *J. Phys. Chem. B*, 2002, **106**, 11970-11979.

38. V. R. Stamenkovic, B. S. Mun, K. J. J. Mayrhofer, P. N. Ross and N. M. Markovic, *J. Am. Chem. Soc.*, 2006, **128**, 8813-8819.
39. C. Wang, D. van der Vliet, K.-C. Chang, H. You, D. Strmcnik, J. A. Schlueter, N. M. Markovic and V. R. Stamenkovic, *J. Phys. Chem. C*, 2009, **113**, 19365-19368.
40. C. Wang, M. Chi, D. Li, D. Strmcnik, D. van der Vliet, G. Wang, V. Komanicky, K.-C. Chang, A. P. Paulikas, D. Tripkovic, J. Pearson, K. L. More, N. M. Markovic and V. R. Stamenkovic, *J. Am. Chem. Soc.*, 2011, **133**, 14396-14403.
41. E. Antolini and E. R. Gonzalez, *Appl. Catal., A*, 2009, **365**, 1-19.
42. M. J. Croissant, T. Napporn, J. M. Léger and C. Lamy, *Electrochim. Acta*, 1998, **43**, 2447-2457.
43. M. Gholamian, J. Sundaram and A. Q. Contractor, *Langmuir*, 1987, **3**, 741-744.
44. K. M. Kost, D. E. Bartak, B. Kazee and T. Kuwana, *Anal. Chem.*, 1988, **60**, 2379-2384.
45. H. J. Salavagione, C. Sanchis and E. Morallon, *J. Phys. Chem. C*, 2007, **111**, 12454-12460.
46. C. Liao, Z. D. Wei, S. G. Chen, L. Li, M. B. Ji, Y. Tan and M. J. Liao, *J. Phys. Chem. C*, 2009, **113**, 5705-5710.
47. N. Gavrilov, M. Dasic-Tomic, I. Pasti, G. Ciric-Marjanovic and S. Mentus, *Mater. Lett.*, 2011, **65**, 962-965.
48. F. T. A. Vork, L. J. J. Janssen and E. Barendrecht, *Electrochim. Acta*, 1986, **31**, 1569-1575.
49. M. Hepel, *J. Electrochem. Soc.*, 1998, **145**, 124-134.

50. V. Selvaraj and M. Alagar, *Electrochem. Commun.*, 2007, **9**, 1145-1153.
51. S. Zhang, H. Wang, N. Zhang, F. Kong, H. Liu and G. Yin, *J. Power Sources*, 2012, **197**, 44-49.
52. V. Selvaraj, M. Alagar and K. S. Kumar, *Appl. Catal., B*, 2007, **75**, 129-138.
53. R. K. Pandey and V. Lakshminarayanan, *J. Phys. Chem. C*, 2009, **113**, 21596-21603.
54. R. Schrebler, M. A. del Valle, H. Gomez, C. Veas and R. Cordova, *J. Electroanal. Chem.*, 1995, **380**, 219-227.
55. B. Rajesh, K. R. Thampi, J. M. Bonard, N. Xanthopoulos, H. J. Mathieu and B. Viswanathan, *J. Phys. Chem. B*, 2004, **108**, 10640-10644.
56. A. Galal, N. Atta, S. Darwish and S. Ali, *Top. Catal.*, 2008, **47**, 73-83.
57. C. Coutanceau, S. Brimaud, C. Lamy, J. M. Leger, L. Dubau, S. Rousseau and F. Vigier, *Electrochim. Acta*, 2008, **53**, 6865-6880.
58. E. Antolini, *J. Power Sources*, 2007, **170**, 1-12.
59. P. N. Ross, K. Kinoshita, A. J. Scarpellino and P. Stonehart, *J. Electroanal. Chem. Interfacial Electrochem.*, 1975, **59**, 177-189.
60. P. N. Ross, K. Kinoshita, A. J. Scarpellino and P. Stonehart, *J. Electroanal. Chem. Interfacial Electrochem.*, 1975, **63**, 97-110.
61. S. Wasmus and A. Kuver, *J. Electroanal. Chem.*, 1999, **461**, 14-31.
62. S. Srinivasan, R. Mosdale, P. Stevens and C. Yang, *Annu. Rev. Energy Env.*, 1999, **24**, 281-328.

63. N. M. Markovic, H. A. Gasteiger, P. N. Ross Jr, X. Jiang, I. Villegas and M. J. Weaver, *Electrochim. Acta*, 1995, **40**, 91-98.
64. C. Hiromi, M. Inoue, A. Taguchi and T. Abe, *Electrochim. Acta*, 2011, **56**, 8438-8445.
65. M. Inoue, H. Shingen, T. Kitami, S. Akamaru, A. Taguchi, Y. Kawamoto, A. Tada, K. Ohtawa, K. Ohba, M. Matsuyama, K. Watanabe, I. Tsubone and T. Abe, *J. Phys. Chem. C*, 2008, **112**, 1479-1492.
66. M. Hara, Y. Hatano, T. Abe, K. Watanabe, T. Naitoh, S. Ikeno and Y. Honda, *J. Nucl. Mater.*, 2003, **320**, 265-271.
67. E. Antolini, F. Colmati and E. R. Gonzalez, *Electrochem. Commun.*, 2007, **9**, 398-404.
68. E. M. Cunha, J. Ribeiro, K. B. Kokoh and A. R. de Andrade, *Int. J. Hydrogen Energy*, 2011, **36**, 11034-11042.
69. H. Wang, Z. Jusys and R. J. Behm, *J. Power Sources*, 2006, **154**, 351-359.
70. Y. Takasu, N. Yoshinaga and W. Sugimoto, *Electrochem. Commun.*, 2008, **10**, 668-672.
71. W. Du, Q. Wang, D. Saxner, N. A. Deskins, D. Su, J. E. Krzanowski, A. I. Frenkel and X. Teng, *J. Am. Chem. Soc.*, 2011, **133**, 15172-15183.
72. J. Matthey, *Platinum Today: London*; <http://www.platinum.matthey.com/> (accessed June 13, 2011).
73. A. Capon and R. Parson, *J. Electroanal. Chem. Interfacial Electrochem.*, 1973, **44**, 1-7.

74. A. Capon and R. Parsons, *J. Electroanal. Chem. Interfacial Electrochem.*, 1973, **44**, 239-254.
75. A. Capon and R. Parsons, *J. Electroanal. Chem. Interfacial Electrochem.*, 1973, **45**, 205-231.
76. A. Capon and R. Parsons, *J. Electroanal. Chem. Interfacial Electrochem.*, 1975, **65**, 285-305.
77. H. Miyake, T. Okada, G. Samjeske and M. Osawa, *PCCP*, 2008, **10**, 3662-3669.
78. X. Yu and P. G. Pickup, *Electrochem. Commun.*, 2009, **11**, 2012-2014.
79. X. Yu and P. G. Pickup, *Electrochem. Commun.*, 2010, **12**, 800-803.
80. J. L. Haan, K. M. Stafford, R. D. Morgan and R. I. Masel, *Electrochim. Acta*, 2010, **55**, 2477-2481.
81. X. Yu and P. G. Pickup, *Electrochim. Acta*, 2010, **55**, 7354-7361.
82. X. Yu and P. G. Pickup, *J. Power Sources*, 2011, **196**, 7951-7956.
83. X. Yu and P. G. Pickup, *Electrochim. Acta*, 2011, **56**, 4037-4043.
84. A. Lopez-Cudero, F. J. Vidal-Iglesias, J. Solla-Gullon, E. Herrero, A. Aldaz and J. M. Feliu, *J. Electroanal. Chem.*, 2009, **637**, 63-71.
85. B. E. Hayden, *Catal. Today*, 1997, **38**, 473-481.
86. B. Losiewicz, R. Jurczakowski and A. Lasia, *Electrochim. Acta*, 2011, **56**, 5746-5753.
87. G. Jerkiewicz, *Electrocatalysis*, 2010, **1**, 179-199.
88. Z. Liu, L. Hong, M. P. Tham, T. H. Lim and H. Jiang, *J. Power Sources*, 2006, **161**, 831-835.

89. R. L. Borup, J. R. Davey, F. H. Garzon, D. L. Wood and M. A. Inbody, *J. Power Sources*, 2006, **163**, 76-81.
90. G. A. Gruver, *J. Electrochem. Soc.*, 1978, **125**, 1719-1720.
91. K. H. Kangasniemi, D. A. Condit and T. D. Jarvi, *J. Electrochem. Soc.*, 2004, **151**, E125-E132.
92. E. Antolini, *Appl. Catal., B*, 2009, **88**, 1-24.
93. E. S. Steigerwalt, G. A. Deluga, D. E. Cliffel and C. M. Lukehart, *J. Phys. Chem. B*, 2001, **105**, 8097-8101.
94. S. L. Knupp, W. Li, O. Paschos, T. M. Murray, J. Snyder and P. Haldar, *Carbon*, 2008, **46**, 1276-1284.
95. C. K. Chiang, Y. W. Park, A. J. Heeger, H. Shirakawa, E. J. Louis and A. G. MacDiarmid, *J. Chem. Phys.*, 1978, **69**, 5098-5104.
96. A. Pron and P. Rannou, *Prog. Polym. Sci.*, 2002, **27**, 135-190.
97. H. Shirakawa, A. McDiarmid and A. Heeger, *Chem. Commun.*, 2003, 1-4.
98. A. G. Macdiarmid, J. C. Chiang, A. F. Richter and A. J. Epstein, *Synth. Met.*, 1987, **18**, 285-290.
99. L.-M. Huang, C.-H. Chen, T.-C. Wen and A. Gopalan, *Electrochim. Acta*, 2006, **51**, 2756-2764.
100. S. H. Glarum and J. H. Marshall, *J. Electrochem. Soc.*, 1987, **134**, 142-147.
101. L.-X. Wang, X.-G. Li and Y.-L. Yang, *React. Funct. Polym.*, 2001, **47**, 125-139.
102. L. F. Warren and D. P. Anderson, *J. Electrochem. Soc.*, 1987, **134**, 101-105.

103. W. J. Feast, J. Tsibouklis, K. L. Pouwer, L. Groenendaal and E. W. Meijer, *Polymer*, 1996, **37**, 5017-5047.
104. F. T. A. Vork, L. J. J. Janssen and E. Barendrecht, *Electrochim. Acta*, 1987, **32**, 1187-1190.
105. J. Roncali, *Chem. Rev.*, 1992, **92**, 711-738.
106. Y.-J. Wang, D. P. Wilkinson and J. Zhang, *Chem. Rev.*, 2011, **111**, 7625-7651.
107. P. Justin and G. Ranga Rao, *Int. J. Hydrogen Energy*, 2011, **36**, 5875-5884.
108. J. H. Ma, Y. Y. Feng, J. Yu, D. Zhao, A. J. Wang and B. Q. Xu, *J. Catal.*, 2010, **275**, 34-44.
109. I.-S. Park, K.-S. Lee, Y.-H. Cho, H.-Y. Park and Y.-E. Sung, *Catal. Today*, 2008, **132**, 127-131.
110. M. Li, A. Kowal, K. Sasaki, N. Marinkovic, D. Su, E. Korach, P. Liu and R. R. Adzic, *Electrochim. Acta*, 2010, **55**, 4331-4338.
111. A. Oliveira Neto, M. Brandalise, R. R. Dias, J. M. S. Ayoub, A. C. Silva, J. C. Penteado, M. Linardi and E. V. Spinace, *Int. J. Hydrogen Energy*, 2010, **35**, 9177-9181.
112. P. Ochal, J. L. Gomez de la Fuente, M. Tsyppkin, F. Seland, S. Sunde, N. Muthuswamy, M. Ronning, D. Chen, S. Garcia, S. Alayoglu and B. Eichhorn, *J. Electroanal. Chem.*, 2011, **655**, 140-146.
113. J. Wang, *Analytical Electrochemistry*, John Wiley & Sons, Inc, 2000, chapter 2.
114. A. Bard and L. Faulkner, *Electrochemical Methods: Fundamentals and Applications*, John Wiley & Sons, Inc, 2001, chapter 5.

115. E. Barsoukov and J. R. Macdonald, *Impedance Spectroscopy: Theory, Experiment, and Applications (2nd Edition)*, Wiley, Hoboken, NJ, USA, 2005, chapter 1.
116. A. Bard and L. Faulkner, *Electrochemical Methods: Fundamentals and Applications*, John Wiley & Sons, Inc, 2001, chapter 10.
117. X. Ren and P. G. Pickup, *Electrochim. Acta*, 2001, **46**, 4177-4183.
118. M. C. Lefebvre, R. B. Martin and P. G. Pickup, *Electrochem. Solid-State Lett.*, 1999, **2**, 259-261.
119. X. Liu and P. G. Pickup, *J. Power Sources*, 2008, **176**, 410-416.

Chapter 2

**Electrochemical impedance study of
the polymerization of pyrrole on high
surface area carbon electrodes**

Chapter 2. Electrochemical impedance study of the polymerization of pyrrole on high surface area carbon electrodes

This work has been published in part as *Moghaddam, R.B. and Pickup P.G., Electrochemical impedance study of the polymerization of pyrrole on high surface area carbon electrodes, Physical Chemistry Chemical Physics 2010, 12, 4733–4741*. The text was written in part by Dr. Peter Pickup.

2.1. Introduction

Studies on conducting polymers (CPs) such as polypyrrole, polyaniline and polythiophene have long been of great scientific interest.¹⁻⁸ In fact, this class of materials possess impressive characteristics such as mechanical stability, remarkable ionic/electronic conductivities, and a wide range of electrochemical applications. On account of these characteristics, CPs have found a great deal of multidisciplinary applications; they have been extensively used in fabrication of anti-static and anti-corrosion coatings, sensors, batteries and supercapacitors, light emitting diodes (LEDs),⁹ solar cells,¹⁰ electrochromic devices,¹¹ and transparent electrode materials.¹²

Conducting polymers are used as electrode materials in a variety of applications, particularly in the general areas of electroanalysis and energy storage/conversion, which generally require high surface area electrodes. Although conducting polymers can be fabricated in a number of porous, high-area forms, there are significant advantages to using a high area carbon support, such as carbon black or carbon nanotubes. Such

supports can enhance mechanical stability, as well as conductivity and the electrochemical utilization of the polymer (e.g. in a supercapacitor).¹³⁻²³

Among the most commonly studied CPs, polypyrrole (PPy) has gained special attention as it has numerous advantages such as desirable redox properties, the ability to give high electrical conductivities, and environmental stability. Owing to the attractive properties of PPy, study of this CP is of great importance (see section 1.1.5.2 for more detailed discussion of PPy).²⁴⁻²⁷

Electrochemical impedance spectroscopy is a powerful technique to investigate the electronic properties of the doped (conducting) and undoped (non-conducting) states of conducting polymers.^{28, 29} Numerous studies have been devoted to polypyrrole and its derivatives including documentaries on their capacitive behaviour,³⁰⁻³³ and ion and electron transport.^{29, 32-38} There is a large body of research on simulating the impedance spectra.^{29, 39-62} Impedance spectroscopy is commonly used to probe the electrochemical characteristics of conducting polymer composites with high surface area carbon. Much of this work has been for the characterization of electrode materials for supercapacitors, where impedance measurements provide the frequency dependence of the capacitance and information on electrode and cell resistances.^{19, 30, 63-69} There has also been a number of more fundamental studies that reveal important details regarding ion and electron transport within conducting polymer/carbon composites, as well as interfacial characteristics.⁷⁰⁻⁷² By analogy with work on planar conducting polymer films, it can be anticipated that such studies would also provide insight into the structures of the composites that could not be obtained by other means.^{32, 73}

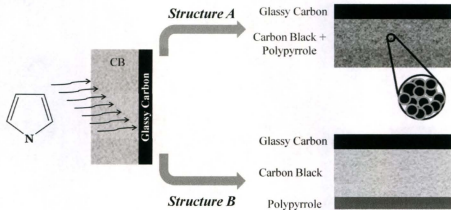


Figure 2-1. Schematic diagrams of two of the limiting structures possible for the electrodeposition of polypyrrole on a carbon black layer. A: Uniform deposition over the carbon black (CB) particles; B: Deposition on the outer surface of the CB layer.

Electrochemical impedance spectroscopy was used here to study the morphologies and electrochemical properties of polypyrrole films prepared potentiostatically, galvanostatically, and potentiodynamically. Using high surface area carbon black (CB; Vulcan XC-72) as a porous substrate for the polymerization, this work is focussed on probing the location of the polypyrrole and how evenly it is distributed over the porous structure of the carbon black. The two extreme possibilities are that the polypyrrole could be evenly distributed as a very thin layer over the entire surface area of the CB (Structure A), or that it could be deposited as a thick film on the outer surface of the CB layer (Structure B). These two structures are illustrated in figure 2-1. In general, the actual structures of the CB/PPy composites will be between these two extremes. A

third limiting structure, with a polypyrrole layer between the GC surface and the carbon black layer is thought to be highly unlikely. Impedance spectroscopy has been used to infer the location of the polypyrrole via its influence on the charge transfer and Warburg impedances of the electrodes.

2.2. Experimental

2.2.1. Chemicals

Analytical grade sodium perchlorate (Sigma Aldrich) was used as received. Vulcan XC-72 (density of 0.264 g cm^{-3} ; specific area $\sim 200 \text{ m}^2 \text{ g}^{-1}$) was obtained from Cabot Corporation and used without purification. Pyrrole (Analytical grade, Sigma Aldrich) was purified by passing through an alumina column prior to use. Distilled and deionized water was used throughout the experiments. All measurements were recorded under a nitrogen atmosphere following purging for 15 min.

2.2.2. Instrumentation

Scanning electron microscopy (SEM) was performed with a Model FEI Quanta 400 environmental SEM. Electrochemical studies consisting of cyclic voltammetry and electrochemical impedance spectroscopy were carried out in a conventional three-electrode cell with a Model 273A EG&G Potentiostat/Galvanostat and Model 5210 Lock-in Amplifier. The system was run by a PC through M270 commercial software for voltammetric measurements and Power-Suite commercial software was used for electrochemical impedance spectroscopy. Electrochemical impedance measurements

were performed over the range of 10 kHz to 10 MHz using an ac amplitude of 10 mV. Before any impedance measurement, the electrode was held for 2 min at the dc offset potential to reach electrochemical equilibrium. Selected experiments were repeated to confirm that a steady-state had been achieved. The working electrode potential was monitored against a Saturated Calomel Electrode (SCE) and a platinum wire formed the counter electrode. A glassy carbon (GC) working electrode (area = 0.071 cm²) was used for all experiments. Porous, high surface area working electrodes were prepared by coating the GC electrode with a drop of a Vulcan XC-72/Nafion/methanol mixture (loading of ca. 0.001 g cm⁻²). A cyclic voltammogram of each carbon black coated glassy carbon (CB) electrode was obtained in 0.5 M NaClO₄(aq) prior to polypyrrole deposition to confirm that a similar loading of carbon black was used for all experiments.

2.2.3. Electrochemical polymerization of pyrrole

In all cases, pyrrole was polymerized in an aqueous solution of 0.5 M pyrrole with 0.5 M NaClO₄ as the supporting electrolyte.

Potentiodynamic polymerization: A cyclic potential sweep range of -0.2 to +0.8 V (anodic as the forward sweep) and a scan rate of 50 mV s⁻¹ were used in all potentiodynamic polymerizations. PPCB-cv2, PPCB-cv4, PPCB-cv6, and PPCB-cv8 are used to designate electrodes prepared using 2, 4, 6 and 8 continuous cyclic scans, respectively.

Potentiostatic polymerization: A constant potential of 0.6 V vs. SCE was applied for 500 s to produce an electrode designated as PPCB-cp. As well, in a pulsed regime, a constant

potential of +0.6 V was applied in 4 periods of 125 s, each of which was followed by a 125 s interval at $E = 0$ V to obtain the PPCB-pp electrode.

Galvanostatic polymerization: A constant anodic current density of 0.88 mA cm^{-2} was used to pass a charge of 0.22 C cm^{-2} for PPCB-cc1 (250 s), 0.48 C cm^{-2} for PPCB-cc2 (545 s), or 0.88 C cm^{-2} for PPCB-cc3 (1000 s).

2.3. Results and discussion

2.3.1. Potentiodynamic polymerization

The striking contrast between the voltammetric polymerization of pyrrole on a bare GC electrode, shown in figure 2-2, and that on a carbon black coated glassy carbon (CB) electrode, shown in figure 2-3, was the incentive to initiate and develop this study, and provided evidence for a strong dependence of the polymerization pathway on the electrode structure. In the first cycle, the onset of pyrrole oxidation occurred earlier (*ca.* +0.4 V) at the CB electrode than at the bare GC electrode (*ca.* +0.6 V), which could be ascribed to facilitated initial oxidation (*i.e.* nucleation) of pyrrole on the CB. This could further also originate, in part, from faster electron transfer for the CB. Furthermore, a substantially larger current value for the CB at the switching potential was recorded (5.4 mA vs. 1.3 mA for the bare GC), which can be attributed to the much higher surface area and/or facile electron transfer for the CB. Further insight into differences in nucleation rates can be inferred from the return scans on the first cycles of the two supports. At both electrodes, the anodic current at the beginning of the return scan was higher than for the forward scan, indicating that there had been nucleation of polypyrrole deposition.

However, the cathodic current between *ca.* +0.35 and -0.2 V for reduction of the deposited polypyrrole was much lower (by a factor of *ca.* 10) at the GC electrode than at the CB electrode.

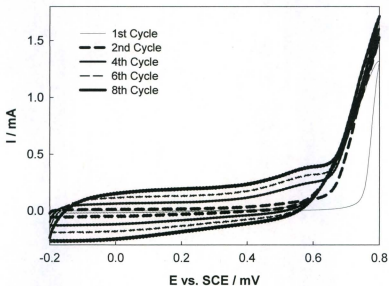


Figure 2-2. Polymerization voltammograms (50 mV s^{-1}) for 0.5 M pyrrole in 0.5 M $\text{NaClO}_4(\text{aq})$ at a bare GC electrode.

Inspection of the subsequent polymerization cycles provides additional information. The polymerization of pyrrole at the GC electrode on the second cycle showed significantly larger current (+0.65 - 0.8 V) than on the first scan. The polymerization current on the subsequent scans also showed gradual increase with cycle number, but not similar to the sharp increase from the first to the second scan. This

clearly is indicative of a different polymerization step (*i.e.* nucleation) at the first scan, which was followed by deposition of additional polymeric layers during the subsequent scans. This can further be supported by the steadily increasing currents seen for reduction and re-oxidation of the polypyrrole film between +0.6 and -0.2 V. The similarity of the return scans for all the cycles is due to the fact that the polymerization of pyrrole proceeds through an oxidative mechanism, which markedly affects the anodic sweeps, but not the cathodic sweeps.

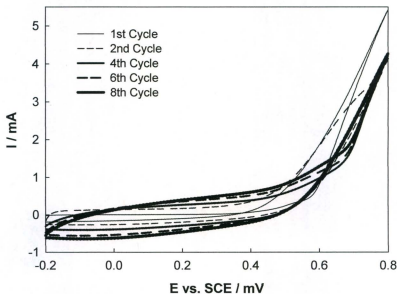


Figure 2-3. Polymerization voltammograms (50 mV s^{-1}) for 0.5 M pyrrole in 0.5 M $\text{NaClO}_4(\text{aq})$ at a CB-coated GC electrode.

Nevertheless, the voltammetric polymerization of pyrrole on CB generated a different pattern. Here after the nucleation scan on the first cycle, the current for pyrrole polymerization (*i.e.* at $E > +0.6$ V) decreased on the subsequent cycles. This can be understood by closer inspection of the second scan. The polymerization current on the forward leg initially followed that on the first return scan, as for the GC electrode, indicating further polypyrrole deposition on the layer formed in the first scan. However, at potentials above *ca.* $+0.6$ V, the current did not increase as steeply, and transitioned to the lower profile seen on subsequent scans. This can be explained by depletion of the pyrrole monomer within the CB layer and/or inhibited diffusion of the monomer. Based on the charge passed during the first cycle ($\sim 3.0 \times 10^{-2}$ C) and taking 2.23 as the number of electrons involved in the polymerization of each pyrrole unit,³⁴ it can be estimated that 1.4×10^{-7} mol of pyrrole was consumed. This is an order of magnitude higher than the amount initially within the *ca.* $4 \mu\text{m}$ CB layer (GC area = 0.071 cm^2 and pyrrole density $\sim 0.97 \text{ g cm}^{-3}$), shown in figure 2-4.

Therefore, sustained polymerization of polypyrrole throughout the CB layer on subsequent scans would require sufficient diffusion of pyrrole from the bulk solution into the layer during the part of the cycle between $+0.6$ and -0.2 V (32 s). It would appear from the voltammograms in figure 2-3 that there was not sufficient time for complete replenishment of the pyrrole within the CB layer. In addition, pyrrole diffusing from the bulk solution would be expected to deposit preferentially close to the CB layer|solution interface, where its accumulation could begin to block access to the CB layer. This would have led to formation of a structure approaching limiting structure B (see figure 2-1). The

voltammograms in figure 2-3 strongly suggest that there was a transition from deposition on the entire CB surface (Structure A; figure 2-1) to deposition primarily at the CB layer|solution interface (Structure B).

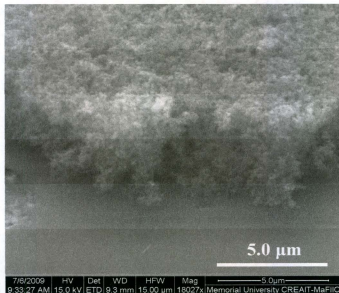


Figure 2-4. SEM image (cross sectional/45° view) for a CB coated GC electrode (~ 1 mg cm⁻²).

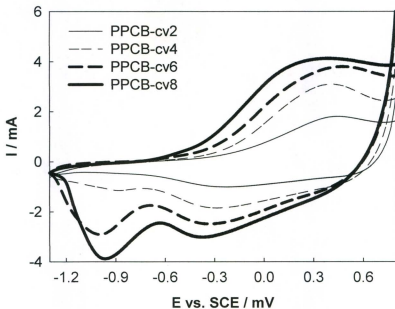


Figure 2-5. Comparative CVs at 200 mV s^{-1} of the PPCB-cv2, PPCB-cv4, PPCB-cv6 and PPCB-cv8 electrodes in $0.5 \text{ M NaClO}_4(\text{aq})$.

Figure 2-5 shows overlaid voltammograms for the PPCB-cv electrodes prepared using 2, 4, 6, and 8 consecutive cyclic scans. These voltammogram were started at $+0.8 \text{ V}$ with no equilibration at this potential in order to show the initial un-doping behaviour of the polypyrrole. The forward sweeps (cathodic) were initiated by a broad reduction signal which is due to the transition of the polypyrrole films from conducting to non-conducting states. This peak, which was centered at *ca.* -0.22 V for PPCB-cv2 and shifted to more negative potentials for the subsequent electrodes, was followed by a second reduction

peak at ~ -1 V presumably due to cation insertion.³⁴ A single broad oxidation peak formed the dominant feature of the reverse scan for all the electrodes, which represents the re-oxidation of the PPy to its conducting state. It is noteworthy that the center of the anodic wave and its onset appreciably shifted to less positive potentials from PPCB-cv2 to PPCB-cv8. This could originate from accelerated electronic/ionic transport, and/or be explained by improvement in the structure towards the end of the 8-cycle polymerization.

The cathodic waves at *ca.* -0.25 and 1 V correspond to the reduction of polypyrrole accompanied by ClO_4^- expulsion and Na^+ insertion, respectively. Re-oxidation of the polypyrrole on the anodic sweep solely involves insertion of ClO_4^- for charge compensation.³⁴ Thus, the -1 V wave can be attributed to cation insertion into the polypyrrole structure. This cation insertion signal became more pronounced for the higher loadings of polypyrrole in the PPCB-cv electrodes, and this can be due to larger $\text{NaClO}_4(\text{aq})$ accumulation within the PPCB layer within the higher quantities of the reduced polypyrrole (ClO_4^- is released into the pores, while charge compensating Na^+ migrates into the layer).

To investigate the effects of scan rate on the voltammetric features, typical CVs for a PPCB-cv8 layer recorded at various scan rates are shown in figure 2-6. Obviously, all three peaks shifted to more extreme potentials with increasing scan rate (more negative for the cathodic peaks and more positive for the anodic peak), which should be simply due to an increasing influence of the film resistance at higher scan rates. However, the most notable observation is the change in the relative peak heights for the two consecutive cathodic waves. In fact, the current of the cation insertion signal, located at

more negative potentials, increased more significantly than its anion expulsion counterpart. That is, the anion expulsion current increased from -0.78 mA at 40 mV s^{-1} to -3.0 mA at 200 mV s^{-1} , while the corresponding currents for the cation insertion were -0.75 and -3.9 mA . This interesting effect could be most likely ascribed to highly resistive anion expulsion, leading to the cation insertion process becoming more pronounced at higher scan rates.

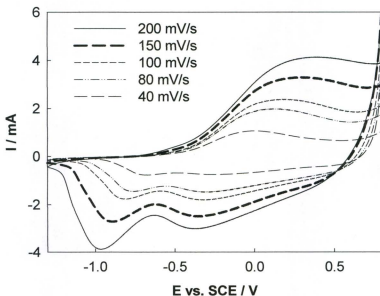


Figure 2-6. Cyclic voltammograms for a PPCB-cv8 electrode at various potential sweep rates.

Comparative voltammetric responses of the PPCB-cv electrodes (figure 2-5) clearly indicate a trend of improvement in the electrochemical properties with the polymerization cycle number (*e.g.* negative shift of the oxidation peak). This could originate from improvements in the electronic/ionic conductivity of the PPCB-cv films, with the PPCB-cv8 and PPCB-cv2 being supposedly superior and inferior to the other composite electrodes. To investigate this further, electrochemical impedance spectroscopy was used to measure film resistances with the expectation that these would provide insight into the evolution of the PPCB structure.

Comparative complex-plane impedance (Nyquist) plots for the PPCB-cv2, PPCB-cv4, PPCB-cv6, and PPCB-cv8 electrodes are shown in figure 2-7. An offset potential of +0.3 V vs. SCE (or -0.1 V; see below) was used here in order to ensure that the polypyrrole was in a highly conducting state and to avoid instability due to over-oxidation (oxidative degradation) that would occur at higher potentials. The general pattern of the Nyquist plots remained constant regardless of the polymerization cycle number (and offset potential of -0.1 or +0.3 V). At high frequencies, all of the Nyquist plots are dominated by the uncompensated solution ohmic resistance (R_s) and a charge transfer resistance (R_{CT}) in parallel with a double layer capacitance (C_{DL}). This region became insignificant and the real impedance value associated with the RC loop decreased for electrodes prepared with higher cycle numbers, clearly due to a decrease of the R_{CT} . Presumably due to the accelerated charge transfer, this effect can account for the unusual negative shift of the re-oxidation peaks in the CVs (figure 2-5) with increasing cycle number.

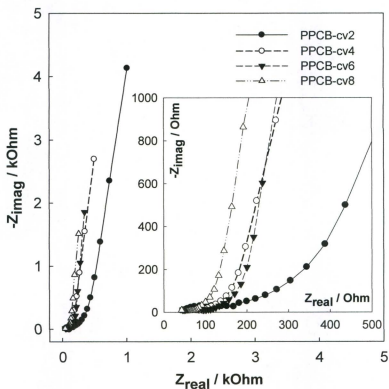


Figure 2-7. Nyquist profiles recorded at $E = +0.3$ V in 0.5 M $\text{NaClO}_4(\text{aq})$ for the PPCB-cv2, PPCB-cv4, PPCB-cv6 and PPCB-cv8 electrodes; inset: expanded high frequency region.

The intermediate frequency impedance for all the PPCB-cv electrodes comprises of a Warburg-type line ($\sim 45^\circ$), characteristic of the porous substrates. It can be observed that this line for the PPCB-cv2 electrode was the longest, while its length decreased with the polymerization cycle number. However, overlap of this region with the high and low

frequency impedances makes the visual judgement uncertain. That is, more accurate interpretation of the changes requires quantitative evaluation (*i.e.* fitting) of the impedance data (see below).

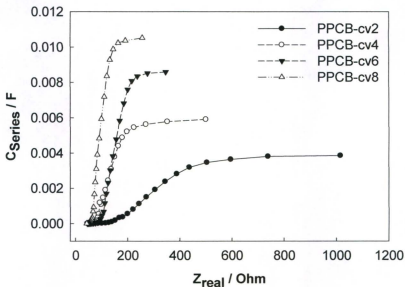


Figure 2-8. Capacitance plots (series capacitance as a function of the real impedance) recorded at $E = +0.3$ V in 0.5 M $\text{NaClO}_4(\text{aq})$ for the PPCB-cv2, PPCB-cv4, PPCB-cv6 and PPCB-cv8 electrodes.

A capacitive-type feature ($\sim 90^\circ$ line) at low frequencies terminates the Nyquist profile for all the PPCB-cv layers. The capacitive responses of the PPCB-cv electrodes can best be visualized using the capacitance plots (series capacitance vs. real impedance), shown in figure 2-8 ($E = +0.3$ V). Such plots are particularly important for assessing the

potential of materials for use in supercapacitors, since they clearly show how much resistance (x-axis) is associated with accessing the capacitance of the material (y-axis). As expected, the limiting capacitance for the PPCB-cv electrode (low frequency/high real impedance limit) increased with the number of the polymerization cycles. The low real impedance region, which demonstrates the paralleled charge transfer resistance to the double layer capacitor, displays the same trend given by the corresponding Nyquist profiles, with PPCB-cv8 and PPCB-cv2 showing the smallest and largest resistances, respectively. Nevertheless, inspection of the intermediate frequency (or intermediate real impedance) of the capacitance plots would provide information about the resistance associated with the PPCB layers. As a matter of fact, the slope of this region is proportional to the conductivity (the smaller of the ionic or electronic conductivity) of the layer.³³ It can be seen that the slope of this portion increased from PPCB-cv2 to PPCB-cv6, while the PPCB-cv6 and PPCB-cv8 electrodes both gave similar slopes. This further indicates that the electronic/ionic resistance of the PPCB layer decreased with the polymerization cycle number, which could be ascribed to a transition from the structure B to structure A in the course of the potentiodynamic polymerization.

As noted earlier, it is necessary to quantify the impedance profiles for a more clear assessment. Quantitative investigation of the impedance data were carried out using two approaches. In a preliminary method, parameters were estimated from the dimensions of the individual features of the Nyquist plots. Thus R_s , R_{CT} and C_{DL} were obtained by fitting a semicircle to the charge transfer region (RC), while the resistance associated with the Warburg region provided an estimate of the resistance of the PPCB

layer (R_L) and the capacitance of the layer (C_L) was obtained as the low-frequency limiting value of $-1/\omega Z_{\text{imag}}$ (ω = radial frequency; Z_{imag} = imaginary impedance). With these estimates in hand, the impedance data were then fitted to the equivalent circuit shown in figure 2-9,³⁶ with a constant phase element to model C_{DL} and a generalized finite Warburg element to model the non-ideal Warburg-type behaviour of the layer.

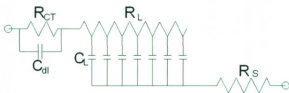


Figure 2-9. Equivalent circuit used to fit the impedance data.

Figure 2-10 shows the overlaid fitting and experimental results for PPCB-cv4 at -0.1 V, as a sample, to illustrate the quality of the fitting. The results from both approaches are presented in Table 2-1 (also see appendix, figures A-1 to A-7, for the complete fitting results compared with the experimental data for the PPCB-cv electrodes at -0.1 and +0.3 V). Data at an offset potential of -0.1 V are also included in Table 2-1 to show the sensitivity of the parameters to the oxidation level of the polypyrrole. The model in figure 2-9 is a simplification of the circuit needed for a rigorous description of the system, but it does provide reasonable fits to the data, and the parameters extracted are useful for documenting the trends in behaviour discussed below. In general, the parameters determined by the two methods described above are in reasonable agreement, and so

either set can be used. In cases of large discrepancies, the values from both methods should be regarded as semi-quantitative.

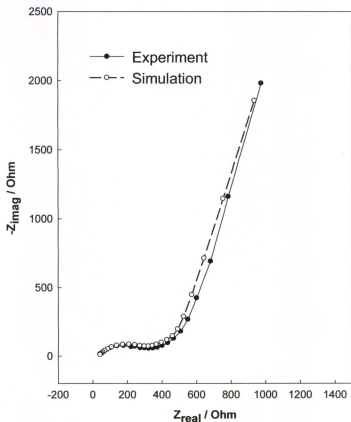


Figure 2-10. Comparison of experimental and simulated (ZView2, Scribner Associates Inc.) impedance data for PPCB-cv4 at -0.1 V. The fitting parameters were: $R_S = 43.3 \Omega$, $R_{CT} = 251 \Omega$, $CPE-T(Q_0 \text{ or } Y_0) = 5.7 \times 10^{-5} \text{ S s}^{0.67}$, $CPE-P(\alpha \text{ or } n) = 0.67$, $R_L = 552 \Omega$, $C_L = 6.6 \text{ mF}$ and $W-P = 0.42$.

Table 2-1 Parameters from impedance data for the PPCB-cv electrodes.

| Cycles | E / V | R _S / Ω | | R _{CT} / Ω | | R _L / Ω | | | C _L / mF | |
|--------|-------|--------------------|-----|---------------------|-----|----------------------|------|------|---------------------|------|
| | | RC | fit | RC | fit | C _{DL} / μF | 45° | fit | -1/ωZ'' | fit |
| 2 | -0.1 | 39 | 36 | 246 | 114 | 3.9 | 1989 | 1106 | 4.4 | 2.7 |
| 4 | -0.1 | 37 | 34 | 272 | 251 | 5.0 | 642 | 552 | 8 | 6.6 |
| 6 | -0.1 | 33 | 30 | 202 | 183 | 4.9 | 507 | 321 | 11.8 | 10.1 |
| 8 | -0.1 | — | 35 | — | 50 | — | 213 | 219 | 14.8 | 12.9 |
| 2 | +0.3 | 41 | 42 | 109 | 85 | 4.0 | 756 | 567 | 3.9 | 3.8 |
| 4 | +0.3 | 19 | 36 | 88 | 42 | 1.2 | 225 | 184 | 5.9 | 4.9 |
| 6 | +0.3 | 38 | 35 | 73 | 62 | 4.4 | 255 | 201 | 8.6 | 7.5 |
| 8 | +0.3 | — | 38 | — | 20 | — | 156 | 131 | 10.5 | 8.9 |

— Could not be determined.

R_S: uncompensated ohmic resistance

R_{CT}: charge transfer resistance

C_{DL}: double layer capacitance

R_L: layer resistance

C_L: layer capacitance

As suggested by visual examination of the Nyquist plots in figure 2-7, the charge transfer resistances listed in Table 2-1 can generally be seen to decrease with the number

of cycles applied for the polymerization. This phenomenon is consistent with the unusual shift of the anodic peak in the voltammograms seen in figure 2-5, which moves to lower potentials at higher polypyrrole loadings. R_{CT} values were all lower at +0.3 V than -0.1 V, showing some sensitivity to the oxidation state of the polymer. The double-layer capacitances associated with R_{CT} range from 4 to 5 μF (except for one anomalous result), which corresponds to 56–70 $\mu\text{F cm}^{-2}$ based on the area of the glassy carbon support. It is therefore too high to be reasonably attributed to the GC surface alone. On the other hand, the double-layer capacitance of the CB is much higher (0.4 mF was measured for an electrode with no polypyrrole), indicating that R_{CT} is not associated with the entire CB surface. In a previous report,³⁶ the charge transfer resistance seen for polypyrrole was attributed to the electrode/polypyrrole interface. Under the conditions employed here, polypyrrole exhibited a negligible charge transfer resistance when deposited on Pt, while a significant R_{CT} is seen on GC (see figure 2-11). In the case of the polypyrrole/CB composites studied here, R_{CT} should be smaller than on GC because of the high surface area. The fact that quite large R_{CT} values were obtained (Table 2-1) suggested that they may include a component due to the electronic contact resistances between the CB particles. It is noteworthy to state that the experimental results summarized in Table 2-1 (and in the following tables) were repeated a number of times to test their reproducibility.

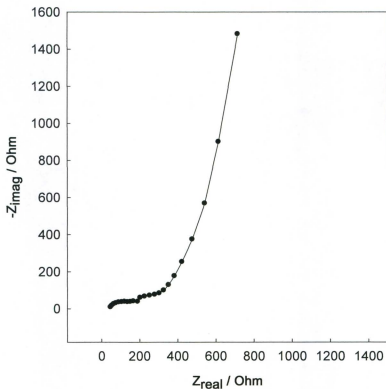


Figure 2-11. Nyquist plot for a polypyrrole coated glassy carbon electrode at +0.1 V in 0.5 M NaClO₄(aq).

The resistances of the PPCB layers (R_L) obtained from impedance spectroscopy strongly decreased with increasing polypyrrole loading (Table 2-1). The trend is the same at both -0.1 and +0.3 V, and in the values obtained from both the length of the Warburg-type impedance ($\sim 45^\circ$ line) in the Nyquist plots and from fitting of the whole data set.

Since this resistance should represent the ionic resistance of the polypyrrole film, it should increase with polypyrrole loading (*i.e.* film thickness) if the polypyrrole is deposited as a layer on top of (or less likely underneath) the CB layer, as in Structure B. If the polypyrrole is deposited primarily over the CB particles (Structure A), the ionic resistance of the layer would be determined by a combination of the resistance of the electrolyte solution within the pores and the resistance of the polypyrrole film over the particles. At low loadings (very thin films), the polypyrrole resistance could be negligible, and R_L could be independent of the loading (but could not decrease). However, at higher loadings the polypyrrole resistance would become more significant and the resistances of the pores would increase as they contract and interconnections become blocked with polypyrrole. This would result in an increasing R_L with increasing loading.

The only reasonable explanation for the decreasing R_L appears to be that it represents the electronic resistance of the PPCB layer. This conclusion is supported by the impedance of a CB layer (no polypyrrole) shown in figure 2-12. This layer exhibited a very large Warburg-like resistance that can only be due to poor electronic conductivity. This may arise from the use of the electronically insulating Nafion binder, which could result in significant contact resistances between carbon particles. The polymerization of polypyrrole around the particles would increase their electronic connectivity, and this would explain the trend in R_L . The decrease in all R_L values when the potential was increased to +0.3 V is consistent with this explanation, since the electronic conductivity of polypyrrole increases with increasing potential. Although, the ionic conductivity also

increases with potential, the effect would be too small³⁴ to account for the magnitude of the observed changes in R_L .

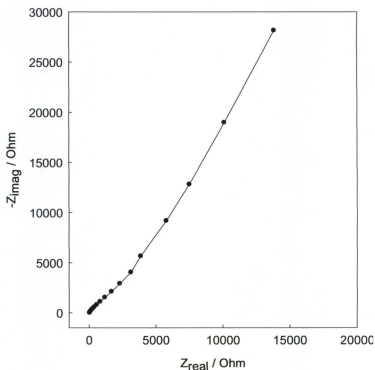


Figure 2-12. Nyquist plot for a carbon black coated glassy carbon electrode at +0.1 V in 0.5 M NaClO₄(aq).

The decreasing R_{CT} and R_L seen in Table 2-1 with increasing polymer loading strongly suggests that the polypyrrole was deposited primarily over the CB particles (Structure A), since deposition of the polypyrrole as a layer on top of (or underneath) the

CB layer (Structure B) should result in a constant R_{CT} . To visualize the structural evolution during the polymerization, representative SEM images for the CB (with no polypyrrole) and PPCB-cv2 and PPCB-cv6 electrodes are shown in figure 2-13. Herein, all three electrodes had been scratched to obtain cross sectional views of the PPCB composites. The agglomeration of the CB particles seen in the SEM images is consistent with the decrease in R_{CT} with the polymerization cycle number (see table 2-1). As the CB particles become embedded within the growing polymer particles, the connectivity of the polymer and CB composite material should increase, which could appear as a decreasing R_{CT} . The thickness of the CB layer (A) can be seen to be *ca.* 4 μm . The SEM image (45° view) of the PPCB-cv2 electrode (C) indicates that the film consists of two somewhat distinguishable layers, a densely packed structure in depth (thickness \sim 2 μm), on top of which spheres with *ca.* 0.5 μm diameter can be observed (thickness \sim 1 μm). Consistent with the polymerization CVs in figure 2-3, this suggests that the polymerization initially involved the entire CB layer, after which pyrrole was significantly depleted in depth of the layer (*i.e.* insufficient diffusion of pyrrole before the polymerization onsets on subsequent cycles) favouring the polymerization at the CB layer|solution interface during subsequent cycles. However, the SEM image for PPCB-cv6 displays a more homogeneous morphology, mainly consisting of spherical structures (diameter \sim 0.5 μm), which encompasses almost the entire layer. The structure evolution from PPCB-cv2 to PPCB-cv6 is consistent with the decrease in the resistance of the PPCB-cv layer (R_L values; Table 2-1) with increasing cycle number.

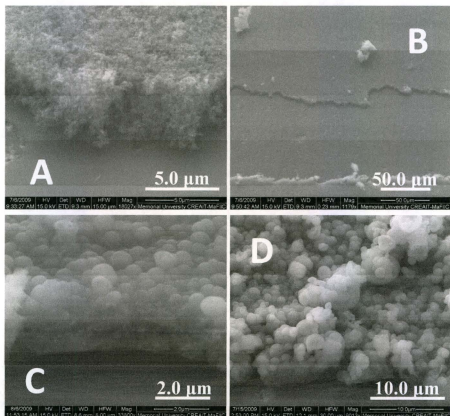


Figure 2-13. SEM images of a CB coated electrode (A and B) and similar electrodes coated with polypyrrole by using 2 (C; PPCB-cv2) and 6 (D; PPCB-cv6) polymerization cycles.

The SEM images shown in figure 2-13 provide strong evidence that the polypyrrole is deposited over the CB particles (Structure A), although there is also substantial deposition on top of the CB layer, as in Structure B. These observations, in combination with the depletion of the pyrrole monomer within the CB layer indicated by

the polymerization CVs (figure 2-3), suggest that polypyrrole deposition begins at the individual CB particles on the first polymerization cycle, but then occurs largely at the CB layer|solution interface during subsequent cycles.

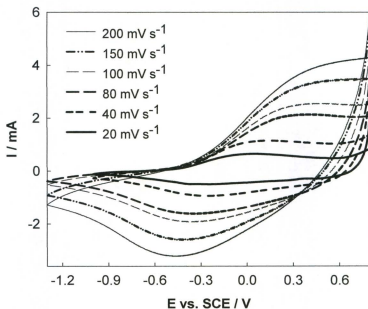


Figure 2-14. Typical cyclic voltammograms of a PPCB-cp electrode recorded at various potential sweep rates in 0.5 M NaClO₄.

2.3.2. Potentiostatic polymerization

In an attempt to fabricate composite films of lower resistance than the PPCB-cv layers, potentiostatic polymerization was also employed to electropolymerize pyrrole on CB (see experimental for details) substrates. In this respect, we tested several potentials (in the range of +0.55 to +0.65 V where polymerization was expected to actively occur based on the potentiodynamic polymerization CVs) to optimize the polymerization conditions. It was found that potentials higher than +0.6 V would lead to production of highly resistive PPy, while the polymerization rate (*i.e.* current) was too low at +0.6 V. Therefore, as stated in the experimental section, +0.6 V was chosen as the polymerization potential.

Typical cyclic voltammograms for a PPCB-cp electrode in 0.5 NaClO₄ are shown in figure 2-14. The forward scan (cathodic) at all scan rates is dominated by a very broad peak, characteristic of the conducting polymer voltammetry. This peak centered at ~ -0.25 V (at 40 mV s⁻¹) demonstrates the reduction of the PPy film to its non-conducting form. It is noteworthy that this reduction signal, involving the ClO₄⁻ expulsion, was the only significant feature of the cathodic scan. In fact, in contrast to the CVs for the PPCB-cv electrodes, no secondary reduction peak (*i.e.* assigned to the cation insertion) was observed at any scan rates. Re-oxidation of the reduced form to the conducting state occurred on the anodic scan, identified by the broad anodic peak centered at *ca.* +0.07 V (at 40 mV s⁻¹).

Nevertheless, the general shape of the voltammograms (*i.e.* noticeable peak separation) and the changes with increasing scan rate (*i.e.* appreciable shift in the peak

potentials for both the cathodic and anodic signals) point to a possible kinetic barrier for the doping/undoping process of the potentiostatically made polymer. Therefore, impedance spectroscopy was used for further exploration.

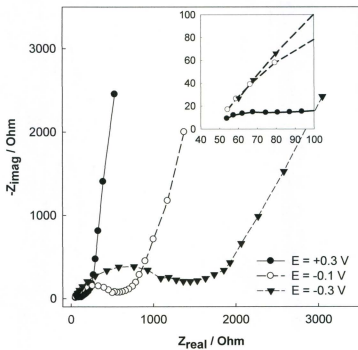


Figure 2-15. Complex-plane plots for a PPCB-cp electrode in 0.5 M NaClO₄ at various dc-offset potentials; inset: expanded high frequency region.

Figure 2-15 presents complex-plane (Nyquist) plots for a PPCB-cp electrode. Here three dc-offset potentials were chosen to investigate sensitivity of the film to the

oxidation state. The high frequency region at all potentials consists of the uncompensated ohmic resistance (R_S) and a charge transfer resistance (R_{CT}) paralleled with an electrical double layer capacitance (C_{DL}). The intermediate frequency for all cases is dominated by a Warburg-type behaviour ($\sim 45^\circ$) giving a measure of ionic or mixed ionic and electronic resistances, followed by a capacitive behaviour ($\sim 90^\circ$) at low frequencies. The high frequency regions of the Nyquist plots in figure 2-15 display a very significant dependence on the potential. At +0.3 V, the R_{CT} - C_{DL} (RC) region is very small and indicative of a low charge transfer resistance at this potential. In contrast, the diameter of the RC loop at -0.1 V dramatically increased, clearly indicative of a transition from a conducting to non-conducting form. Moreover, the RC region of the Nyquist was further expanded at -0.3 V.

For better understanding of the impedance data, the analysis/simulation approach described for the PPCB-cv layers (section 2.3.1) was used for the quantification of the impedance data recorded for the PPCB-cp electrode. The results are listed in Table 2-2 (also see appendix, figures A-8 to A-10, for the complete fitting results compared with the experimental data). Herein, since the high frequency regions of the Nyquist plots at -0.3 and -0.1 V were well-defined (*i.e.* forming a complete loop that is not depressed or distorted), both of the two quantification tools (*i.e.* estimated parameters from the dimensions of the individual features of the Nyquist plots as well as the results of fitting the impedance data to the equivalent circuit shown in figure 2-9) gave rise to quite consistent results for these two potentials. However, fitting of the high frequency region at +0.3 V with an RC element (*i.e.* a semicircle) was somewhat problematic.

The values of R_{CT} in Table 2-2 show a very strong dependence on the oxidation state of the polymer; that is, it has a value of 1473 Ω at -0.3 V (fit results; Table 2-2), while it decreased to 432 Ω at -0.1 and 65 Ω at +0.3 V. The midrange frequency resistance values, R_L , show acceptable consistency in the two fitting approaches, although some discrepancy at -0.1 V can be observed. However, the R_L seems to decrease with increasing potential even though its change was not as significant as for the R_{CT} . The data shown in Table 2-2 for the C_L values, describing the low frequency impedance of the PPCB-cp electrode, indicate that the limiting capacitance of the electrode did not remarkably change with potential over the range studied.

Table 2-2. Parameters from impedance data for a PPCB-cp electrode.

| E / V | R_S / Ω | | R_{CT} / Ω | | $C_{DL} / \mu F$ | R_L / Ω | | C_L / mF | |
|-------|----------------|-----|-------------------|------|------------------|----------------|-----|------------------|-----|
| | RC | fit | RC | fit | | 45° | fit | -1/ $\omega Z''$ | fit |
| +0.3 | 40 | 42 | — | 65 | 211 | 390 | 373 | 6.5 | 2.2 |
| -0.1 | 41 | 44 | 498 | 432 | 131 | 475 | 741 | 7.9 | 4.7 |
| -0.3 | 41 | 44 | 1366 | 1473 | 131 | 834 | 756 | 6.5 | 3.7 |

— Could not be determined.

R_S : uncompensated solution resistance

R_{CT} : charge transfer resistance

C_{DL} : double layer capacitance

R_L : layer resistance

C_L : layer capacitance

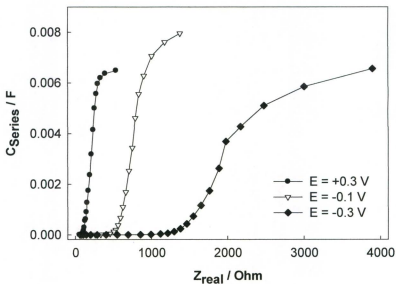


Figure 2-16. Series capacitance as a function of the real impedance for a PPCB-cp electrode in 0.5 M NaClO₄ at various dc-offset potentials.

To more clearly visualize the low frequency impedance of the PPCB-cp electrode, figure 2-16 presents capacitance profiles from the data in figure 2-15. In line with the Nyquist plots, the high frequency region at all potentials shows an appreciable increase of the real impedance without significant increase in the capacitance. It is noteworthy to stress that the offset along the real impedance is indicative of the R_{CT} , while the angle of this region with the Z_{real} axis gives a measure of C_{DL} . As a matter of fact, since C_{DL} is often very small, systems with high R_{CT} produce a “visually” horizontal line over the high frequency region in the capacitance plots. However, the capacitance profiles at +0.3

and -0.1 V had a quite sharp rising capacitance subsequent to the RC region, while that at -0.3 V was much less steep. Comparison of the limiting capacitances at -0.3, -0.1, and +0.3 V shows sensitivity to the potential value, with the profile at -0.1 V giving the highest capacitance for this electrode.

The appreciable resistance of the PPCB-cp electrode and dramatic increase in R_{CT} with decreasing potential are indicative of a low quality polymer. Therefore, we tested a pulsed regime (short periods of polymerization with intervals at an offset of 0 V; see section 2.2 for details) to explore whether this alteration in the polymerization condition may result in production of a higher quality polypyrrole.

Figure 2-17 displays typical CVs for a PPCB-pp electrode. The PPCB-pp electrode shares similar voltammetric features with PPCB-cp, except for some shift in peak potentials of the both cathodic and anodic waves. That is, at 40 mV s^{-1} , the cathodic and anodic peaks for the PPCB-pp electrode appeared at *ca.* -0.3 and +0.28 V, respectively. This corresponds to a peak separation of about 0.58 V compared to about 0.32 V observed for the PPCB-cp electrode (figure 2-14). This could originate from slower kinetics of the redox reactions for the PPCB-pp, and/or in part due to its lower electronic/ionic conductivity. Hence impedance spectroscopy was invoked to further explore this.

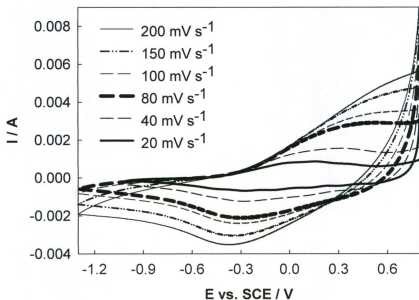


Figure 2-17. Typical cyclic voltammograms of a PPCB-pp electrode recorded at various potential sweep rates in 0.5 M NaClO₄.

Figure 2-18 presents Nyquist and capacitance (inset) profiles for a PPCB-pp electrode. Similar to PPCB-cp, the Nyquist plots for PPCB-pp display RC loops at high frequencies followed by Warburg-type lines in the midrange frequencies, and capacitive behaviour at low frequencies. The potential dependence of PPCB-pp was also similar to that of PPCB-cp, although relatively more resistance can be observed in the Nyquist plots of PPCB-pp. As an instance, the lowest frequency real impedance (*i.e.* at 10 mHz) for the PPCB-cp was 3050 Ω , while that for the PPCB-pp was 4008 Ω . The quantitative

differences between the Nyquist plots in figures 2-15 and 2-18 can reasonably account for the larger peak separation in the CVs of the PPCB-pp.

Capacitance profiles of the PPCB-pp film are also shown in figure 2-18 (inset). As for PPCB-cp, the maximum capacitance for PPCB-pp was obtained at -0.1 V. However, it is notable that the capacitance at -0.3 V for PPCB-pp shows a very large resistance, which consists of an R_{CT} overlapping a Warburg-type resistance.

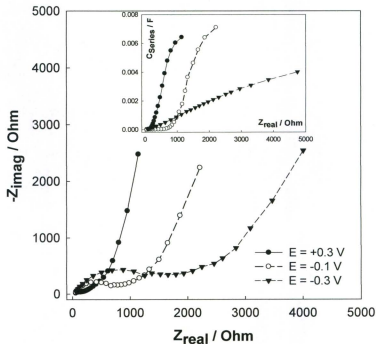


Figure 2-18. Complex-plane plots for a PPCB-pp electrode in 0.5 M NaClO_4 at various dc-offset potentials; capacitance profiles (inset).

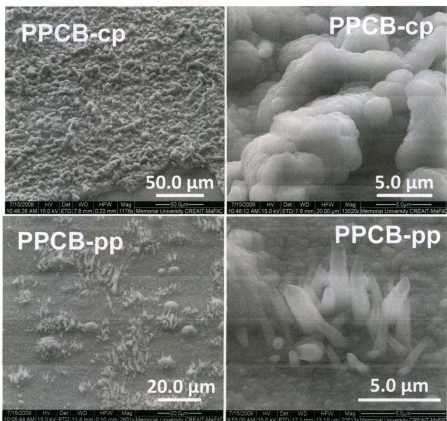


Figure 2-19. Scanning electron micrographs for the PPCB-cp and PPCB-pp composite films.

To obtain morphologic information about the two potentiodynamically prepared PPCB films, representative SEM images for the PPCB-cp and PPCB-pp electrodes are shown in figure 2-19. It is remarkable how a slight modification (*i.e.* pulsed versus continuous polymerization) in the polymerization condition could have resulted in such

significant changes in the structure. The interesting surface structure of the PPCB-cp appears to evenly consist of large sized twisted plates (diameter $\sim 5 - 10 \mu\text{m}$) forming a very rough morphology, into which the CB particles could have been embedded (*i.e.* no evidence for the presence of pure CB can be found). In contrast, the SEM images for the PPCB-pp film display a somewhat homogeneous background covered with spheres of about $0.5 \mu\text{m}$, onto which randomly distributed islands consisting of somewhat tubular buildups can be noticed. These images clearly indicate production of uneven structures using the pulsed potential polymerization, although they may not provide conclusive information attributable to the poor electrochemical performance of the PPCB-pp electrode.

2.3.3. Galvanostatic polymerization

Even though we were able to monitor/characterize the PPCB films prepared using either of the potential-controlled (*i.e.* potentiodynamic and potentiostatic) polymerization methods (see sections 2.3.1 and 2.3.2) to meet one of the important scopes of this study, unfortunately, it was found that these two fashions led to formation of uncontrolled structures and resistive composites. Although the impedance data for the PPCB-cv electrodes show good capacitive behaviour and quite low resistances for the layers with high polypyrrole loadings, the SEM images and polymerization CVs clearly show that a large amount of polypyrrole was deposited at the CB layer|solution interface. As well, undesirable electrochemical properties of the potentiostatically prepared PPCB films

would not justify further study of this method. Therefore, we used a constant current (galvanostatic) regime as the third possible electrochemical method of polymerization.

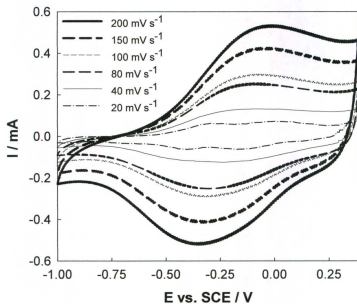


Figure 2-20. Cyclic voltammograms of a PPCB-cc2 electrode in 0.5 M NaClO₄.

Typical CVs for a selected galvanostatically prepared PPCB composite with a polymerization charge of 0.48 C cm⁻² (see experimental section for the polymerization conditions), PPCB-cc2, are shown in figure 2-20. These voltammograms are significantly different from those for the PPCB-cv electrodes shown in figure 2-5. They exhibit only a single redox process, which can be attributed to anion expulsion/insertion. Similar to the CVs for PPCB-cp and PPCB-pp electrodes, the cathodic sweep consists of a single

reduction peak. This suggests that anion expulsion for this electrode (PPCB-cc2), and for both of the potentiostatically prepared electrodes, was more facile than for the PPCB-cv electrodes.

In a meaningful contrast to all of the PPCB films prepared in potential-controlled regimes, peak potentials in the CVs for PPCB-cc2 show a very negligible dependence on scan rate, which can be attributed to faster kinetics/charge transport of the PPCB-cc2 film. Further evidence for the superiority of the PPCB-cc2 to both the PPCB-cv8 and PPCB-cp (and PPCB-pp as well) can be obtained by comparing their corresponding redox peak separations. Herein, one may estimate a peak separation of about 0.3 V (at 200 mV s⁻¹) for the PPCB-cc2 electrode, which is dramatically lower than that for PPCB-cv8 (~ 0.7 V) and PPCB-cp (> 0.9 V). Moreover, the onset potential for the re-oxidation of PPy to its conducting state (compare anodic sweeps in figures 2-5, 2-14, and 2-17) for PPCB-cc2 was at ~ -0.7 V, compared to -0.65 and -0.45 for the potentiodynamic and potentiostatic counterparts, respectively. This suggests that the galvanostatically prepared PPy must become conductive at a lower potential than the other PPCB composites. Exploration of this effect can best be made using impedance spectroscopy, as follows.

Figure 2-21 displays Nyquist profiles for the PPCB-cc2 electrode at various de-offset potentials. Even though it is uncertain to judge whether there was a charge transfer resistance at high frequencies, a resistance-type feature attributable to a RC loop (paralleled R_{CT} and C_{DL}) at -0.5 V can be seen over this region, which became less pronounced at higher potentials. The overlap of this feature with the effects of the geometric capacitance prevents unambiguous identification and quantification.

Consequently, it was problematic to fit the high frequency impedance of the PPCB-cc2 electrode. The quantification results for the Nyquist plots shown in figure 2-21 are listed in Table 2-3 (also see appendix, figures A-11 to A-14, for the complete fitting results compared with the experimental data).

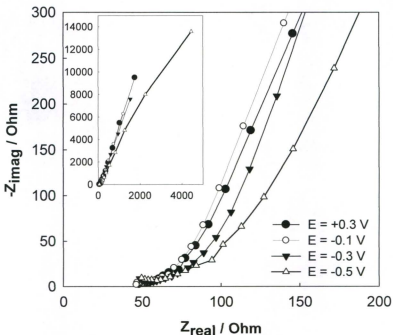


Figure 2-21. Complex-plane (Nyquist) profiles for the PPCB-cc2 electrode at +0.3, -0.1, -0.3, -0.5 V.

It is clear that R_{CT} values remained much smaller than those seen for the PPCB-cv and PPCB-cp electrodes at the same potentials (Tables 2-1 and 2-2), and surprisingly its

value did not significantly change with potential. The midrange frequency resistance, demonstrating the resistance of the PPCB layer (R_L ; Warburg-like region in figure 2-21) increased somewhat with decreasing potential, but the effect was much smaller than observed for the PPCB-cv and PPCB-cp electrodes (see Tables 2-1 and 2-2). This suggests that R_L is essentially dominated by the ionic resistance for the PPCB-cc2 electrode (at least at +0.3 and -0.1 V), in contrast to which the Warburg-type region of for PPCB-cv and PPCB-cp is controlled by the electronic resistance.

Table 2-3. Parameters from impedance data for a PPCB-cc2 electrode.

| $Q / C \text{ cm}^{-2}$ | E / V | R_S / Ω | | R_{CT} / Ω | | $C_{DL} / \mu F$ | R_L / Ω | | C_L / mF | |
|-------------------------|---------|----------------|-----|-------------------|------|------------------|----------------|-----|-------------------|------|
| | | RC | fit | RC | fit | | 45° | fit | -1/ $\omega Z''$ | fit |
| 0.48 | -0.5 | 42 | 39 | — | 13.5 | 0.9 | 240 | 182 | 1.1 | 0.09 |
| 0.48 | -0.3 | 42 | 39 | — | 13 | 2.3 | 174 | 117 | 2.1 | 0.12 |
| 0.48 | -0.1 | 42 | 39 | — | 9.5 | 13.2 | 108 | 91 | 2.5 | 0.13 |
| 0.48 | +0.3 | 42 | 39 | — | 9.4 | 13.2 | 72 | 86 | 1.7 | 0.1 |

— Could not be determined.

R_S : uncompensated solution resistance

R_{CT} : charge transfer resistance

C_{DL} : double layer capacitance

R_L : layer resistance

C_L : layer capacitance

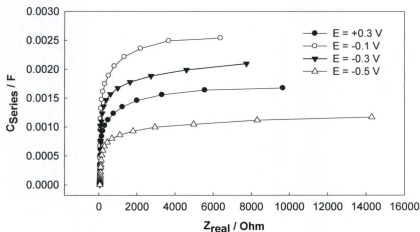


Figure 2-22. Series capacitance as a function of real impedance for the PPCB-cc2 electrode at +0.3, -0.1, -0.3, -0.5 V.

The low-frequency capacitance is related to the charge storage in the polymer and can be seen as an equilibrium insertion capacitance. The capacitive behaviour of the PPCB-cc2 at the various potentials is best visualized using the capacitance profiles, figure 2-22. According to the data in 2-22, the capacitance of the polymer increased to a peak at *ca.* -0.1 V and then decreased at higher potentials (+0.3 V). This is approximately consistent with the location of the peak seen in cyclic voltammetry (figure 2-20). Furthermore, indicative of the system resistance and in line with the Nyquist profiles, the low real impedance region for all the capacitance plots at all potentials displays insignificant resistances (*i.e.* R_{CT}). This is opposite to potentiodynamic polymerization

which led to poor control of the electrode structure and large resistances, and to potentiostatic polymerization which resulted in highly resistive electrodes.

Figure 2-23 pictures selective SEM images for the PPCB-cc2 electrode. Taking 0.48 mC cm^{-2} as the polymerization charge for this electrode, and assuming 2.25 as the number of electrons per unit of pyrrole, one may work out $\sim 1.8 \times 10^{-7} \text{ mol}$ for the polymerized pyrrole. This further corresponds to a mass of *ca.* $1.3 \times 10^{-4} \text{ mg}$ (pyrrole = 67.09 g mol^{-1}), which would form a layer with a thickness of about $2 \text{ }\mu\text{m}$ on a 0.71 cm^2 GC electrode (density of pyrrole $\sim 0.96 \text{ g cm}^{-3}$). This amount of polypyrrole could be reasonably accommodated within the pores of the *ca.* $4 \text{ }\mu\text{m}$ CB layer.

Nevertheless, the morphology of the film is significantly different from those prepared under either of the potential-controlled methods. Here, the PPCB layer has a similar appearance as the blank CB layer (with no polypyrrole; figure 2-4), and the structure appears quite even with particle sizes of less than $0.5 \text{ }\mu\text{m}$. The dense particles for the PPCB-cc2 layer may account for its insignificant R_{CT} value, while homogeneous deposition of pyrrole all over the CB (structure A) could have resulted in the significantly low midrange frequency impedance associated with the layer resistance (Warburg-type line resistance; R_L).

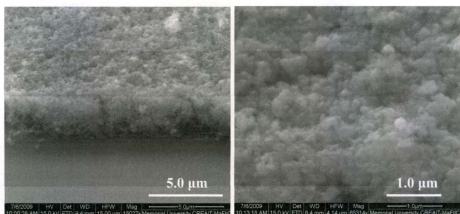


Figure 2-23. Representative SEM images for a PPCB-cc2.

It appears that 0.48 C cm^{-2} was, accidentally, close to the optimum charge for the galvanostatic polymerization of pyrrole on the CB layer. In fact, this charge was adopted from a previous report³⁴ demonstrating the polymerization of pyrrole on a Pt surface, and the PPCB-cc2 was the first galvanostatically prepared electrode in this study. Therefore, we conducted the galvanostatic polymerization using two other charge values, to fabricate one PPCB-cc layer with a lower polypyrrole loading (PPCB-cc1) and one with a higher loading (PPCB-cc3) (see section 2.2 for details).

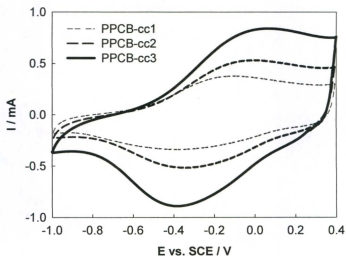


Figure 2-24. Cyclic voltammograms in 0.5 M NaClO₄ at 200 mV s⁻¹ for the PPCB-cc1, PPCB-cc2, and PPCB-cc3 electrodes.

Cyclic voltammograms for the three types of PPCB-cc layer are shown in figure 2-24. Interestingly, PPCB-cc1 and PPCB-cc3 both display the same voltammetric features as described for the PPCB-cc2, except for their different charge accumulation, as expected. By integrating the anodic waves between -0.6 and +0.4 V for these plots, *ca.* 2.9, 2.0, and 1.4 mC charge values (corrected for the CB background) were estimated for the PPCB-cc1, PPCB-cc2, and PPCB-cc3 films, respectively. Taking into account the polymerization charges (see section 2.2; experimental section), and considering 0.23 and 2.23 as number of electrons involved per unit of pyrrole in the doping (oxidation wave; anodic sweep) and the polymerization processes,³⁴ respectively, a polymerization

efficiency (*i.e.* the estimated doping charge in the CVs over the consumed polymerization charge) of about 50-60% can be obtained for the PPCB-cc layers.

SEM images for the PPCB-cc1 and PPCB-cc3 electrodes are displayed in figure 2-25 to reveal the effect of the polymerization charge on structure. While the PPCB-cc1 layer displays lower thickness ($\sim 2 \mu\text{m}$) than the PPCB-cc2 with a somewhat similar structure, the highest loading electrode (PPCB-cc3), with nearly twice as much polypyrrole, shows a much different morphology (figure 2-21B) from PPCB-cc2. In PPCB-cc3, the CB appears to have become embedded within a dense polypyrrole layer, as also seen in figure 2-13 for the PPCB-cv6 electrode.

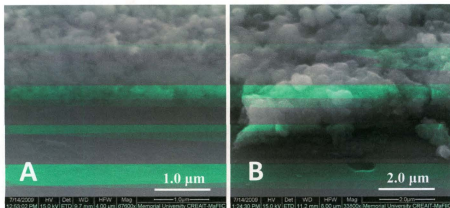


Figure 2-25. SEM images for the PPCB-cc1 and PPCB-cc3 electrodes.

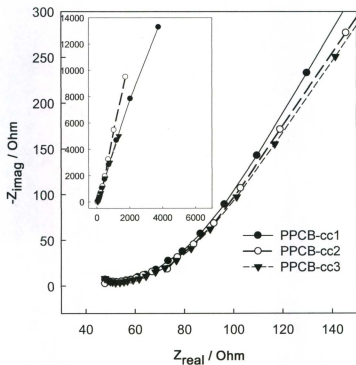


Figure 2-26. Complex-plane diagrams in 0.5 M NaClO₄ at +0.3 V for the PPCB-cc1, PPCB-cc2, and PPCB-cc3 electrodes.

Figure 2-26 shows impedance data at $E = +0.3$ V for the PPCB-cc1, PPCB-cc2, and PPCB-cc3 electrodes. None of the Nyquist plots exhibit significant charge transfer features in their high frequency regions, in a distinct contrast to the Nyquist plots for PPCB-cv, PPCB-cp and PPCB-pp layers. Apart from the RC region, the other observations are similar to those for the PPCB-cv electrodes. The surprisingly

insignificant high frequency resistance for the PPCB-cc electrodes at all loadings suggest that the use of a low constant current for the polymerization resulted in more even coverage of the CB surface area, since R_{CT} should be inversely proportional to the surface area over which the polypyrrole was deposited. The fact that the C_{DL} values measured for the PPCB-cv layers are much lower than the total capacitance of the CB does indicate that there was limited coverage of the CB for those electrodes. However, it is not possible to measure C_{DL} values for the PPCB-cc electrodes to determine whether they are in fact higher, as implied by the absence of charge transfer features. The similarity of the three Nyquist plots in figure 2-26 is remarkable given the different amounts of polymer that were deposited.

Inspection of the intermediate frequency impedance of the three PPCB-cc layers provides interesting structural information. That is, the length of the Warburg region did not change with loading (or charge), indicating the formation of relatively uniform PPCB layers (Structure A), rather than separate CB and polypyrrole layers (Structure B). R_L values of 76, 86 and 77 Ω for PPCV-cc1, PPCV-cc2 and PPCV-cc3, respectively, were obtained by fitting a simplified version of the circuit shown in figure 2-9, without the R_{CT} - C_{DL} element. This confirms the independence of R_L on the polypyrrole loading. The fact that R_L did not change significantly with polypyrrole loading for the PPCB-cc electrodes suggests that it is associated with the ionic (and not electronic) resistance within the pores of the PPCB structure. It is also notable that these R_L values are all significantly lower than those reported in Tables 2-1 and 2-2 for the PPCB-cv and PPCB-cp layers, even though these PPCB-cc electrodes all had lower polypyrrole loadings.

Moreover, the fact that R_t for the PPCB-cv layers decreases clearly indicates the difference in the polymerization pathway (*i.e.* structural evolution) for different polymerization regimes.

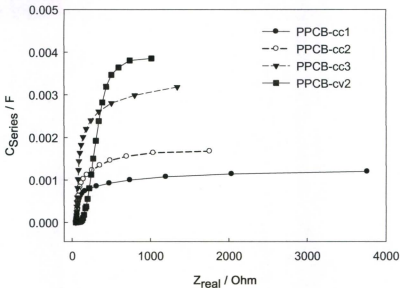


Figure 2-27. Capacitance plots for the PPCB-cc1, PPCB-cc2, PPCB-cc3, and PPCB-cv2 electrodes at +0.3 V.

Figure 2-27 illustrates the C_{series} against real impedance for PPCB-cc1, PPCB-cc2, PPCB-cc3 at +0.3 V to better visualize the low frequency impedance of the PPCB-cc electrodes. As well, data for the PPCB-cv2 electrode, which had a polypyrrole loading closest to those for the PPCV-cc electrodes (note the similar limiting capacitances for

PPCB-cv2 and PPCB-cc3) is also included for comparison. The plots for the PPCB-cc films reveal a regular trend of increasing capacitance with polymerization time. Their steep profiles at the initial stages (*i.e.* low real impedance) indicate that the PPCB-cc layers had high conductivities. This also reflects the absence of significant charge transfer resistances and the low R_L values for these layers relative to PPCB-cv2. These comparative plots for the three loadings of PPCB-cc and the PPCB-cv2 clearly indicated that the constant current method is superior for preparing electrodes with low polypyrrole loadings. However, comparison of the results with those for PPCB-cv6 suggests that the CV method may be better for high loadings (note the much lower resistances at the highest capacitances). The potentiostatic polymerization may also be suitable for preparing high loading PPy films for use in the electrochemical devices provided that the operation potential lies within the range where the film is acceptably conductive (*i.e.* $E > 0.3$ V vs. SCE). Nevertheless, possible oxidative degradation of PPy at high potentials, in concert with the high resistance of the potentiostatically prepared PPy, makes this method an inappropriate regime for the polymerization of pyrrole.

2.4. Concluding remarks

This work demonstrates the electrochemical polymerization of pyrrole on high surface area carbon black (CB) electrodes. Potentiodynamically, potentiostatically, and galvanostatically prepared polypyrrole-CB composites (PPCB) were probed using SEM, cyclic voltammetry and electrochemical impedance spectroscopy. In fact, using SEM as visual proof, we intended not only to characterize the differently made PPCB films, but

also to investigate whether it was possible to unveil structural information by impedance spectroscopy as a powerful technique in this respect. It is noteworthy that in a follow-up work done by Goswami *et al.*,⁷⁴ impedance spectroscopy was successfully employed to measure ionic/electronic properties of Au/polypyrrole composite films to obtain the optimized conductivity.

Herein, it was found that constant current and potentiodynamic, and potentiostatic polymerization methods yielded PPCB composites with different structures. In the potentiodynamic method, the initial steps involved deposition of PPy all over the CB layer, while a mixture of the structures A and B was formed at the final stages of the 8-cycle polymerization. The PPCB composites prepared using potentiostatic methods (*i.e.* continuous and pulsed) displayed large particle size structures with somewhat homogeneous morphologies, with the pulsed regime showing additional top layer tubular islands as well. However, slow polymerization of the polypyrrole at a constant rate (galvanostatic) allows the individual carbon particles to be coated with a thin layer of polypyrrole (Structure A). These PPCB-cc composites show rapid electrochemistry characterized by negligible charge transfer resistances, and high electronic and ionic conductivities. The conductivities of the electrodes are limited by the conductivity of the electrolyte within the pores of the PPCB layer. Consequently, their resistances do not depend on the polypyrrole loading (over the range investigated). This is a particularly important finding regarding the use of such electrodes in supercapacitors and fuel cells.

It was originally thought that use of a potentiodynamic method, in which the polymerization occurred only during certain periods of each cycle, would facilitate

polymerization within the CB layer. There would be time for pyrrole consumed during the polymerization phase to be replenished by diffusion during the undoping-doping phase. Indeed, voltammograms obtained during the polymerization, and SEMs, supported the hypothesis that pyrrole depletion would lead to subsequent polymerization on the outer surface of the CB layer (Structure B). However, the large overpotentials required to initiate polypyrrole deposition caused loss of control over the polymerization rate and consequently the location of the polymerization. The rapid deposition of polypyrrole led to electrodes with incomplete coating of the CB particles. As well, the potentiostatic polymerization similarly gave a high resistance polymer, and the attempt to use a pulsed potentiostatic regime resulted in an even more resistive PPCB. In contrast, charge transfer and electronic resistances for electrodes prepared by slow deposition at constant current (PPCB-cc) were markedly lower, and their values changed only slightly with potential. Interestingly, similar to the potentiostatic polymerization case, adoption of a pulsed regime in the galvanostatic polymerization gave rise to a somewhat more resistive polymer film.

This study demonstrates the complexity of the electrochemical polymerization of polypyrrole on porous carbon electrodes and the power of impedance spectroscopy for probing the electrochemical characteristics of the resulting composites. Further work will be aimed at developing a full understanding of how to control deposition conditions for the creation of desired structures and to optimize the performances of these structures.

References

1. H. S. Nalwa, *Handbook of Organic Conductive Molecules and Polymers*, Wiley, Chichester, UK, pp. 2-4, 1997.
2. T. A. Skotheim, R. L. Elsenbaumer and J. R. Reynolds, *Handbook of Conducting Polymers*, 2nd edn, Marcel Dekker, New York, 1998.
3. H. Shirakawa, A. McDiarmid and A. Heeger, *Chem. Commun.*, 2003, 1.
4. A. Malinauskas, J. Malinauskiene and A. Ramanavicius, *Nanotechnology*, 2005, **16**, R51.
5. C. Li, H. Bai and G. Q. Shi, *Chem. Soc. Rev.*, 2009, **38**, 2397-2409.
6. E. Antolini and E. R. Gonzalez, *Appl. Catal., A*, 2009, **365**, 1-19.
7. D. Curran, J. Grimshaw and S. D. Perera, *Chem. Soc. Rev.*, 1991, **20**, 391-404.
8. F. Chen and P. Liu, *Chem. Eng. J.*, 2011, **168**, 964-971.
9. R. H. Friend, R. W. Gymer, A. B. Holmes, J. H. Burroughes, R. N. Marks, C. Taliani, D. D. C. Bradley, D. A. Dos Santos, J. L. Bredas, M. Logdlund and W. R. Salaneck, *Nature*, 1999, **397**, 121-128.
10. S. Gunes, H. Neugebauer and N. S. Sariciftci, *Chem. Rev.*, 2007, **107**, 1324-1338.
11. G. Sonmez, *Chem. Commun.*, 2005, 5251.
12. L. Groenendaal, F. Jonas, D. Freitag, H. Pielartzik and J. R. Reynolds, *Adv. Mater.*, 2000, **12**, 481-494.
13. W. A. Wampler, C. Wei and K. Rajeshwar, *Chem. Mat.*, 1995, **7**, 585-592.
14. B. Coffey, P. V. Madsen, T. O. Poehler and P. C. Searson, *J. Electrochem. Soc.*, 1995, **142**, 321-325.

15. S. Higashika, K. Kimura, Y. Matsuo and Y. Sugie, *Carbon*, 1999, **37**, 354-356.
16. B. Ballarin, C. Zanardi, L. Schenetti, R. Seeber and J. de Cisneros, *Synth. Met.*, 2003, **139**, 29-33.
17. G. Wu, L. Li, J. H. Li and B. Q. Xu, *Carbon*, 2005, **43**, 2579-2587.
18. Y. S. Choi, S. H. Joo, S. A. Lee, D. J. You, H. Kim, C. Pak, H. Chang and D. Seung, *Macromolecules*, 2006, **39**, 3275-3282.
19. K. S. Ryu, Y. G. Lee, K. M. Kim, Y. J. Park, Y. S. Hong, X. L. Wu, M. G. Kang, N. G. Park, R. Y. Song and J. M. Ko, *Synth. Met.*, 2005, **153**, 89-92.
20. V. Gupta and N. Miura, *J. Power Sources*, 2006, **157**, 616-620.
21. Y. H. Lin and X. L. Cui, *J. Mater. Chem.*, 2006, **16**, 585-592.
22. H. Tamai, M. Hakoda, T. Shiono and H. Yasuda, *J. Mater. Sci.*, 2007, **42**, 1293-1298.
23. A. L. M. Reddy, N. Rajalakshmi and S. Ramaprabhu, *Carbon*, 2008, **46**, 2-11.
24. W. J. Feast, J. Tsibouklis, K. L. Pouwer, L. Groenendaal and E. W. Meijer, *Polymer*, 1996, **37**, 5017-5047.
25. F. T. A. Vork, L. J. J. Janssen and E. Barendrecht, *Electrochim. Acta*, 1987, **32**, 1187-1190.
26. L.-X. Wang, X.-G. Li and Y.-L. Yang, *React. Funct. Polym.*, 2001, **47**, 125-139.
27. L. F. Warren and D. P. Anderson, *J. Electrochem. Soc.*, 1987, **134**, 101-105.
28. G. Inzelt, *Electroanalysis*, 1995, **7**, 895-903.
29. M. M. Musiani, *Electrochim. Acta*, 1990, **35**, 1665-1670.

30. A. Rudge, I. Raistrick, S. Gottesfeld and J. P. Ferraris, *Electrochim. Acta*, 1994, **39**, 273-287.
31. J. Tanguy, N. Mermilliod and M. Hoclet, *J. Electrochem. Soc.*, 1987, **134**, 795-802.
32. G. Garcia-Belmonte and J. Bisquert, *Electrochim. Acta*, 2002, **47**, 4263-4272.
33. X. M. Ren and P. G. Pickup, *Electrochim. Acta*, 2001, **46**, 4177-4183.
34. X. M. Ren and P. G. Pickup, *J. Phys. Chem.*, 1993, **97**, 5356-5362.
35. X. M. Ren and P. G. Pickup, *Electrochim. Acta*, 1996, **41**, 1877-1882.
36. X. M. Ren and P. G. Pickup, *J. Electroanal. Chem.*, 1997, **420**, 251-257.
37. C. Deslouis, T. ElMoustafid, M. M. Musiani and B. Tribollet, *Electrochim. Acta*, 1996, **41**, 1343-1349.
38. A. Hallik, A. Alumaa, J. Tamm, V. Sammelselg, M. Vaartnou, A. Janes and E. Lust, *Synth. Met.*, 2006, **156**, 488-494.
39. M. Kalaji and L. M. Peter, *J. Chem. Soc.-Faraday Trans.*, 1991, **87**, 853-860.
40. I. Rubinstein, E. Sabatani and J. Rishpon, *J. Electrochem. Soc.*, 1987, **134**, 3078-3083.
41. J. Tanguy, J. L. Baudoin, F. Chao and M. Costa, *Electrochim. Acta*, 1992, **37**, 1417-1428.
42. W. J. Albery, C. M. Elliott and A. R. Mount, *J. Electroanal. Chem.*, 1990, **288**, 15-34.
43. T. Amemiya, K. Hashimoto and A. Fujishima, *J. Phys. Chem.*, 1993, **97**, 4187-4191.

44. R. P. Buck, M. B. Madaras and R. Mackel, *J. Electroanal. Chem.*, 1993, **362**, 33-46.
45. R. P. Buck, M. B. Madaras and R. Mackel, *J. Electroanal. Chem.*, 1994, **366**, 55-68.
46. C. Deslouis, M. M. Musiani and B. Tribollet, *J. Electroanal. Chem.*, 1989, **264**, 57-76.
47. C. Deslouis, M. M. Musiani and B. Tribollet, *J. Phys. Chem.*, 1994, **98**, 2936-2940.
48. G. Lang and G. Inzelt, *Electrochim. Acta*, 1991, **36**, 847-854.
49. R. M. Penner and C. R. Martin, *J. Phys. Chem.*, 1989, **93**, 984-989.
50. A. M. Waller, A. N. S. Hampton and R. G. Compton, *J. Chem. Soc.-Faraday Trans.*, 1989, **85**, 773-781.
51. W. J. Albery and A. R. Mount, *J. Chem. Soc.-Faraday Trans.*, 1994, **90**, 1115-1119.
52. G. Inzelt and G. Lang, *J. Electroanal. Chem.*, 1994, **378**, 39-49.
53. R. P. Buck, *J. Electroanal. Chem.*, 1986, **210**, 1-19.
54. C. Ehrenbeck, K. Juttner, S. Ludwig and G. Paasch, *Electrochim. Acta*, 1998, **43**, 2781-2789.
55. G. Lang, J. Bacskai and G. Inzelt, *Electrochim. Acta*, 1993, **38**, 773-780.
56. G. Paasch, *Electrochim. Acta*, 2002, **47**, 2049-2053.
57. G. Paasch, K. Micka and P. Gersdorf, *Electrochim. Acta*, 1993, **38**, 2653-2662.

58. M. A. Vorotyntsev, J. P. Badiali and G. Inzelt, *J. Electroanal. Chem.*, 1999, **472**, 7-19.
59. M. A. Vorotyntsev, L. I. Daikhin and M. D. Levi, *J. Electroanal. Chem.*, 1994, **364**, 37-49.
60. M. D. Levi, Y. Gofer and D. Aurbach, *Russ. J. Electrochem.*, 2004, **40**, 273-279.
61. M. A. Vorotyntsev, *Electrochim. Acta*, 2002, **47**, 2071-2079.
62. M. R. Warren and J. D. Madden, *J. Electroanal. Chem.*, 2006, **590**, 76-81.
63. M. Hughes, G. Z. Chen, M. S. P. Shaffer, D. J. Fray and A. H. Windle, *Chem. Mat.*, 2002, **14**, 1610-1613.
64. J. H. Park, J. M. Ko, O. O. Park and D. W. Kim, *J. Power Sources*, 2002, **105**, 20-25.
65. Q. F. Xiao and X. Zhou, *Electrochim. Acta*, 2003, **48**, 575-580.
66. V. Branzoi, L. Pilan and F. Branzoi, *Electroanalysis*, 2009, **21**, 557-562.
67. A. Izadi-Najafabadi, D. T. H. Tan and J. D. Madden, *Synth. Met.*, 2005, **152**, 129-132.
68. H. Talbi, P. E. Just and L. H. Dao, *J. Appl. Electrochem.*, 2003, **33**, 465-473.
69. J. Wang, Y. L. Xu, X. Chen and X. F. Sun, *Compos. Sci. Technol.*, 2007, **67**, 2981-2985.
70. S. Bhandari, M. Deepa, A. K. Srivastava, C. Lal and R. Kant, *Macromol. Rapid Commun.*, 2008, **29**, 1959-1964.
71. C. Dalmolin, S. R. Biaggio, R. C. Rocha and N. Bocchi, *J. Solid State Electrochem.*, 2007, **11**, 609-618.

72. P. Pieta, E. Grodzka, K. Winkler, M. Warczak, A. Sadkowski, G. Z. Zukowska, G. M. Venukadasula, F. D'Souza and W. Kutner, *J. Phys. Chem. B*, 2009, **113**, 6682-6691.
73. X. M. Ren and P. G. Pickup, *J. Electroanal. Chem.*, 1995, **396**, 359-364.
74. L. Goswami, N. S. Sarma and D. Chowdhury, *J. Phys. Chem. C*, 2011, **115**, 19668-19675.

Chapter 3

Electrocatalytic oxidation of formic acid at Pd nanoparticles incorporated into polyaniline modified carbon fibre paper

Chapter 3. Electrocatalytic oxidation of formic acid at Pd nanoparticles incorporated into polyaniline modified carbon fibre paper

This work has been published in part as *Moghaddam, R.B. and Pickup P.G., Formic acid oxidation at spontaneously deposited palladium on polyaniline-modified carbon fibre paper, Electrochimica Acta, 2011, 56, 7666-7672*. The text was written in part by Dr. Peter Pickup.

3.1. Introduction

A significant amount of research has been increasingly focused on the electrochemical oxidation of formic acid (FA), which is the central reaction in the development of anodes for direct formic acid fuel cells (DFAFCs).¹ In fact, due to a number of superior properties of FA, DFAFCs have become potential alternatives to the most widely applied H₂-fed polymer electrolyte membrane (PEM) and direct methanol fuel cells.²⁻¹⁰ That is, FA is largely safer than H₂ in transportation, less toxic than methanol, and its oxidation gives an appreciable electromotive force.^{1, 3, 6} Moreover, the well-known fuel crossover which is a common source of voltage losses in alcohol fuel cells is less significant in DFAFCs.^{1, 11-13} This will allow use of more concentrated FA solutions to be fed to fuel cell anodes to improve energy and power densities.¹ In this regard, extended reaction zone anodes have also been developed to compensate for the inherent low energy density of DFAFCs.^{8, 14} For example, Pd deposited onto a three dimensional graphite felt electrode was shown to provide higher power densities than a commercial Pd catalyst-coated membrane.⁸ The improved performances of such anodes

with liquid fuels have been attributed to better catalyst utilization, improved fuel mass transport, and decreased CO₂ accumulation.

As a result of their ease of preparation, appreciable stability, and excellent electronic/ionic conductivity, conducting polymers (CPs) have gained a great deal of attention among all the potential catalyst support materials.^{7, 15-17} In a number of studies, as support materials they have shown large effects on the electrochemical characteristics of the resulting catalysts.¹⁸⁻²⁰ In this regard, as a result of its superior physicochemical properties (e.g. stability, conductivity, etc), polyaniline (PANI) has been used most extensively.²¹ The promotional effects of PANI supports have been ascribed to accelerated electronic/ionic transport, homogenous dispersion of catalyst particles on the substrate, and inhibited adsorption of poisoning intermediates (such as -CO and -CHO, formed as a result of incomplete oxidation of small organic molecules).⁷ Having excellent electron conductivity owing to their conjugated structure, CPs such as PANI are also well-known as strong ion transporters. Antolini *et al.*⁷ have comprehensively reviewed research on the effects of CPs on the acceleration of the electron/ion transport rate as well as on homogenous accommodation of catalyst species into the polymeric films. They have also summarized the reports on how conducting polymers can increase accessibility of the fuel to catalyst active sites^{22,23} to increase catalytic efficiency. As noted before, the other important effect of PANI has been repeatedly shown to be inhibition of the poisoning species adsorption on Pt during the oxidation of C1 molecules (CH₃OH, HCHO, HCO₂H, CO).²⁴⁻²⁶ Nevertheless, while possessing considerable promotional effects, Hable *et al.*²¹ showed in an early report that synergetic effects of PANI on

catalytic systems was limited to the potential range in which it was electronically conductive. The oxidation of methanol and ethanol at PtRu and PtSn as well-known catalytic systems were presented to validate the hypothesis. They showed that in order for a typical PANI support to exert promotional effects, it has to be sufficiently conductive over the catalytic potential window. It was shown that the cocatalytic effects of Sn on the Pt were significantly inhibited by PANI when it had low conductivity at low potentials. In contrast, Ru-assisted oxidation of methanol at Pt, which takes place at higher potentials, was not affected by the low-potential resistivity of PANI. More recently, one may find a number of reports on the effects of the method used for deposition of the PANI support^{27, 28} and Pt^{1, 29, 30} catalyst on the catalytic oxidation of methanol at PANI-Pt composites. It has also been demonstrated that the dopant type can greatly influence the activity of Pt in the oxidation of methanol. As such, polymerization in H₂SO₄ results in the formation of a granular PANI structure while HClO₄ and HBF₄ form fibrillar PANI structures; the composites of the granular and fibrillar PANI with Pt gave high and low activities for methanol oxidation, respectively.²⁷ Furthermore, in recent work by us, it was shown that the polymerization medium had a remarkable influence on the catalytic activity of Pd on PANI in FA oxidation with H₂SO₄ giving the highest current density.³¹ However, in addition to the effects of the polymerization medium, Zhou *et al.*²⁸ showed that the polymerization regime greatly influenced both the structure and activity of the PANI supports. Therein, nanofibrillar PANI prepared by a pulse galvanostatic method was shown to provide a more active catalyst than granular PANI prepared galvanostatically.²⁸ It was suggested that the higher conductivity and specific area of the

nanofibrillar PANI were responsible for the enhanced electrocatalytic activity. As well, PANI nanowires doped with trifluoromethanesulfonic acid have recently been used to fabricate a carbon black/PANI composite support for Pt nanoparticles.³² An impedance study of methanol oxidation with this catalyst indicated that the PANI improved ion and methanol transport as well as decreased the susceptibility of the Pt to poisoning.

In a large body of literature, electrochemical impedance spectroscopy (EIS) has been used as a powerful tool to inspect the electronic/ionic characteristics of conducting polymers.³³⁻³⁷ It has been shown for polyaniline,^{12, 35, 38-40} polypyrrole,⁴¹⁻⁴⁴ poly(3,4-ethylenedioxythiophene) (PEDOT)^{41, 45} and polythiophene^{46, 47} as the most commonly studied polymers that the preparation conditions can enormously influence the electrochemical performance of the polymers.

Therefore, it was intended in the present work to investigate whether the electronic/ionic characteristics of polyaniline films fabricated under various electrochemical conditions (potentiodynamic, potentiostatic, and galvanostatic) can affect the activities of their resulting composites with Pd nanoparticles. In fact, we essentially aimed at accounting for possible different activities of the prepared composites towards the oxidation of FA based on the electrochemical characteristics of their corresponding PANI substrates. For this purpose, three types of PANI films were made potentiodynamically, potentiostatically, and galvanostatically. Thereafter, these PANI films were loaded by Pd nanoparticles using two approaches as follows:

1. Spontaneous deposition of Pd on PANI based on reductive deposition of Pd from a solution of PdCl₂ at a CFP/PANI electrode preconditioned at a negative potential

(described in the experimental section in detail); here, we actually adopted the method originally introduced by Eliseeva *et al.* (spontaneous incorporation of Pd nanoparticle in PEDOT)⁴⁸ for our system.

2. Drop coating of the PANI films with an aqueous solution of Pd nanoparticles (synthesis of the Pd nanoparticles is described in the experimental section in detail); this complementary study was performed not only to further assess the trend observed for the composites made by the spontaneous deposition method but also to test whether the drop coating method could give composites with higher activities.

Electrochemical impedance spectroscopy (EIS) has been employed to elucidate the different electronic/ionic and capacitive characteristics of the PANI supports and their possible roles in the FA oxidation activities of the resulting composites.

3.2. Experimental

3.2.1. Chemicals

Sulfuric acid (Fisher Scientific), formic acid (Sigma–Aldrich, ACS reagent grade), palladium(II) chloride (PMO Pty Ltd.), palladium(II) nitrate (Alfa Aesar), sodium borohydride (Sigma Aldrich), sodium citrate (Anachemia), and carbon fibre paper (Toray TGP-H-090) were used as received. Aniline (Sigma Aldrich) was purified by passing through an alumina column prior to use. Doubly distilled water was used throughout the experiments. All measurements were recorded under a nitrogen atmosphere following purging for 15 min.

3.2.2. Electrochemical Instrumentation

An EG&G Model 273A Potentiostat/Galvanostat run by a PC through M270 commercial software was used for voltammetric measurements. In addition, an EG&G Model 5210 Lock-in Amplifier and Power-Suite commercial software were used for electrochemical impedance spectroscopy. Electrochemical impedance measurements were performed over the range of 10 kHz to 1 Hz using a potential amplitude of 10 mV. A saturated calomel electrode (SCE) and a platinum wire formed the reference and counter electrode, respectively.

3.2.3. Working electrode preparation

3.2.3.1. Electropolymerization of aniline

Polyaniline supported carbon fibre paper (CFP; ca. 3 cm × 1 cm with ca. 1 cm² immersed in the electrolyte) electrodes were synthesized galvanostatically (CFP/G-PANI) ($I = 1.4 \times 10^{-4}$ A, $t = 1000$ s), potentiostatically (CFP/P-PANI) ($E = 0.69$ mV, $t = 1000$ s), and potentiodynamically (CFP/PD-PANI) (3 cycles between -0.2 and 1.1 mV at 50 mV s⁻¹).

3.2.3.2. Spontaneous deposition of Pd

Spontaneous deposition of Pd onto the PANI coated CFP electrodes was achieved by first reducing the PANI at $E = -200$ mV for 100 s, followed by exposure to 0.005 M PdCl₂ in 0.1 M H₂SO₄ for 100 s.⁴⁸ Simultaneous oxidation of the PANI and reduction of

Pd(II) results in formation of a Pd-PANI composite, generally designated as CFP/PANI/Pd_{SP}.

3.2.3.3. Drop coating of PANI films with Pd nanoparticle (Pd NP) solution

A Pd nanoparticle solution was prepared by adding NaBH₄(aq) (1.5 mL, 60 mM) dropwise to a stirred solution of Pd(NO₃)₂(aq) (10 mL, 3 mM) containing 0.6 mL of 50 mM sodium citrate. The mixture was stirred for a further 2 h and then the gray colloidal Pd nanoparticle solution was stored in a fridge. X-ray diffraction measurements indicated that the average particle diameter was 6.4 ± 0.4 nm, and this was confirmed by transmission electron microscopy. About 50 µg of Pd NP (ca. 0.17 mL) was drop coated on each of the three CFP/PANI electrodes to obtain CFP/PD-PANI/Pd_{NP}, CFP/PANI/Pd_{NP}, and CFP/G-PANI/Pd_{NP} electrodes.

3.2.4. Characterization of the working electrodes

Scanning electron microscopy (SEM) was performed with a Model FEI Quanta 400 environmental SEM. To perform transmission electron microscopy (TEM), dark green PANI/Pd_{SP} polymer powder was carefully scraped from the CFP/PANI/Pd_{SP} electrode (using a fine spatula) and dispersed in ethanol with sonication. A drop of the suspension was applied to a 200 mesh copper grid with a carbon support film. The grid was allowed to dry overnight and then observed under a Model JEOL 2011 transmission electron microscope (The Microscopy and Microanalysis Facility, University of New Brunswick). X-ray diffraction measurements on the CFP/PANI/Pd_{SP} electrodes did not show any peaks that could be attributed to Pd, presumably because the loadings of Pd

were below the detection limit. Pd loadings were determined by placing the CFP/PANI/Pd_{SP} electrodes in a concentrated mixture of HCl + HNO₃ to dissolve the Pd (3 days). The concentration of the resulting solution was determined by using a model EALN DRC II inductively coupled plasma mass spectrometer (ICP-MS; Axial Field Technology).

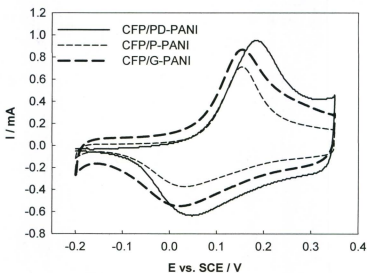


Figure 3-1. Cyclic voltammograms (10 mV s^{-1}) of CFP/PD-PANI, CFP/P-PANI, and CFP/G-PANI electrodes in $0.5 \text{ M H}_2\text{SO}_4$.

3.3. Results and discussion

3.3.1. Characterization of the CPF/PANI

Figure 3-1 presents typical voltammograms of CFP/G-PANI, CFP/P-PANI, and CFP/PD-PANI (10 mV s^{-1}) in $0.5 \text{ M H}_2\text{SO}_4$. In all voltammograms, the forward sweep is dominated by a well-defined anodic peak at about $+0.15 \text{ V}$ following which a broad reduction peak develops in the cathodic sweep centered at about $+0.03 \text{ V}$. The areas under the voltammograms indicate similar quantities of PANI films deposited for each polymerization regime. The most considerable difference in the voltammograms is at potentials below 0 V , where CFP/G-PANI shows significantly higher current than the other two. The feature cannot be reasonably accounted for by the somewhat different PANI loadings for each electrode. In fact, CFP/PD-PANI had the highest PANI loading in the group but produced the lowest current between -0.2 to 0 V .

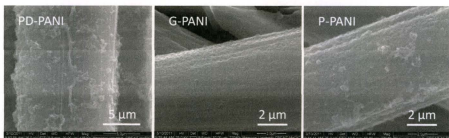


Figure 3-2. SEM images of the CFP/PD-PANI, CFP/G-PANI, and CFP/P-PANI electrodes.

Figure 3-2 displays SEM images of carbon fibres coated with PANI films under potentiodynamic, galvanostatic, and potentiostatic polymerization conditions. Although all three CFP/PANI composites showed fairly similar morphology, it can be observed that CFP/G-PANI displays a smoother surface. This can be ascribed to the formation of more homogenous polymeric assemblies in the slow galvanostatic polymerization, similar to a previous report on the polymerization of polypyrrole (see chapter 2).⁴² Closer inspection of the SEM images reveals that there are dust-type precipitates on each PANI-coated fibre, with CFP/G-PANI visually having less of these features. X-ray analysis (not presented) showed that these dusts were nitrogen-rich and could be mainly composed of assemblies of PANI chains.

3.3.2. Characterization of the CPF/PANI/Pd_{SP} composites

Voltammograms of the CFP/PANI/Pd_{SP} electrodes made with the three types of PANI are shown in figure 3-3. Herein, similar features can be observed by inspection of the voltammograms at potentials between -0.2 and 0.1 V where CFP/G-PANI/Pd_{SP} and CFP/PD-PANI/Pd_{SP} exhibit the largest and smallest background currents. Moreover, all of the three PANI/Pd_{SP} composites displayed qualitatively similar patterns beyond 0.1 V, where the voltammograms are dominated by the electrochemistry of the PANI. This indicates that the spontaneous deposition method employed here preserved the original electrochemical characteristics of the PANI substrates.

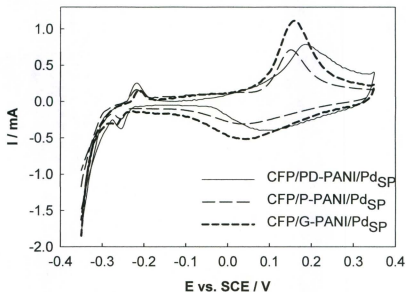


Figure 3-3. Cyclic voltammograms (10 mV s^{-1}) of CFP/PD-PANI/Pd, CFP/P-PANI/Pd, and CFP/G-PANI/Pd electrodes in $0.5 \text{ M H}_2\text{SO}_4$.

Nevertheless, in all the CVs in figure 3-3, hydrogen electrochemistry can be identified by the peaks at ca. -0.27 V (cathodic; H_{ads}) and -0.21 V (anodic; H_{des}). These signals along with the cathodic current spike at potentials below ca. -0.28 V (due to H_2 evolution) confirmed the presence of electroactive Pd species. The significant peak separations between the H adsorption and desorption waves can be either attributed to the electronic resistance of the PANI, which becomes non-conductive when fully reduced, or due to the 3-dimensional structure of carbon fibre paper which may limit ionic diffusion.

We show in section 3.3.4 that a bare carbon fibre paper coated with Pd nanoparticles (no PANI) also shows a significant peak separation. However, it can be inferred from the relative sizes of the H adsorption peaks that the CFP/PD-PANI/Pd_{SP} electrode had a higher electroactive Pd surface area than the other two composites. This was further explored by TEM images of the three CFP/PANI/Pd_{SP} electrodes shown in figure 3-4. Consistent with the CVs, TEMs displayed smaller crystallite sizes for the CFP/PD-PANI/Pd_{SP} electrode (ca. 5 nm) compared to ca. 17 and 25 nm for CFP/G-PANI/Pd_{SP} and CFP/P-PANI/Pd_{SP}, respectively. Moreover, the larger electroactive area for CFP/PD-PANI/Pd_{SP} is also in line with its higher Pd loading (80 μg compared to 70 and 50 μg for CFP/G-PANI/Pd_{SP} and CFP/P-PANI/Pd_{SP}; see section 3.2.4 for details).

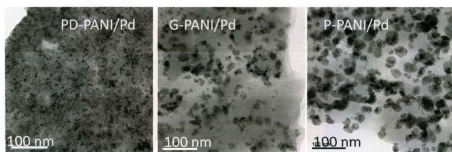


Figure 3-4. TEM images of PANI/Pd_{SP} deposits scraped from CFP/PD-PANI/Pd_{SP}, CFP/G-PANI/Pd_{SP}, and CFP/P-PANI/Pd_{SP} electrodes.

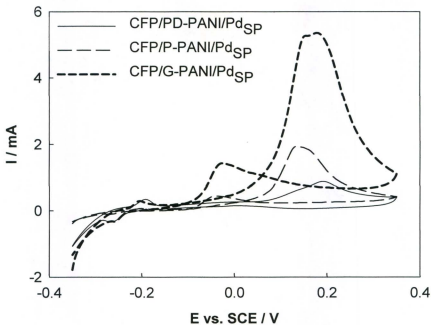


Figure 3-5. Cyclic voltammograms (10 mV s^{-1}) of CFP/PD-PANI/Pd_{SP}, CFP/P-PANI/Pd_{SP}, and CFP/G-PANI/Pd_{SP} electrodes in $0.5 \text{ M H}_2\text{SO}_4$ containing 0.5 M HCOOH .

3.3.3. Formic acid oxidation at CPF/PANI/Pd_{SP} composites

Figure 3-5 presents voltammetric oxidation of 0.5 M formic acid (FA) at CPF/PANI/Pd_{SP} electrodes at a scan rate of 10 mV s^{-1} . It was reasonably expected, based on TEMs and the $H_{\text{ads,des}}$ relative areas, that CFP/PD-PANI/Pd_{SP} would exhibit

significantly better performance than the other two composites. Interestingly, it can be seen that CFP/G-PANI/Pd_{SP} was remarkably superior to both CFP/PD-PANI/Pd_{SP} and CFP/P-PANI/Pd_{SP} merely by comparing the FA oxidation peak centred at about +0.18 V. Coincidental to the electrochemistry of PANI, this large peak provides further evidence for the presence of electroactive Pd particles. As such, CFP/G-PANI/Pd_{SP} gave a peak current of ca. 5.5 mA compared to 2 and 0.9 mA for CFP/P-PANI/Pd_{SP} and CFP/PD-PANI/Pd_{SP}, respectively, compared to peak currents of ca. 0.75 to 0.95 mA for all three electrodes with no Pd or FA, respectively (see figure 3-1).

Constant potential oxidation of FA was also conducted to further investigate the oxidation of FA at the three types of CFP/PANI/Pd composite electrodes. Figure 3-6A-D presents chronoamperometric (CA) profiles of the CFP/G-PANI/Pd_{SP}, CFP/P-PANI/Pd_{SP}, and CFP/PD-PANI/Pd_{SP} electrodes at various potentials ranging from -0.2 to +0.1 V. The range highlighted here covers the useful potential window for operation of the anode of a DFAFC. For all three composites, the current decayed significantly over the 100 s time scale of the experiment, which is typical for FA oxidation at Pd catalysts.¹ Consistent with the voltammograms in figure 3-5, CFP/G-PANI/Pd_{SP} was significantly superior to CFP/PD-PANI/Pd_{SP} while CFP/P-PANI/Pd_{SP} showed intermediate activity at +0.1 V.

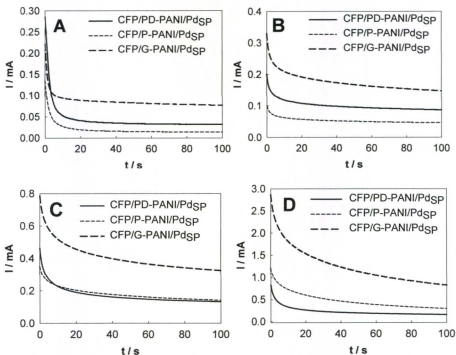


Figure 3-6. Chronoamperometric responses at $E = -0.2$ (A), -0.1 (B), 0 (C), and $+0.1$ (D) V for CFP/PD-PANI/Pd_{SP}, CFP/P-PANI/Pd_{SP}, and CFP/G-PANI/Pd_{SP} electrodes in 0.5 M H₂SO₄ containing 0.5 M FA.

A similar trend to the profiles at $+0.1$ V was seen at 0 V although there was a negligible difference between CFP/PD-PANI/Pd_{SP} with CFP/P-PANI/Pd_{SP}. In contrast, in CAs recorded at -0.1 and -0.2 V, although CFP/G-PANI/Pd_{SP} still gave the highest current, CFP/PD-PANI/Pd_{SP} was superior to CFP/P-PANI/Pd_{SP}. This follows the trend seen in the voltammograms. The higher activity of CFP/PD-PANI/Pd_{SP} relative to

CFP/P-PANI/Pd_{SP} at low potentials could be explained by its higher Pd loading and smaller Pd particle size, both of which should provide a larger Pd active area.

3.3.4. Formic acid oxidation at CFP/PANI/Pd_{NP} composites

Recently in the study of support effects, drop coating of preformed metal nanoparticles has been shown to be a powerful tool in investigating synergetic effects of metal oxides and conducting polymers on the oxidation of organic fuels at Pt and Pd nanoparticles.^{31, 49} Drop coating is advantageous over spontaneous deposition in that the catalyst loading can be reproducibly controlled, simply, by the aid of a fine micropipette. Therefore, we employed this versatile tool to directly inspect the effects of the CFP/PANI supports on the activity of Pd in the oxidation of FA. Figure 3-7A-B shows overlaid voltammograms of the CFP/PD-PANI/Pd_{NP}, CFP/P-PANI/Pd_{NP}, and CFP/G-PANI/Pd_{NP} electrodes in the absence and presence of 0.5 M FA. Consistent with figure 3-1, the background current for CFP/G-PANI/Pd_{NP} was the largest whereas CFP/PD-PANI/Pd_{NP} displayed the smallest. Peaks assigned to underpotential hydrogen deposition (cathodic sweep; ~ -0.25 V) and stripping (anodic sweep; ~ -0.23 V) together with the current spike due to the hydrogen evolution reaction (HER; below -0.3 V) are indicative of the presence of electroactive Pd species. The hydrogen signals for all three composites should correspond to similar quantities of active Pd. However, close inspection of the H_{ads} and H_{des} peaks reveals that there was a more significant peak separation for CFP/G-PANI/Pd_{NP} (similar to that in the CFP/PANI/Pd_{SP} electrodes), probably due to its larger ionic/electronic resistance. It is shown in section 3.4 that unlike CFP/PD-PANI and

CFP/P-PANI, impedance of CFP/G-PANI gave a significant Warburg-type impedance at intermediate frequencies. This is characteristic of a porous electrode and is due to the combined ionic and electronic resistance.⁵⁰ Detailed discussion of the impedance data is presented in section 3.3.5.

Nevertheless, voltammograms for the oxidation of FA at CFP/PANI/Pd_{NP} composites (figure 3-7B) displayed quite different observations from their CFP/PANI/Pd_{SP} counterparts (figure 3-5). The main differences are the much higher currents at the CFP/PANI/Pd_{NP} electrodes and the approximately linear current increases relative to the peaked responses in figure 3-5.

The currents at the CFP/PANI/Pd_{NP} electrodes did not peak or reach limiting values before the selected anodic limit (+0.35 V). The upper limit was set at +0.35 V to avoid oxidative degradation (overoxidation) of the PANI films while covering the useful potential window for operation of the anode of a DFAFC. In contrast, for the CFP/PANI/Pd_{SP} electrodes FA oxidation started at ca. -0.1 V followed by a sharp surge up to about +0.18 V after which current decreased rapidly (see figure 3-5).

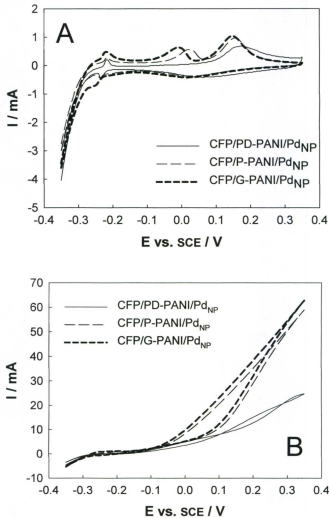


Figure 3-7. Cyclic voltammograms (10 mV s^{-1}) of CFP/PD-PANI/Pd_{NP}, CFP/P-PANI/Pd_{NP}, and CFP/G-PANI/Pd_{NP} electrodes in $0.5 \text{ M H}_2\text{SO}_4$ and in the absence (A) and presence (B) of 0.5 M FFA .

For better visualization of the difference between the two series of composites, figure 3-8 illustrates comparative CVs of the CFP/G-PANI/Pd_{SP} and CFP/G-PANI/Pd_{NP} electrode in the presence of FA over an extended anodic window (up to +1 V). In these voltammograms, the peak current value for CFP/G-PANI/Pd_{NP} was ca. 65 μ A compared to ca. 5.5 μ A for CFP/G-PANI/Pd_{SP}. Furthermore, CFP/G-PANI/Pd_{NP} exhibited a much wider active range for FA oxidation. That is, FA oxidation at CFP/G-PANI/Pd_{NP} took place over -0.1 to about +0.8 V while that for CFP/G-PANI/Pd_{SP} was limited to -0.1 to +0.35 V. These observations show that the preformed Pd nanoparticles gave much more active palladium-polyaniline composites than did the spontaneous deposition of Pd.

Figure 3-7B also shows that the onset for FA oxidation at all the CFP/PANI/Pd_{NP} electrodes was at ca. -0.1 V. Nevertheless, it is clear that CFP/PD-PANI/Pd_{NP} had the lowest activity towards FA oxidation whereas both CFP/P-PANI/Pd_{NP} and CFP/G-PANI/Pd_{NP} displayed similarly remarkable activities. It is noteworthy that all three composites show noticeably better performances than their corresponding CFP/PANI/Pd_{SP} counterparts. As presented in figure 3-5, CFP/PD-PANI/Pd_{SP} exhibited poor activity for FA oxidation (ca. 0.5 mA at +0.1 V) while CFP/PD-PANI/Pd_{NP} gave substantially higher activity (ca. 6 mA at +0.1 V). A similar factor of ca. 10 improvement from the spontaneous deposition to the drop coating method was observed for all the three types of the CFP/PANI.

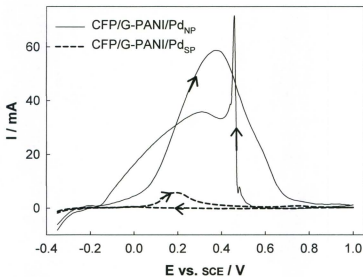


Figure 3-8. Comparative voltammetric responses of CFP/G-PANI/Pd_{SP} and CFP/G-PANI/Pd_{NP} electrodes at 10 mV s⁻¹ in 0.5 M H₂SO₄ containing 0.5 M FA.

Constant potential oxidation of FA was also employed to further inspect the trends observed in the voltammograms. Figure 3-9 shows chronoamperometric responses of the CPF/PANI/Pd_{NP} composites towards FA at various potentials. The time scale for +0.1 V was chosen as 2000 s to test the stability of the catalysts. In the CAs, both CFP/G-PANI/Pd_{NP} and CFP/P-PANI/Pd_{NP} were superior to CFP/PD-PANI/Pd_{NP} at all potentials, consistent with the voltammetric results.

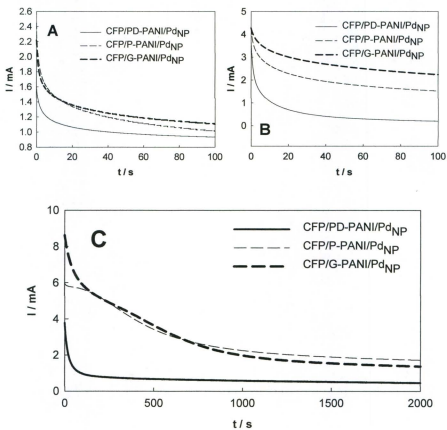


Figure 3-9. Chronoamperometric responses at $E = -0.1$ (A), 0 (B), and $+0.1 \text{ V}$ (C) for CFP/PD-PANI/Pd_{NP}, CFP/P-PANI/Pd_{NP}, and CFP/G-PANI/Pd_{NP} electrodes in $0.5 \text{ M H}_2\text{SO}_4$ containing 0.5 M FA .

However, while CFP/G-PANI/Pd_{NP} and CFP/P-PANI/Pd_{NP} gave similar initial activities (consistent with the CVs in figure 3-7), the rate of decay for CFP/G-PANI/Pd_{NP} was lower at -0.1 and 0 V , indicating greater stability at low potentials. In contrast,

CFP/G-PANI/Pd_{NP} exhibited more rapid decay at +0.1 V, while CFP/P-PANI/Pd_{NP} was more stable at this potential. Nevertheless, unlike the CAs for the CFP/PANI/Pd_{SP} composites, CAs for the CFP/PANI/Pd_{NP} composites up to $t = 800$ s exhibited the same general trend at all potentials with CFP/G-PANI/Pd_{NP} and CFP/PD-PANI/Pd_{NP} giving the highest and lowest activities, respectively.

Due to appreciably high activity of the CFP/PANI/Pd_{NP} composites, it was intended to investigate whether the PANI supports had any synergetic effects on the activity of Pd towards FA oxidation. Here, by means of the drop coating method, we were able to compare a CFP/Pd_{NP} electrode (CFP drop coated with the Pd NP solution) with the CFP/PANI/Pd_{NP} composites. Unfortunately, it would be impractical to make a similar comparison for the CFP/PANI/Pd_{SP} composites since Pd cannot be quantitatively loaded onto CFP using the spontaneous deposition method described in this work.

Figure 3-10 presents overlaid CVs of the CFP/Pd_{NP}, CFP/PD-PANI/Pd_{NP}, and CFP/G-PANI/Pd_{NP} electrodes in the absence (A) and presence (B) of 0.5 M FA. In the blank CVs, CFP/Pd_{NP} can be clearly identified by its significantly stronger $H_{ads,des}$ signals indicating an inhibitory effect of PANI on the electrochemistry of hydrogen at the Pd particles. Considering the 50 μ g loading for Pd NP with an average particle size of 6.4 nm, a theoretical active area of ca. 39.3 cm^2 was obtained. Then, by integrating the H_{ads} signal for CFP/Pd_{NP} one may obtain ca. 24.5 cm^2 as the experimental active area which indicates a 62% utilization. However, the hydrogen signals for the CFP/PANI/Pd_{NP} composites are too suppressed to produce meaningful utilization values.

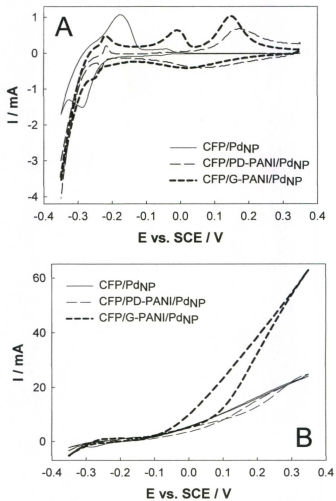


Figure 3-10. Cyclic voltammograms of CFP/Pd_{NP}, CFP/G-PANI/Pd_{NP}, and CFP/PD-PANI/Pd_{NP} in the absence (A) and presence (B) of 0.5 M FA in 0.5 M H₂SO₄ at a scan rate of 10 mV s⁻¹.

Unfortunately, due to the large background of the PANI supports, it was not possible to obtain useful results from Cu underpotential deposition/stripping for the CFP/PANI/Pd_{NP} composites (neither for the CFP/PANI/Pd_{SP} composites) to estimate their corresponding experimental active areas.

Nevertheless, figure 3-10B exhibits FA oxidation onsets of about -0.1 V for all three composites though CFP/G-PANI/Pd_{NP} displayed remarkably higher activity to FA for the rest of the oxidation region ($E > 0$ V). Here, comparison of CFP/PD-PANI/Pd_{NP} and CFP/Pd_{NP} indicates that CFP/PD-PANI would not be a promising alternative to CFP as a support for the oxidation of FA at Pd. On the other hand, the superiority of CFP/G-PANI/Pd_{NP} (and also CFP/P-PANI/Pd_{NP}) to CFP/Pd indicates that slow polymerization conditions lead to the production of CFP/PANI supports that accelerate FA oxidation at Pd. This is consistent with a recent communication concerning the promotional effect of a thin layer of G-PANI on the oxidation of FA at Pd nanoparticles.³¹ Shown in figure 3-10B, the substantial activities of the CFP/PANI/Pd_{NP} and CFP/Pd_{NP} composites justified comparing long term constant potential oxidation of FA at them to illustrate the relative stabilities of this series of catalysts.

Figure 3-11 displays comparative chronoamperometric responses of the CFP/Pd_{NP} and CFP/PANI/Pd_{NP} composites at +0.1 V in the presence of 0.5 M FA over a 2000 s timescale. Herein, although long-term CAs of the composites showed significant current decreases, particularly in the early stages of the polarization, it is notable that the current losses for CFP/P-PANI/Pd_{NP} and CFP/G-PANI/Pd_{NP} were only about 50-60% while that for CFP/Pd_{NP} was more than 70% after 2000 s of polarization. These results clearly

demonstrate the importance of the nature of the support in the present system, and can be attributed to more facile direct formic acid oxidation (direct production of CO_2) and/or inhibition of the formation of poisoning species such as carbon monoxide at Pd to sustain turnover of the active sites. As future work, beyond the scope of this thesis, it would be interesting to investigate whether the PANI supports have any mechanistic effects (e.g. oxidation of CO through a bifunctional mechanism) and/or third body effects (e.g. geometric effects) on the Pd nanoparticles.

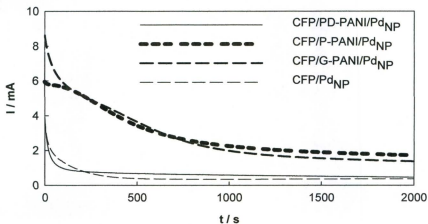


Figure 3-11. Chronoamperometric responses of CFP/Pd_{NP}, CFP/G-PANI/Pd_{NP}, CFP/P-PANI/Pd_{NP}, and CFP/PD-PANI/Pd_{NP} in 0.5 M H_2SO_4 containing 0.5 M FA at +0.1 V.

3.3.5. Impedance spectroscopy

It is shown in this chapter that PANI supports prepared under various electrochemical conditions can have considerable impacts on the electrochemical characteristics of the resulting CFP/PANI/Pd composites. In fact, it was found that CFP/PANI/Pd composites incorporating different PANI supports behave toward the oxidation of FA quite differently. As well, we have shown that while CFP/PD-PANI/Pd composites gave the higher electrochemical active area (stronger H_{ads} and H_{des} signals) compared to the other two PANI-supported catalysts, they exhibited the lowest activities for FA oxidation. The more pronounced hydrogen electrochemistry of CFP/PD-PANI/Pd_{SP} was consistent with the TEM images (see figure 3-4) which showed significantly smaller Pd particles (ca. 5 nm) than both CFP/P-PANI/Pd_{SP} and CFP/G-PANI/Pd_{SP}. As a result, it can be assumed that the electrochemical oxidation of FA at the CFP/PANI/Pd composites was mainly affected by the electronic and/or ionic properties of the PANI supports and not necessarily by the active area of the Pd particles. This was also supported by the fact that while CFP/Pd_{NP} gave a ca. 10 times larger H_{ads} and H_{des} peaks than all the other composites, it was remarkably inferior to both the CFP/P-PANI/Pd_{NP} and CFP/G-PANI/Pd_{NP} electrodes for FA oxidation. Therefore, electrochemical impedance spectroscopy as a powerful technique for conducting polymer studies was used to unveil the actual importance of the electronic/ionic characteristics of the PANI supports.³⁵

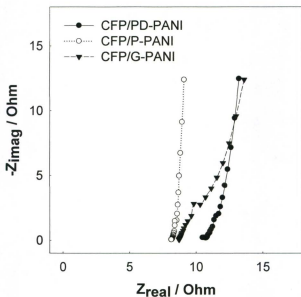


Figure 3-12. Complex plane impedance plots at +0.1 V for PD-PANI, P-PANI, and G-PANI coated CFP electrodes in 0.5 M H_2SO_4 .

Figure 3-12 presents complex-plane plots (Nyquist) of the CFP/PD-PANI, CFP/P-PANI, and CFP/G-PANI electrodes at +0.1 V. Nyquist plots for all three electrodes at high and midrange frequencies were dominated by a charge transfer resistance (negligible for CFP/P-PANI, and CFP/G-PANI at all potentials and for CFP/PD-PANI at +0.1) and/or Warburg-like region (an approximately 45° line) approximating the behaviour of a porous electrode. Warburg-like behaviour corresponds to the combined electronic resistance ($R_{\text{electronic}}$) and ion resistance (R_{ionic}) of the electrode ($R_{\text{Warburg}} = (R_{\text{electronic}} + R_{\text{ionic}})/3$) which is followed by a low frequency capacitive behaviour.⁵⁰ The very short

Warburg-like region for the CFP/P-PANI electrode indicates that its electronic and ionic resistances were quite insignificant at +0.1 V. In contrast, the CFP/G-PANI electrode displayed the longest Warburg region, although the PANI resistance was still low ($< 15 \Omega$), and should not have greatly influenced the FA oxidation current.

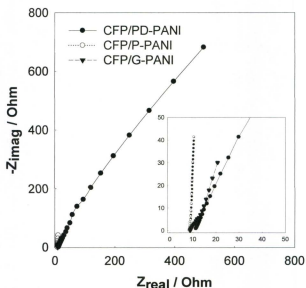


Figure 3-13. Complex plane impedance plots at -0.1 V for PD-PANI, P-PANI, and G-PANI coated CFP electrodes in 0.5 M H_2SO_4 (inset: expanded high frequency region)

The differences in high frequency resistances seen in figure 3-12 were most likely due to differences in the bulk solution resistance, $R_{solution}$, which could not easily be controlled because of small differences in the areas of the CFP electrodes exposed to the electrolyte and small differences in the positioning of the electrodes. However, there is an

indication for the CFP/PD-PANI of a small charge transfer resistance at high frequencies. Comparable values of the imaginary impedance at +0.1 V for all three electrodes indicate their similar capacitive behaviours.

In contrast to the similar impedance responses of the three CFP/PANI films at +0.1 V, they exhibited notably different features at -0.1 V, figure 3-13 (Nyquists at -0.1 V). At this potential, CFP/P-PANI and CFP/G-PANI showed low impedances which did not change significantly from those at +0.1 V, while CFP/PD-PANI displayed much larger impedances at -0.1 V. This clearly shows that CFP/PD-PANI becomes non-conductive at the potential (~ -0.1 V) at which FA oxidation at Pd initiates (at the present composites).

Better visualization of the potential dependent impedances of the CFP/PANI electrodes can be obtained with the series capacitance plots ($-1/\omega Z_{\text{imag}}$ vs. the real impedance, where ω is the radial frequency and Z_{imag} is the imaginary impedance)^{51, 52} shown in figure 3-14A-C.

Although the shapes of these plots are complex because of the use of 3-dimensional CPF electrodes, they do clearly show how the low frequency, limiting capacitance and PANI resistance vary with potential. The slope of the rising portion of the capacitance plot is proportional to the conductivity of the PANI and is dominated by the smaller of the ionic or electronic conductivity. The real impedance at the point where the series capacitances begins to level off approximately represents the solution resistance plus one third of the resistance of the CFP/PANI layer (i.e. $R_{\text{solution}} + R_{\text{Warburg}}$).^{51, 52}

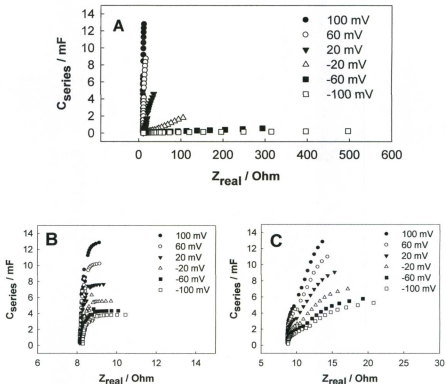


Figure 3-14. Series capacitance plots for CFP/PD-PANI (A), CFP/P-PANI (B), and CFP/G-PANI (C) coated CFP electrode in 0.5 M H₂SO₄. Potentials are vs. SCE.

It is clear from the data in figure 3-14 that the CFP/G-PANI film had a low resistance ($[Z_{\text{real}} - R_{\text{solution}}] \times 3$) at all potentials employed, and that its resistance did not change greatly with potential. This resistance is presumably dominated by the ionic resistance of the PANI, since it did not change significantly with potential. In contrast, the series capacitance of the CFP/G-PANI increased significantly with

increasing potential, which is consistent with the increasing current seen in cyclic voltammetry over this range. CFP/P-PANI gave a similar impedance response over the same potential range, with very similar capacitances (also increasing with potential) but somewhat lower resistances. CFP/PD-PANI (figure 3-14A) also displayed similar capacitances (increasing with potential) and resistances to those of CFP/G-PANI and CFP/P-PANI at the highest potentials (+0.06 mV and +0.1 mV), but its resistance increased sharply and its capacitance decreased sharply at lower potentials. The increase in resistance was most likely due to an increase in the electronic resistance of the PANI as it was reduced to its non-conducting form over the ca. +0.06 V to -0.06 V range. Its earlier (i.e. at higher potentials) loss of electronic conductivity relative to CFP/G-PANI and CFP/P-PANI is consistent with the lower currents seen in its voltammogram at low potentials (figure 3-1), which are also consistent with the loss of capacitance observed for CFP/PD-PANI. In contrast, both CFP/G-PANI and CFP/PPANI must remain partially oxidized and electronically conducting at potentials as low as -0.1 V.

For the case of spontaneously deposited Pd, the differences in electronic resistances observed for the three types of PANI clearly do not provide a direct explanation for the differences in activities of the corresponding CFP/PANI/Pd_{sp} electrodes, since large differences in activity were maintained at +0.1 V when all three forms exhibited low resistances. However, the differences in resistances and/or capacitances at low potentials could have exerted an indirect influence through their effects on the Pd deposition process.^{39, 53} Since the reduced form of the PANI acts as a chemical reductant in this method, differences in its chemical and electrochemical

characteristics can play a large role in determining the morphology of the Pd. It appears to be reasonable to conclude that the low capacitances and high resistances of the CFP/PD-PANI at low potentials (figure 3-14A) played a role in limiting the size of the Pd particles that were formed (TEM images: figure 3-4). On the other hand, there seemed to be correlations between activities of the CFP/PANI/Pd_{NP} composites and the physicochemical properties of the PANI supports. That is, in the case of FA oxidation on the CFP/PANI/Pd_{NP} electrodes, CFP/P-PANI/Pd_{NP} and CFP/G-PANI/Pd_{NP} showed quite similar performances, and both were markedly superior to CFP/PD-PANI/Pd_{NP} (see figure 3-7). This clearly provides evidence for the role of capacitances and resistances of the PANI support at low potentials in the electrochemical performances of the resulting composites.

3.4. Concluding remarks

Spontaneous deposition and drop coating methods were used to impregnate three CFP/PANI supports with Pd species to fabricate CFP/PANI/Pd_{SP} and CFP/PANI/Pd_{NP} composites, respectively. It was shown that the electrocatalytic activity of these composites towards FA oxidation greatly depends on the polymerization conditions for preparation of the CFP/PANI supports. CFP/G-PANI and CFP/P-PANI were found to be superior supports to CFP/PD-PANI characterized typically by their lower oxidation onset and higher activities for FA oxidation. On the other hand, it was revealed that CFP/PANI/Pd_{NP} composites gave substantial activities for FA oxidation, remarkably higher than their CFP/PANI/Pd_{SP} counterparts. However, both methods showed similar

trends for the three PANI supports, validating the methodology presented in this work. Furthermore, it was shown by comparing CFP/Pd_{NP} and CFP/PANI/Pd_{NP} composites that CFP/G-PANI and CFP/P-PANI electrodes were better supports than CFP for FA oxidation at the Pd particles whereas CFP/PD-PANI was not. Considering these observations, electrochemical impedance spectroscopy (EIS) was conducted to study the electronic/ionic characteristics of the PANI supports to address the different activities. Based on the EIS results, one may suggest that the electronic conductivity and/or capacitance of the PANI supports played a significant role in determining the morphology, particle size, and electrocatalytic activity of the spontaneously deposited Pd. That is, CFP/PD-PANI which dramatically loses conductivity and capacitance with lowering potential, gave CFP/PD-PANI/Pd_{SP} with poor activity even though it displayed the highest electrochemically active area. The higher activity of CFP/G-PANI/Pd_{SP} compared to that of CFP/P-PANI/Pd_{SP} may be explained by their different Pd loadings (70 vs. 50 µg, respectively) and/or their different particle sizes (17 vs. 25 nm, respectively). This can be further supported by the similar activities of CFP/G-PANI/Pd_{NP} and CFP/P-PANI/Pd_{NP} (both having similar impedance behaviours and the same Pd sizes and loadings). Also, the trend seen for activities of the CFP/PANI/Pd_{NP} composites would suggest that the electronic/ionic conductivity of the PANI films at the onset potential of the FA oxidation (ca. -0.1 V) can further affect activity of the resulting composites.

References

1. X. Yu and P. G. Pickup, *J. Power Sources*, 2008, **182**, 124-132.
2. S. Ha, B. Adams and R. I. Masel, *J. Power Sources*, 2004, **128**, 119-124.
3. S. Ha, R. Larsen, Y. Zhu and R. I. Masel, *Fuel Cells*, 2004, **4**, 337-343.
4. S. Ha, R. Larsen and R. I. Masel, *J. Power Sources*, 2005, **144**, 28-34.
5. J. Yeom, G. Z. Mozsgai, B. R. Flachsbar, E. R. Choban, A. Asthana, M. A. Shannon and P. J. A. Kenis, *Sensors and Actuators B: Chemical*, 2005, **107**, 882-891.
6. D. Umit B, *J. Power Sources*, 2007, **169**, 239-246.
7. E. Antolini and E. R. Gonzalez, *Appl. Catal., A*, 2009, **365**, 1-19.
8. T. Cheng and E. Gyenge, *J. Appl. Electrochem.*, 2009, **39**, 1925-1938.
9. P. Hong, S. Liao, J. Zeng and X. Huang, *J. Power Sources*, 2010, **195**, 7332-7337.
10. S. M. Baik, J. Han, J. Kim and Y. Kwon, *Int. J. Hydrogen Energy*, 2011, **36**, 14719-14724.
11. C. Lamy, S. Rousseau, E. M. Belgsir, C. Coutanceau and J. M. LÅger, *Electrochim. Acta*, 2004, **49**, 3901-3908.
12. L. Niu, Q. Li, F. Wei, X. Chen and H. Wang, *J. Electroanal. Chem.*, 2003, **544**, 121-128.
13. S. Wasmus and A. Kuver, *J. Electroanal. Chem.*, 1999, **461**, 14-31.
14. T. T. Cheng and E. L. Gyenge, *J. Electrochem. Soc.*, 2008, **155**, B819-B828.
15. D. Curran, J. Grimshaw and S. D. Perera, *Chem. Soc. Rev.*, 1991, **20**, 391-404.
16. A. Deronzier and J. C. Moutet, *Acc. Chem. Res.*, 1989, **22**, 249-255.

17. M. E. G. Lyons, *Analyst*, 1994, **119**, 805-826.
18. C. Liao, Z. D. Wei, S. G. Chen, L. Li, M. B. Ji, Y. Tan and M. J. Liao, *The Journal of Physical Chemistry C*, 2009, **113**, 5705-5710.
19. G. Wu, L. Li, J.-H. Li and B.-Q. Xu, *Carbon*, 2005, **43**, 2579-2587.
20. G. Wu, L. Li, J.-H. Li and B.-Q. Xu, *Journal of Power Sources*, 2006, **155**, 118-127.
21. C. T. Hable and M. S. Wrighton, *Langmuir*, 1993, **9**, 3284-3290.
22. W. T. Napporn, H. Laborde, J. M. Leger and C. Lamy, *J. Electroanal. Chem.*, 1996, **404**, 153-159.
23. M. Hepel, *J. Electrochem. Soc.*, 1998, **145**, 124-134.
24. P. O. Esteban, J. M. Leger, C. Lamy and E. Genies, *J. Appl. Electrochem.*, 1989, **19**, 462-464.
25. V. E. Kazarinov, V. N. Andreev, M. A. Spitsyn and A. P. Mayorov, *Electrochim. Acta*, 1990, **35**, 1459-1463.
26. H. Laborde, J. M. Leger and C. Lamy, *J. Appl. Electrochem.*, 1994, **24**, 219-226.
27. A. Kitani, T. Akashi, K. Sugimoto and S. Ito, *Synth. Met.*, 2001, **121**, 1301-1302.
28. H. H. Zhou, S. Q. Jiao, J. H. Chen, W. Z. Wei and Y. F. Kuang, *J. Appl. Electrochem.*, 2004, **34**, 455-459.
29. D. W. Hatchett, R. Wijeratne and J. M. Kinyanjui, *J. Electroanal. Chem.*, 2006, **593**, 203-210.
30. C. Liao, Z. D. Wei, S. G. Chen, L. Li, M. B. Ji, Y. Tan and M. J. Liao, *J. Phys. Chem. C*, 2009, **113**, 5705-5710.

31. R.B. Moghaddam and P.G. Pickup, *Electrocatalysis*, 2011, **2**, 159-162.
32. H. Gharibi, K. Kakaei and M. Zhiani, *J. Phys. Chem. C*, 2010, **114**, 5233-5240.
33. G. Garcia-Belmonte and J. Bisquert, *Electrochim. Acta*, 2002, **47**, 4263-4272.
34. V. F. Lvovich, *The Electrochemical Society Interface Spring*, 62.
35. I. Rubinstein, E. Sabatani and J. Rishpon, *J. Electrochem. Soc.*, 1987, **134**, 3078-3083.
36. V. Branzoi, L. Pila and F. Branzoi, *Electroanalysis*, 2009, **21**, 557-562.
37. C. Dalmolin, S. R. Biaggio, R. C. Rocha and N. Bocchi, *J. Solid State Electrochem.*, 2007, **11**, 609-618.
38. F. Chen and P. Liu, *Chem. Eng. J.*, 2011, **168**, 964-971.
39. A. Mourato, A. S. Viana, J. P. Correia, H. Siegenthaler and L. M. Abrantes, *Electrochim. Acta*, 2004, **49**, 2249-2257.
40. J. Stejskal, A. Riede, D. Hlavata, J. Prokes, M. Helmstedt and P. Holler, *Synth. Met.*, 1998, **96**, 55-61.
41. V. Syritski, K. Idla and A. Opik, *Synth. Met.*, 2004, **144**, 235-239.
42. R. B. Moghaddam and P. G. Pickup, *Phys. Chem. Chem. Phys.*, **12**, 4733-4741.
43. J. H. Park, J. M. Ko, O. O. Park and D. W. Kim, *J. Power Sources*, 2002, **105**, 20-25.
44. X. M. Ren and P. G. Pickup, *J. Electroanal. Chem.*, 1995, **396**, 359-364.
45. T. Kim, J. Kim, Y. Kim, T. Lee, W. Kim and K. S. Suh, *Current Applied Physics*, 2009, **9**, 120-125.
46. C. Li, G. Shi, Y. Liang and Z. Sha, *Polymer*, 1997, **38**, 6421-6422.

47. S. Osawa, T. Ogawa and M. Ito, *Synth. Met.*, 1997, **90**, 109-113.
48. S. Eliseeva, E. Ubyivovk, A. Bondarenko, O. Vyvenko and V. Kondratiev, *Russ. J. Gen. Chem.*, 2010, **80**, 1143-1148.
49. R. B. Moghaddam and P. G. Pickup, *Electrochem. Commun.*, 2011, **13**, 704-706.
50. X. Ren and P. G. Pickup, *J. Chem. Soc., Faraday Trans.*, 1993, **89**, 321-326.
51. M. C. Lefebvre, R. B. Martin and P. G. Pickup, *Electrochem. Solid-State Lett.*, 1999, **2**, 259-261.
52. X. Ren and P. G. Pickup, *Electrochim. Acta*, 2001, **46**, 4177-4183.
53. A. Mourato, J. P. Correia, H. Siegenthaler and L. M. Abrantes, *Electrochim. Acta*, 2007, **53**, 664-672.

Chapter 4

**Support effects on the oxidation of
methanol at Pt nanoparticles**

Chapter 4. Support effects on the oxidation of methanol at Pt nanoparticles

This work has been published in part as *Moghaddam, R.B. and Pickup P.G., Support effects on the oxidation of methanol at platinum nanoparticles, Electrochemistry Communications 2011, 13, 704-706*. The text was written in part by Dr. Peter Pickup.

4.1. Introduction

The remarkable energy output of direct methanol fuel cells (DMFCs) makes them an important subcategory of fuel cells, which have long been a center of attention in academia and technology as efficient energy producing devices.¹⁻³ In this respect, a great deal of research has been increasingly devoted to studying the oxidation of methanol as the central reaction in the anode of a DMFC.^{1, 3-15} Particularly, much attention has been focused on preparation of improved catalysts, mainly based on Pt as the catalyst of choice, to decrease the large overpotential and increase the kinetics of methanol oxidation, and to avoid detrimental adsorption of poisoning intermediates (e.g. CO).² Combining Pt with metals such as Ru and making its composites with conducting polymers such as polyaniline (PANI) have been shown to greatly improve the performance of Pt catalysts in the oxidation of methanol. As well, it was shown in a number of studies that deposition of Pt onto Ru oxide¹⁶ and PANI^{14, 17} substrates was effective for promoting the oxidation of methanol and CO at those composite catalysts.

However, even though it is well understood that the presence of a modifier such as Ru in proximity to Pt (e.g. in an alloy, as a support, or in a physical mixture) improves its activity, the actual role of modifiers serving as supports is still elusive. In fact, most of

the methods used for deposition of catalysts could make considerable change in the structure and morphology of the support (e.g. electrodeposition which requires applying a potential/current to the working electrode). Moreover, use of such methods could lead to a significant amount of the catalyst species diffusing into the support layer which would create a mixture (e.g. alloy) rather than a layered structure. Therefore, it is unclear whether changes in activity for such mixtures can be attributed to pure support effects.

On this basis, we have developed methodology to more clearly elucidate the effects of Ru oxide and PANI supports on the electrocatalytic activity of Pt nanoparticles in the oxidation of methanol. To achieve this goal, we aimed at making thin-layer supports and using drop coating of preformed Pt nanoparticles to decrease the possible effects of diffusion and structural changes on the system. In this regard, polyaniline and Ru oxide supports were chosen as model systems, since both of them have been shown in a number of studies to promote methanol oxidation at Pt. Here, we adopted a facile method to prepare an Ru oxide modified glassy carbon electrode through spontaneous reduction of Ru(VII),^{18, 19} and utilized galvanostatic polymerization of aniline to fabricate thin layers of the two supports. The use of preformed Pt nanoparticles²⁰ negates the influences of the support on the nature of the catalyst particles^{21, 22} in order to unveil true support effects on the oxidation of methanol.

4.2. Experimental

4.2.1. Chemicals

Sulfuric acid (Fisher Scientific), methanol (Sigma Aldrich, HPLC grade), KRuO_4 (Alfa Aesar), $\text{H}_2\text{PtCl}_6 \cdot 6\text{H}_2\text{O}$ (Alfa Aesar), sodium citrate (Anachemia), potassium hydroxide (ACP Chemical Inc.), Nafion™ solution (5%; Dupont) and sodium borohydride (Sigma Aldrich) were used as received. Aniline (Sigma Aldrich) was purified by passing through an alumina (neutral) chromatography column prior to use. Doubly distilled water was used throughout the experiments. All measurements were recorded under a nitrogen atmosphere following purging for 15 min.

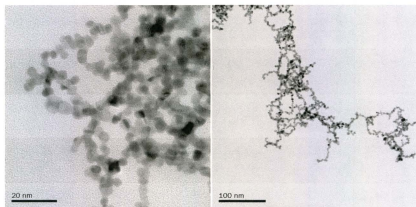


Figure 4-1. Transmission electron microscopy images of colloidal Pt nanoparticles (deposited on a Cu grid).

4.2.2. Preparation of Pt nanoparticles

To prepare the colloidal Pt nanoparticle solution, 10 mL of 3 mM $\text{H}_2\text{PtCl}_6(\text{aq})$ was mixed with 0.6 mL of 50 mM aqueous sodium citrate and stirred vigorously while 1.5 mL of 120 mM $\text{NaBH}_4(\text{aq})$ was added dropwise. Following stirring for a further 2 h, the resulting grey colloidal Pt nanoparticle solution was stored in a fridge. This stock solution was diluted by a factor of 10 with water and Nafion solution prior to use to give $48 \mu\text{g mL}^{-1}$ Pt and $2.4 \mu\text{g mL}^{-1}$ Nafion. X-ray diffraction measurements indicated that the average particle diameter was 5.0 ± 0.4 nm. This result is consistent with the particle sizes (5.0 ± 1.3 nm) seen by transmission electron microscopy, figure 4-1, which also confirmed the narrow size distribution previously reported for this synthesis method.²³

4.2.3. Working electrode preparation

Glassy carbon electrodes (GC; CH Instruments; 0.071 cm^2) were polished with $0.05 \mu\text{m}$ alumina and rinsed well with water before use. They were coated with a thin layer of hydrous Ru oxide (GC/Ru oxide), as required, by the following procedure.^{19, 24} The GC electrode was conditioned at -0.5 V for 300 s in 0.1 M H_2SO_4 , rinsed with water, and then placed in aqueous 0.05 M KRuO_4 (in 0.1 M KOH) for 15 min. It was then rinsed thoroughly with water and placed in lightly stirred, distilled water for 5 min to ensure removal of all non-chemically attached Ru species. The presence of Ru oxide on the electrode surface was confirmed by microprobe analysis (energy dispersive X-ray emission) which showed the presence of C, O and Ru, but no other elements. Scanning electron microscopy of the modified surface was featureless, indicating that the Ru oxide

had deposited as a thin film, as observed on carbon nanotubes and carbon fabric.^{18, 19} Analysis by inductively coupled plasma mass spectrometry (ICP-MS) gave a Ru loading of 1.3×10^{-6} g. Polyaniline (PANI) coated GC electrodes (GC/PANI) were prepared by galvanostatic polymerization ($I = 3.5 \mu\text{A}$, $t = 150$ s) of 0.1 M aniline in 0.5 M H_2SO_4 . The GC, GC/Ru oxide, and GC/PANI electrodes were drop coated with 12.5 μL of the diluted Nafion-containing Pt colloid to obtain GC/Pt, GC/Ru oxide/Pt, and GC/PANI/Pt electrodes with Pt loadings of $\sim 7.2 \times 10^{-7}$ g ($\sim 10 \mu\text{g cm}^{-2}$) with 5% Nafion by mass relative to Pt. In one case, the quantity of Pt on a GC/Ru oxide/Pt electrode was determined by ICP-MS to be 5.6×10^{-7} g. This quantity of Pt nanoparticles would correspond to ca. two close-packed monolayers.

4.2.4. Instrumentation

An EG&G Model 273A Potentiostat/Galvanostat run by a PC through M270 commercial software was used for voltammetric measurements. A saturated calomel electrode (SCE) and a platinum wire formed the reference and counter electrode, respectively.

A Model FEI Quanta 400 environmental SEM was used to perform scanning electron microscopy (SEM) measurements. For transmission electron microscopy (TEM), the colloidal Pt nanoparticle solution was diluted with ethanol and sonicated for several minutes. A drop of the mixture was then placed on a 200 mesh copper grid with a carbon support film. The grid was allowed to dry overnight and then observed under a Model JEOL 2011 transmission electron microscope (The Microscopy and Microanalysis

Facility, University of New Brunswick). Atomic force microscopy (AFM) measurements were conducted with a Quesant Q-Scope 350 using a smooth glassy carbon plate (SPI Supplies, USA) as the substrate.

4.3. Results and discussion

4.3.1. Characterization of the Pt nanoparticles

Figure 4-2 presents a cyclic voltammogram of a GC electrode coated with ca. 10 $\mu\text{g cm}^{-2}$ Pt nanoparticles. The CV shows characteristic voltammetry for Pt, with H electrochemistry below 0 V and oxide formation/stripping at potentials above +0.3 V. Here, the negative tail of the CV is dominated by clearly defined signals of hydrogen adsorption/desorption (H_{ads} and H_{des}) in the cathodic and anodic scans, respectively, and the hydrogen evolution current spike below -0.22 V. Generally, H_{ads} and H_{des} signals are characteristics of a few transition metals such as Pt, Pd, Rh, and Ir. In theory, the appearance of such waves indicates strong interactions (i.e. energetically favoured) between hydrogen and the metal atoms.²⁵ Usually, these characteristic signals are useful to estimate the electrochemical active surface area (EASA) of such metals. Here for a Pt electrode, the $EASA_{\text{Pt}}$ can be calculated using eq. 4-1.^{26,27}

$$EASA_{\text{Pt}} = Q_{\text{H}} / (2.10 \times 10^{-4} \text{ C cm}^{-2}) \quad (4-1)$$

Where Q_{H} stands for the background corrected charge under the H_{ads} signals and 2.10×10^{-4} is the average charge value (in C cm^{-2}) associated with deposition of one monolayer of hydrogen atoms on polycrystalline Pt.^{26,27}

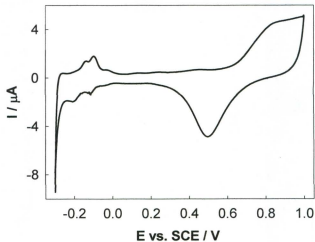


Figure 4-2. Voltammogram of a GC/Pt electrode in 0.1 M H₂SO₄ at a potential sweep rate of 10 mV s⁻¹.

For the GC/Pt electrode, the background corrected area under the H_{ads} peaks yielded an experimental active area of ca. 0.12 cm². Taking into account a theoretical electrochemical active area of ca. 0.41 cm² based on the Pt loading (ca. 10 μg cm⁻²) and an average particle size of 5 nm, one may obtain a utilization of ca. 29%. As well, one may estimate EASA_{Pt} using the background corrected area under the oxide stripping wave (cathodic scan; background corrected area between 0.8 and 0.1 V), eq. 4-2, which is a 2-electron reaction, eq. 4-3.^{26, 27}

$$EASA_{Pt} = Q_{\text{Oxide Stripping}} / (4.20 \times 10^{-4} \text{ C cm}^{-2}) \quad (4-2)$$



Inconsistency of the $EASA_{Pt}$ value from H_{ads} signals (0.12 cm^2) with the $EASA_{Pt}$ value from the oxide stripping wave (0.27 cm^2 active area corresponding to a utilization of ca. 66%) shows that the hydrogen electrochemistry was significantly inhibited at the GC/Pt electrode.

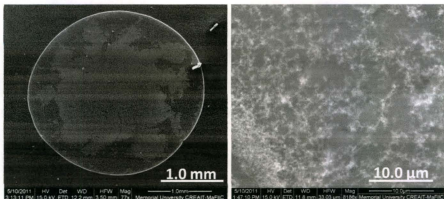


Figure 4-3. Scanning electron microscopy images for $10 \mu\text{g cm}^{-2}$ Pt nanoparticles + 5% Nafion coated on a GC plate.

SEM and AFM measurements were conducted to unveil whether there was any geometric/morphologic evidence for this electronic isolation. Figure 4-3 shows representative SEM images of the Pt nanoparticles coated on a GC plate. Herein, the complete spot image along with view of a selective region of the same spot display an uneven distribution of the Pt+Nafion deposit on the electrode. It can be seen that the Pt nanoparticles randomly concentrated in the middle and also at the edge of the spot with some bare regions between them.

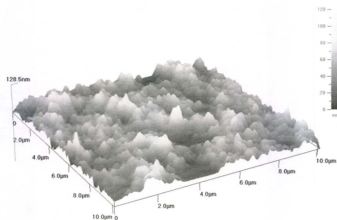


Figure 4-4. Atomic force microscopy (B; $10 \times 10 \mu\text{m} \times 128 \text{ nm}$) images of ca. $10 \mu\text{g cm}^{-2}$ of Pt nanoparticles + 5 % Nafion on a GC plate.

Thereafter, AFM measurement following rinsing with water (to remove residual salts of the synthesis solution) showed similar observations to the SEMs, both indicative of an uneven distribution of the Pt nanoparticles on the GC substrate. However, it was revealed that relatively uniform regions of Pt+Nafion corresponding to ca. 50 nm thickness (see figure 4-4) covered approximately half of the coated GC area. Since approximately equal volumes of Pt and Nafion solids were applied to the electrodes, the Pt+Nafion deposits typically consisted of ca. 5 layers of Pt nanoparticles.

Since the electrochemical active area calculated from the H_{ads} signals gave only a 29% utilization value, the Cu underpotential deposition/stripping method (Cu UPD) described by Green and Kucernak²⁷ was performed for further assessment.

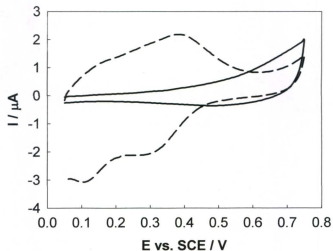


Figure 4-5. Cyclic voltammograms (10 mV s^{-1}) of a GC/Pt electrode in $0.1 \text{ M H}_2\text{SO}_4$ in the absence (solid line) and presence (dashed line) of 0.005 M CuSO_4 .

Due to high tendency of the Cu(II) ions to be reduced at metals such as Pt and Pd, the deposition of one monolayer of Cu atoms from a Cu(II) solution ($\text{Cu}^{2+} + 2\text{e}^- \rightarrow \text{Cu}$) can be carried out at potentials significantly more positive than that for the bulk deposition.^{28, 29} In fact, under this condition, the potential is not sufficiently negative for the Cu(II) ions to be deposited as adlayers on top of the preformed Cu monolayer. To perform underpotential deposition of Cu at the GC/Pt electrode, the electrode was conditioned at $+0.75 \text{ V}$ for 120 s , and then stepped to $+0.05 \text{ V}$ for 100 s to deposit approximately a monolayer of Cu. This UPD Cu was then stripped in a $+0.05$ to $+0.75 \text{ V}$ cyclic scan. Some diagnostic experiments (not shown) were carried out to test the

applicability of the protocol for this system. For instance, the conditioning potential was varied from +0.5 to +0.75 V, and the conditioning step was also excluded in one experiment. It was found that this conditioning step played a key role in obtaining a more efficient Cu stripping process (e.g. more charge under the stripping peak at the anodic scan conditions), although no observable difference was seen for conditioning potentials higher than +0.6 V. This could be assigned to activation of the Pt nanoparticles during conditioning, and/or changes in their structure or arrangement. Furthermore, consistent with Green *et al.*'s report,²⁷ it was found that a slightly more negative deposition potential (e.g. +0.03 V) can activate the bulk deposition of Cu significantly. Therefore, we set the deposition potential at +0.05 V to ensure complete exclusion of the bulk deposition.

Figure 4-5 illustrates CVs of a GC/Pt electrode in the absence and presence of 5 mM CuSO₄ in 0.1 M H₂SO₄ to depict typical Cu UPD behaviour. The electrochemically active Pt area (EASA_{Pt}) of the electrode was estimated by integrating the charge (EASA_{Pt} = $Q_{\text{Cu UPD}} / 4.20 \times 10^{-4} \text{ C cm}^{-2}$) under the anodic portion of the curve between +0.05 and +0.4 V, corrected for the background contribution in the absence of Cu, and found to be ca. 0.16 cm². This gives a utilization of ca. 40% for the GC/Pt electrode which is consistent with the uneven distribution of Pt+Nafion composites on the surface, with half of the Pt content not establishing electronic communication with the electrode surface. However, since the area of the oxide reduction peak (cathodic sweep; +0.7 to +0.2 V) yielded 66% utilization (0.27 cm² active area) and the oxide charge should not exceed the active Pt area, it appears that both H adsorption and Cu UPD on this electrode were suppressed in some way. Nevertheless, based on repeated experiments (not shown), the

EASA_{Pt} estimated by either of the methods, H adsorption and Cu UPD could be subject to some uncertainty (~ 5%), probably as a consequence of uncontrollable experimental errors.

4.3.2. Polyaniline supported Pt

Overlaid CVs of the GC/Pt and GC/PANI/Pt electrodes in 0.1 M H₂SO₄ are presented in figure 4-6. For both cases, as a result of the selected anodic window, poorly defined Pt oxide formation/reduction signals can be seen in the voltammograms. The upper potential limit was restricted to +0.7 V here in order to avoid instability due to oxidative degradation of the polymer at higher potentials. The presence of the PANI layer in GC/PANI/Pt is identified by its large background current in the entire voltammetric range. Furthermore, the oxidation peak at +0.15 V and a broad reduction peak at -0.05 V are presumably due to the electrochemistry of PANI. The thickness of the PANI layer was estimated to be ca. 10 nm based on the charge under the oxidation wave located at +0.15 V, which was integrated between 0 and +0.4 V.³⁰ Interestingly, while only a thin layer of PANI was used as the support, it appears to have greatly inhibited the hydrogen electrochemistry. However, the H_{ads} signal and hydrogen evolution current surge were less affected while the H_{des} twin peaks virtually disappeared. Furthermore, the large background current of the GC/PANI/Pt electrode prohibited accurate integration of the H_{ads} signals.

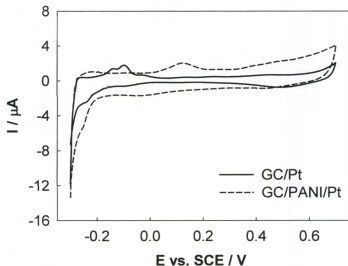


Figure 4-6. Cyclic voltammograms (10 mV s^{-1}) of GC (solid line) and GC/PANI (dashed line) electrodes coated with ca. $10 \mu\text{g cm}^{-2}$ of Pt nanoparticles in $0.1 \text{ M H}_2\text{SO}_4$.

Consequently, only the Cu UPD method explained earlier was performed for the GC/PANI/Pt electrode to obtain the EASA. Figure 4-7 displays cyclic voltammograms of the GC/PANI/Pt electrode in the absence and presence of Cu(II) ions. The active surface area for this electrode was estimated to be 0.18 cm^2 to give a catalyst utilization of ca. 43%. SEM images for the GC/PANI/Pt electrode (not presented) showed that the presence of the PANI layer did not visually change the morphology of the Pt layer on the electrode surface (randomly distributed aggregates leaving uncoated support in some regions; see figure 4-3).

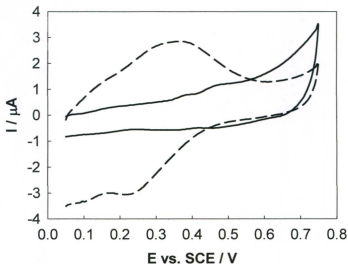


Figure 4-7. Cyclic voltammograms (10 mV s^{-1}) of a GC/PANI/Pt electrode in $0.1 \text{ M H}_2\text{SO}_4$ in the absence (solid line) and presence (dashed line) of 0.005 M CuSO_4 .

Figure 4-8 displays overlaid voltammograms of the GC/Pt and GC/PANI/Pt electrodes in the presence of 0.2 M methanol. As can be observed, multiple scan CVs (10 and 15 scans for the GC/Pt and GC/PANI/Pt electrodes, respectively) were carried out for the two electrodes in order to establish stable voltammetric patterns. Here, GC/PANI/Pt showed a quite low anodic peak current on the first cycle ($\sim 30 \mu\text{A}$ at $+0.57 \text{ V}$), which significantly increased in subsequent cycles with no observable shift of the peak potential (to $\sim 70 \mu\text{A}$ at $+0.57 \text{ V}$). This may be due to changes in the distribution of the nanoparticles incorporated into the polymeric film, partial oxidative dissolution of the PANI layer, oxidation of an adsorbed poison (e.g. aniline), and/or an activation effect by

cycling. However, investigation of this behaviour requires complementary work and was not the scope this preliminary study. On the other hand, GC/Pt showed a stable performance, the limiting current of which ($\sim 70 \mu\text{A}$ at $+0.49 \text{ V}$) and the peak potential remained almost unchanged with cycling.

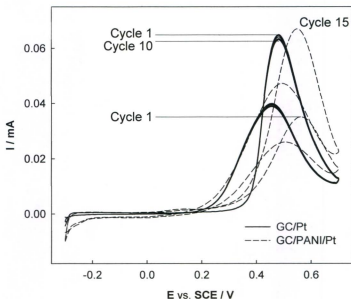


Figure 4-8. Multiple cycle voltammograms (10 mV s^{-1}) of GC (solid line; 10 cycles) and GC/PANI (dashed line; cycles 1 and 15 are shown) electrodes coated with ca. $10 \mu\text{g cm}^{-2}$ of Pt nanoparticles in $0.1 \text{ M H}_2\text{SO}_4$ containing 0.2 M methanol.

It is noteworthy that while the two electrodes displayed similar peak currents (I_p), their peak potentials (E_p) were notably different ($+0.49 \text{ V}$ for GC/Pt vs. $+0.57 \text{ V}$ for

GC/PANI/Pt). Thus the presence of the PANI layer had no promotional effect on the current density and also shifted the peak current to a more positive potential. The more positive peak potential could have originated from inhibited access of methanol to a portion of the Pt species which are in contact with the PANI layer (i.e. innermost layer) and/or weak electronic communication of the electrode with the Pt nanoparticles due to the presence of the PANI layer. However, the oxidation onset for the GC/PANI/Pt electrode was slightly less positive, presumably due to promoted oxidation of CO at the PANI layer, and/or electrochemistry of PANI over this region. Nevertheless, the reverse scan for the GC/PANI/Pt electrode followed the same changes with cycling. That is, it was inferior to the GC/Pt electrode on the first scan but showed more current after cycling.

As shown in the voltammetric results (figure 4-8), the PANI layer did not impart a significant promotional effect on the reaction of methanol at the Pt nanoparticles suggesting that the previous observations of an effect^{14, 17, 31} were due to factors other than a direct interaction of the PANI with the Pt. They could have been due to better Pt dispersion and/or enhanced transport properties of the catalysts, rather than to inherent effects of the PANI on the methanol oxidation mechanism or via electronic effects.

4.3.3. Ru oxide supported Pt

Figure 4-9 presents overlaid cyclic voltammograms of the GC/Pt and GC/Ru oxide/Pt electrodes in 0.1 M H₂SO₄. The voltammogram of the GC/Ru oxide electrode is characterized by its larger background current most noticeable at E > 0 V in both the

forward and reverse scans, and is diagnostic of the presence of the Ru oxide layer. Furthermore, the Pt oxide formation signal is less pronounced for this electrode compared to GC/Pt. In fact, the oxide formation region ($E > +0.6$ V) would have overlapped the oxidation of Ru oxide. Also, on the reverse leg of the CV for the GC/Ru oxide/Pt electrode, the Pt oxide reduction peak had shifted to +0.47 V which is slightly less positive than that for the GC/Pt electrode ($\sim +0.50$ V). Moreover, at about +0.2 V, there seems to be a poorly-defined peak presumably due to the reduction of Ru oxide which overlaps the Pt oxide reduction region.

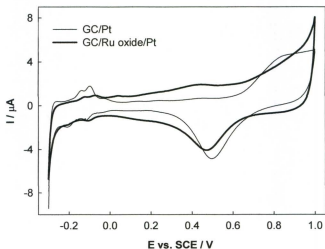


Figure 4-9. Cyclic voltammograms (10 mV s^{-1}) of GC (light) and GC/Ru oxide (heavy) electrodes coated with ca. $10 \mu\text{g cm}^{-2}$ of Pt nanoparticles in $0.1 \text{ M H}_2\text{SO}_4$.

It appears that the Ru oxide layer had an inhibitory effect on the hydrogen electrochemistry at the Pt nanoparticles as the H_{ads} and H_{des} peaks were suppressed significantly. The $EASA_{Pt}$ for the GC/Ru oxide/Pt electrode based on the area under the H_{ads} signals was found to be ca. 0.05 cm^2 which corresponds to a utilization of about 12%. Therefore, the Cu UPD protocol explained earlier was also conducted for this electrode (figure 4-10) giving an active area of ca. 0.25 cm^2 which corresponds to a ca. 61% utilization. This number is higher than the Cu UPD utilization for the GC/Pt electrode (40%) and close to the utilization obtained by integrating the oxide reduction peak of the GC/Pt electrode (66%).

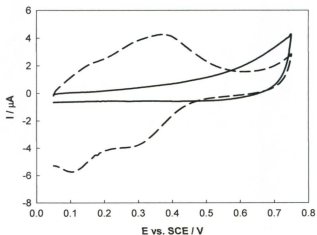


Figure 4-10. Cyclic voltammograms (10 mV s^{-1}) of a GC/Ru oxide/Pt electrode in $0.1 \text{ M H}_2\text{SO}_4$ in the absence (solid line) and presence (dashed line) of 0.005 M CuSO_4 .

Comparative CVs of the GC/Pt and GC/Ru oxide/Pt electrodes in the presence of 0.2 M methanol are presented in figure 4-11. The forward scans of the CVs reveal significant observations. First of all, the oxidation onset for the GC/Ru oxide/Pt electrode was considerably less positive (+0.24 V compared to +0.36 V for the GC/Pt electrode), explicit evidence for a cocatalytic effect of the Ru oxide layer on the oxidation of methanol at the Pt nanoparticles. The voltammogram of the GC/Pt electrode on the forward leg shows a sharp oxidation peak at +0.48 V, in contrast to the forward scan of the GC/Ru oxide/Pt electrode that is dominated by two overlapping peaks over this region.

Here, the forward scan of the GC/Ru oxide/Pt exhibits a shoulder at +0.43 V overlapping a larger wave at +0.52 V. The oxidation current for GC/Ru oxide/Pt reached the peak value for the GC/Pt electrode ca. 90 mV earlier (at +0.40 V vs. SCE, vs. +0.49 V for GC/Pt). Furthermore, inspection of the voltammograms at $E > +0.75$ V displays notable features. In this region, the GC/Ru oxide/Pt electrode gave significantly larger activity at potentials above +0.8 V which became more pronounced towards the end of the scan. The current surge after +0.8 V, presumably due to the direct oxidation of methanol, is substantially sharper for the GC/Ru oxide/Pt electrode suggesting a strong catalytic activity of the Ru oxide layer over this region, or a large synergetic effect on the direct oxidation of methanol at the Pt nanoparticles. Therefore, in order to elucidate the actual effect of the Ru oxide layer, a control experiment in the absence of the Pt nanoparticles on a GC/Ru oxide electrode was performed.

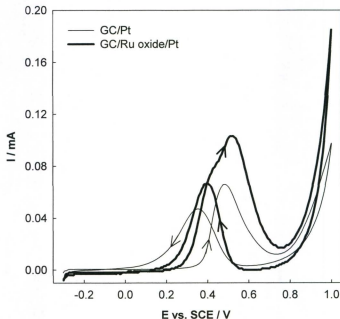


Figure 4-11. Cyclic voltammograms (10 mV s^{-1}) of GC (light) and GC/Ru oxide (heavy) electrodes coated with ca. $10 \mu\text{g cm}^{-2}$ of Pt nanoparticles in $0.1 \text{ M H}_2\text{SO}_4$ containing 0.2 M methanol.

Figure 4-12A shows a cyclic voltammogram of a GC/Ru oxide electrode in $0.1 \text{ M H}_2\text{SO}_4$. Here, typical reversible oxidation and reduction waves (pseudocapacitance) of the hydrous Ru oxide layer¹⁸ can be observed between $+0.2$ to $+0.6 \text{ V}$. At the anodic tail, the electrode exhibited a sharp current surge initiated from about $+0.80 \text{ V}$ which could have been due to formation of hydrous Ru (VI), and possibly superposition of oxygen evolution at the final stages (e.g. $> +0.95 \text{ V}$). This feature can clearly account for the

different voltammetric observations of the the GC/Pt and GC/Ru oxide/Pt over this region (see figure 4-9) where Pt appears to be less active than the Ru oxide layer in the oxidative hydrolysis of H₂O.

CVs of the GC/Ru oxide electrode in the absence and presence of 0.2 M methanol are displayed in figure 4-12B. The electrode exhibited no activity below +0.75 V, where both the anodic and cathodic legs remained unchanged over this region. This clearly indicates that the Ru oxide layer had essentially a cocatalytic effect (i.e. mechanistic and/or electronic) on the Pt nanoparticle activity for methanol oxidation at low potentials (> +0.75 V). The mechanistic aspects of this effect are discussed in section 4.3.4. However, a sharp current surge initiated at ~ +0.75 V points to the independent catalytic activity of the Ru oxide layer at high potentials. Consequently, one may conclude that the larger activity of GC/Ru oxide/Pt compared to GC/Pt at $E > +0.75$ V was due to superimposition of currents of the Pt nanoparticles and the Ru oxide layer in the presence of methanol. Interestingly, current values for the GC/Pt and GC/Ru oxide electrodes at $E = +1$ V were ca. 100 and 75 μ A, summation of which is close to the current for the GC/Ru oxide/Pt electrode at this potential (180 μ A).

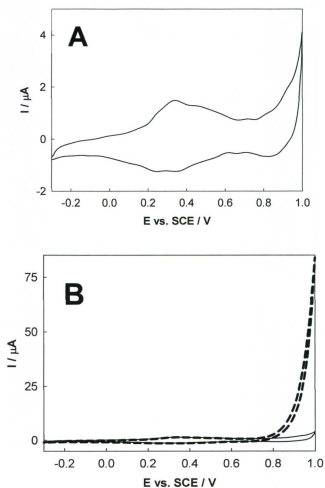


Figure 4-12. (A) Cyclic voltammograms (10 mV s^{-1}) of a GC/Ru oxide electrode in $0.1 \text{ M H}_2\text{SO}_4$; (B) Overlaid CVs of a GC/Ru oxide electrode in $0.1 \text{ M H}_2\text{SO}_4$ in the presence (dashed line) and absence of 0.2 M methanol (solid line).

Further insight into the role of the Ru oxide layer can be obtained by inspection of the reverse sweeps of the GC/Pt and GC/Ru oxide/Pt electrodes (figure 4-11). The two exhibited quite similar onsets (ca. +0.58 V) for rapid oxidation of methanol. As a matter of fact, here the oxidation onsets for both electrodes were close to the onsets for the reduction of Pt oxide in figure 4-9. Consistent with Jiang and Kucernak's report,³² this would clearly signify the inhibitory role of the oxide film (Pt oxide) before the rapid oxidation of methanol during the cathodic scan. Additional evidence for this inhibitory effect³² can be obtained by comparison of the onset potential here with that in figure 4-8 (GC/Pt; cathodic scan) where the rapid oxidation of methanol in the reverse scan initiated at a much more positive potential (+0.7 V). Nevertheless, the GC/Ru oxide/Pt electrode gave I_p of ca. 60 μA at +0.4 V, whereas that for the GC/Pt was only about 45 μA at +0.35 V (figure 4-11; reverse scans). At final stages of the reverse scan ($E < +0.35$ V) the GC/Pt electrode was superior to GC/Ru oxide/Pt which gave much lower current.

To obtain further insight into promotional effects of the Ru oxide layer a series of chronoamperometric experiments were conducted for the GC/Pt and GC/Ru oxide/Pt electrodes over a wide potential range. That is, we selected the range of +0.2 to +0.95 V in which methanol oxidation is active at both electrodes. Note that the CAs were performed following multiple cycling between -0.3 and +1 V in the absence of methanol followed by a single linear sweep from -0.3 to +0.2 V in the presence of 0.2 M methanol.

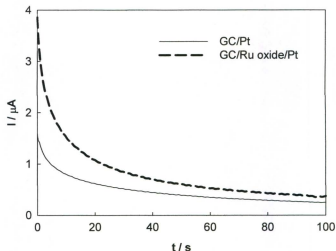


Figure 4-13. Chronoamperometric responses of GC/Pt and GC/Ru oxide/Pt at +0.2 V in 0.1 M H₂SO₄ containing 0.2 M methanol.

Figure 4-13 compares chronoamperometric (CA) responses at +0.2 V in the presence of 0.2 M methanol subsequent to this voltammetric treatment. Both electrodes showed quite low activity for methanol oxidation with GC/Ru oxide/Pt giving a somewhat better initial performance, although both electrodes gave similarly insignificant activities at $t = 100$ s. In a sharp contrast, CAs of the two electrodes at +0.3 V, figure 4-14, shows remarkable superiority of the GC/Ru oxide/Pt at all times. The different activities of the two electrodes at this potential match well with the voltammetric profiles (figure 4-11) in which the oxidation onset for the GC/Ru oxide/Pt electrode was less positive. In fact, it was expected that the GC/Pt electrode would exhibit little activity at

this potential while the GC/Ru oxide/Pt electrode should have been fairly active. Furthermore, CAs of the two electrodes at +0.4, +0.5, and +0.6 V (figures 4-15 and 4-16) consistently followed the trend seen in the voltammograms with GC/Ru oxide/Pt giving higher activity at all of these potentials.

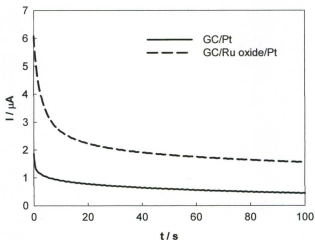


Figure 4-14. Chronoamperometric responses of GC/Pt and GC/Ru oxide/Pt at +0.3 V in 0.1 M H₂SO₄ containing 0.2 M methanol.

Figure 4-15 illustrates CAs of the GC/Pt and GC/Ru oxide/Pt electrodes at +0.4 V. Here, the GC/Pt electrode gave a typical chronoamperometric pattern dominated by a large initial current which decayed over the designated timescale. In contrast, the GC/Ru oxide/Pt electrode at this potential showed more complicated behaviour. That is, the current decreased during the first 3-4 s (probably due to the exponential decay of the background current), after which it increased up until $t \sim 30$ s. This increment, which was

not seen for the GC/Pt electrode, should be ascribed to the effect of the Ru oxide layer in activation of the reaction at the Pt nanoparticles. Taking into consideration the oxidizing nature of the Ru oxide layer, its effect in the oxidation of methanol at +0.4 V could be through a bifunctional mechanism, in which it can act as oxidizing agent to promote oxidation of the poisoning species (e.g. CO) at the Pt nanoparticles. The mechanistic aspects of this effect are discussed in section 4.3.4. After $t \sim 30$, no significant current change was observed until $t \sim 60$ s, where the current slowly began to decay for the remainder of the chronoamperometry.

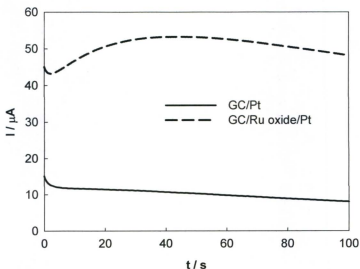


Figure 4-15. Chronoamperometric responses of GC/Pt and GC/Ru oxide/Pt at +0.4 V in 0.1 M H_2SO_4 containing 0.2 M methanol.

Figure 4-16 presents CAs of the GC/Pt and GC/Ru oxide/Pt electrodes at +0.5 and +0.6 V in the presence of 0.2 M methanol. The GC/Ru oxide/Pt electrode was superior at +0.5 V at all times but its initial high activity decayed more rapidly than GC/Pt. The catalytic instability of the GC/Ru oxide/Pt electrode was more pronounced at +0.6 V, which resulted in comparable activity to the GC/Pt electrode at $t = 100$ s.

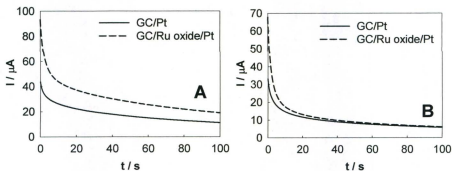


Figure 4-16. Chronoamperometric responses of GC/Pt and GC/Ru oxide/Pt at +0.5 (A) and +0.6 (B) in 0.1 M H_2SO_4 containing 0.2 M methanol.

Chronoamperometric responses of the two electrodes at +0.85 and +0.95 V are presented in figure 4-17. Here the CAs followed the voltammetric results which further indicated catalytic activity of the Ru oxide layer in this region. However, the rate of decay for the GC/Ru oxide/Pt electrode was significantly larger particularly at +0.95 V. This may be ascribed either to lower catalytic stability of Ru oxide (i.e. rapid deactivation) or electrodisolution of Ru at this potential which can greatly decrease activity.

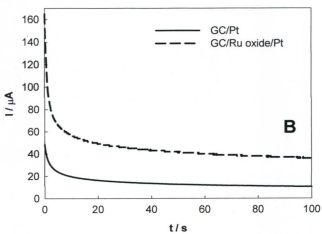
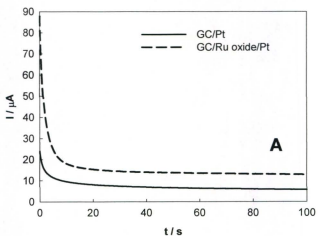


Figure 4-17. Chronoamperometric responses of GC/Pt and GC/Ru oxide/Pt at +0.85 (A) and +0.95 (B) V in 0.1 M H_2SO_4 containing 0.2 M methanol.

4.3.4. Mechanistic insights

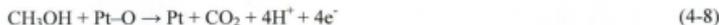
The electrocatalytic oxidation of methanol at Pt is well-known to initiate with adsorption, eq. 4-4, and decomposition of methanol at early potentials, eq. 4-5.^{7, 32, 33}



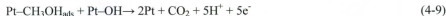
In order to complete the reaction, oxidative removal of the $-\text{CO}_{\text{ads}}$ (representing several possible intermediates such as $-\text{CO}$, $-\text{CHO}$, etc) should take place either at high potentials ($E > +0.6$ V vs. RHE), eq. 4-6, or by means of an oxidizing agent such as a metal oxide (MO), eq. 4-7.³³



Reaction 4-7 is addressed as bifunctional oxidation which requires the presence of an oxidizing agent (MO) in the vicinity of the Pt active sites. Direct oxidation of methanol at Pt occurs during the final stages of the anodic sweep where poison-free sites of Pt are accessible for adsorption of methanol, eq. 4-8.^{7, 32-34}



Pt oxide species formed during the anodic sweep can be reduced during the early stages of the reverse scan, onto which methanol would adsorb (eq. 4-4) and be oxidized rapidly, eq. 4-9.^{7, 32-34}



Typically, the large anodic wave observed during the cathodic scan is known to be due to rapid oxidation of methanol at Pt, reaction 4-9, which necessitates the presence

of unblocked reaction sites. The onset potential for this wave highly depends on the anodic switching potential (the upper potential limit).³² In fact, the oxide layer formed in the final stages of the anodic sweep becomes more stable when using larger upper limits, the reductive removal of which would require more negative potentials so that the methanol oxidation onset will shift to more negative potentials.

Here, similar voltammetric observations were made for the GC/Pt and GC/Ru oxide/Pt electrodes. Close inspection of the forward scans of the electrodes showed lower oxidation onset and substantially larger activity at $E > +0.2$ V for the GC/Ru oxide/Pt electrode. The lower oxidation onset together with the low potential shoulder (at 0.43 V) suggests that the effect of Ru oxide should be mechanistic. It was discussed in an early report¹⁷ that the presence of Ru species caused efficient removal of CO_{ads} and decreased the rate of the adsorption of CO on the reaction sites. Consistently, Ochal *et al.*³⁵ have recently shown that the onset for voltammetric stripping of CO at Ru–Pt core–shell particles was less positive than that at either pure Pt or Ru electrodes. In fact, the CO stripping at the Ru–Pt core–shell alloy gave two overlapping waves, one at ca. +0.55 V/RHE close to the CO stripping potential at pure Ru, and one at +0.8 V/RHE coincidental to the CO stripping potential at the pure Pt. On this basis, we may suggest that the oxidation of methanol at the GC/Ru oxide/Pt electrode has been performed through the well-known bifunctional mechanism. In fact, in our system, dehydrogenation of methanol at Pt occurred at below +0.2/SCE, following which Ru–OH promoted oxidative stripping the CO_{ads} at lower potentials (i.e. than that at Pt–OH) appears as a small shoulder at +0.43 V. However, the increased activity at $+0.5 < E < +0.65$ (CO

stripping at Pt; reaction 4-6) may have been due to improvement (by the Ru oxide layer) in the electronic properties of the Pt nanoparticle. Furthermore, decisive evidence for the presence of the Ru oxide layer was found by inspection of forward scans of the two electrodes at potentials above +0.75 V (figure 4-11) where GC/Ru oxide/Pt was significantly more active than GC/Pt. In this way, a control experiment for the GC/Ru oxide electrode (figure 4-12B) verified that the significant difference between the two forward sweeps at $E > +0.75$ V originated from direct oxidation of methanol at the Ru oxide layer over this region.

4.4. Concluding remarks

We introduced drop coating as a facile and powerful method for the study of the support effects on the oxidation of methanol at Pt nanoparticles. By the aid of this method, we showed that a thin layer of Ru oxide can promote the reaction through a bifunctional mechanism, lowering the oxidation onset and increasing the current density. Here, we adopted the spontaneous deposition method previously described for modification of high surface area carbon black^{18, 19} for modifying glassy carbon electrodes by a thin layer of Ru oxide. Nevertheless, it was also found that the thin polyaniline support had no promotional effects on the reaction suggesting that the previous observations of an effect may have been due to changes in morphology, electronic/ionic transport, and/or distribution of the catalyst species inside the polymeric film.

References

1. T. S. Zhao and C. Xu, in *Encyclopedia of Electrochemical Power Sources*, Elsevier, Amsterdam, 2009, pp. 381-389.
2. X. Zhao, M. Yin, L. Ma, L. Liang, C. Liu, J. Liao, T. Lu and W. Xing, *Energy Environ. Sci.*, 2011, **4**, 2736-2753.
3. A. M. C. Luna, *J. Appl. Electrochem.*, 2000, **30**, 1137-1142.
4. R. W. McCabe and D. F. McCready, *J. Phys. Chem.*, 1986, **90**, 1428-1435.
5. H. A. Gasteiger, N. Markovic, P. N. Ross and E. J. Cairns, *J. Phys. Chem.*, 1993, **97**, 12020-12029.
6. N. M. Markovic, H. A. Gasteiger, P. N. Ross Jr, X. Jiang, I. Villegas and M. J. Weaver, *Electrochim. Acta*, 1995, **40**, 91-98.
7. S. Wasmus and A. Kuever, *J. Electroanal. Chem.*, 1999, **461**, 14-31.
8. A. Kitani, T. Akashi, K. Sugimoto and S. Ito, *Synth. Met.*, 2001, **121**, 1301-1302.
9. T. H. M. Housmans and M. T. M. Koper, *J. Phys. Chem. B*, 2003, **107**, 8557-8567.
10. J. S. Spendelow, J. D. Goodpaster, P. J. A. Kenis and A. Wieckowski, *Langmuir*, 2006, **22**, 10457-10464.
11. C. Yu, F. Jia, Z. Ai and L. Zhang, *Chem. Mater.*, 2007, **19**, 6065-6067.
12. I.-S. Park, K.-S. Lee, Y.-H. Cho, H.-Y. Park and Y.-E. Sung, *Catal. Today*, 2008, **132**, 127-131.
13. P. Justin and G. Ranga Rao, *Int. J. Hydrogen Energy*, 2011, **36**, 5875-5884.

14. H. Laborde, J. M. Leger and C. Lamy, *J. Appl. Electrochem.*, 1994, **24**, 1019-1027.
15. H. Laborde, J. M. Léger and C. Lamy, *J. Appl. Electrochem.*, 1994, **24**, 219-226.
16. J. H. Ma, Y. Y. Feng, J. Yu, D. Zhao, A. J. Wang and B. Q. Xu, *J. Catal.*, 2010, **275**, 34-44.
17. C. T. Hable and M. S. Wrighton, *Langmuir*, 1993, **9**, 3284-3290.
18. X. R. Liu, T. A. Huber, M. C. Kopac and P. G. Pickup, *Electrochim. Acta*, 2009, **54**, 7141-7147.
19. X. Liu and P. G. Pickup, *J. Electrochem. Soc.*, 2010, **158**, A241-A249.
20. B. R. Cuenya, *Thin Solid Films*, 2010, **518**, 3127-3150.
21. P. Diao, D. F. Zhang, M. Guo and Q. Zhang, *J. Catal.*, 2007, **250**, 247-253.
22. F. Mirkhalaf and D. J. Schiffrin, *Langmuir*, 2010, **26**, 14995-15001.
23. J. Yang, J. Y. Lee and H. P. Too, *Anal. Chim. Acta*, 2006, **571**, 206-210.
24. R. B. Moghaddam and P. G. Pickup, *Electrochem. Commun.*, 2011, **13**, 704-706.
25. B. E. Conway and G. Jerkiewicz, *The Electrochemical Society, Pennington, USA (1995), volume of conference proceedings*, 1995, 152-166.
26. A. Essalik, K. Amouzegar and O. Savadogo, *J. Appl. Electrochem.*, 1995, **25**, 404-407.
27. C. L. Green and A. Kucernak, *J. Phys. Chem. B*, 2002, **106**, 1036-1047.
28. W. Schmickler and D. Henderson, *Prog. Surf. Sci.*, 1986, **22**, 323-419.
29. E. Leiva, *Electrochim. Acta*, 1996, **41**, 2185-2206.
30. W. C. Chen, T. C. Wen and A. Gopalan, *Synth. Met.*, 2002, **128**, 179-189.

31. H. Gharibi, K. Kakaei and M. Zhiani, *J. Phys. Chem. C*, **114**, 5233-5240.
32. J. Jiang and A. Kucernak, *J. Electroanal. Chem.*, 2005, **576**, 223-236.
33. C. Roth, A. J. Papworth, I. Hussain, R. J. Nichols and D. J. Schiffrin, *J. Electroanal. Chem.*, 2005, **581**, 79-85.
34. D. Cao, G. Q. Lu, A. Wieckowski, S. A. Wasileski and M. Neurock, *J. Phys. Chem. B*, 2005, **109**, 11622-11633.
35. P. Ochal, J. L. Gomez de la Fuente, M. Tsytkin, F. Seland, S. Sunde, N. Muthuswamy, M. Ronning, D. Chen, S. Garcia, S. Alayoglu and B. Eichhorn, *J. Electroanal. Chem.*, 2011, **655**, 140-146.

Chapter 5

**Support effects on the oxidation of
formic acid at Pd nanoparticles**

Chapter 5. Support effects on the oxidation of formic acid at Pd nanoparticles

This work has been published in part as *Moghaddam, R.B. and Pickup, P.G., Support effects on the oxidation of formic acid at Pd nanoparticles, Electroanalysis 2011, 2, 159-162.* The text was written in part by Dr. Peter Pickup.

5.1. Introduction

Owing to their large electromotive force, high degree of safety, and superior performance, formic acid fuel cells (DFAFCs) have become a potential alternative to H₂-fed PEMFCs and direct methanol fuel cells (DMFCs).¹ Consequently, a large body of research has been increasingly focussed on the study of formic acid (FA) oxidation which is the performance limiting anodic reaction in DFAFCs.¹⁻⁶ The study of FA oxidation has been dominated by development of catalysts with high activity and stability. In this regard, use of Pd and Pt has gained increasing attention as they exhibit superior activities to other catalysts for FA oxidation.¹ As such, there are a significant number of reports on improving the performance of Pt.^{1, 7-9} In contrast, Pd possesses substantial intrinsic activity in the oxidation of FA, making it the dominant catalyst for use in DFAFC anodes.¹ As a matter of fact, Pt is well-known to perform FA oxidation through an indirect pathway in distinct contrast to Pd which promotes the direct oxidation of FA. The indirect mechanism consists of a preliminary decomposition of FA to intermediates such as CO, which can detrimentally deactivate the catalyst.¹ Here, the oxidation of FA at Pt gives two anodic peaks, one weak signal at low potentials (below +0.4 V vs. RHE) due to the direct oxidation of FA, and a second strong oxidation peak at higher potentials

(above +0.6 V vs. RHE) which depicts oxidative removal of CO.¹⁰⁻¹³ The strength of the signal attributed to the oxidative removal of CO reveals the prevalence of the indirect pathway for FA oxidation at Pt. On the contrary, FA oxidation at Pd is characterized by a single anodic peak demonstrating complete oxidation of FA to CO₂, which typically initiates at low potentials (below +0.1 V vs. RHE).¹⁴⁻¹⁶ In fact, efficient oxidation (direct pathway) of FA at Pd at low potentials is the basis for the remarkable activity of this catalyst at operational potentials for DFAFC anodes ($E < +0.4$ V vs. RHE). Even so, there has been considerable interest in increasing the activity of this reaction at Pd. However, stability of the activity of Pd in FA oxidation is somewhat limited; therefore, efforts have been made also to increase the long term activities of such a catalyst. It has been repeatedly shown that alloying Pd with metals such as Pb,^{17, 18} Sb,¹⁹ and Pt²⁰⁻²² could improve its long term activity for FA oxidation.

On the other hand, in consideration of their excellent ionic/electronic properties, controllable morphology, ease of preparation, and ability to provide large surface area networks, conducting polymers (CPs) such as polyaniline (PANI) have been extensively used as additive materials to Pd^{6, 23-26} and shown to markedly promote the oxidation of FA. Specifically, it has been reported that use of PANI as a support material not only could provide a high surface area platform for dispersion of the catalyst species (i.e. increase of electrochemical accessibility)^{6, 26} but it also could impart synergetic effects to the reaction at Pd.²⁶ However, even though several reports can be found in the literature demonstrating the promotional effects of PANI on FA oxidation at Pd,²⁷ there is a lack of clear studies of the pure synergetic influence of such support materials. Hence, it would

be an asset to design a catalytic system in which the support and catalyst are in direct electronic contact while not being physically combined. In fact, fabrication of such a layered structure is useful since it should satisfy the need for adequate electronic communication between the support material and the catalyst species (e.g. Pd), and simultaneously hinder formation of mixed structures (e.g. alloyed or composite structures).

For this purpose, we extended the drop coating method recently developed for the oxidation of methanol at Pt nanoparticles²⁸ to the present work, the oxidation of FA at Pd nanoparticles. The present study is aimed at investigating effects of PANI supports on the oxidation of formic acid at Pd nanoparticles, whether synergetic or electronic, by means of drop coating a solution of preformed Pd nanoparticles on thin layers of PANI deposited on glassy carbon electrodes. In this respect, we used galvanostatic polymerization to deposit a controlled amount of PANI on glassy carbon electrodes in the presence of various acids (H_2SO_4 , CF_3COOH , and CF_3SO_3H). By using cyclic voltammetry and chronoamperometry, FA oxidation was explored on the unmodified and PANI modified electrodes following drop coating with Pd nanoparticles. The recently developed drop coating method, encompassing the use of a preformed nanoparticles solution,²⁸ allows direct analogy between performances of unmodified GC and PANI-modified GC supports in the oxidation of FA at Pd.

5.2. Experimental

5.2.1. Chemicals

Sulfuric acid (Fisher Scientific), formic acid (Sigma-Aldrich, ACS reagent grade), trifluoroacetic acid (Sigma Aldrich), trifluoromethanesulfonic acid (Sigma Aldrich), palladium nitrate (Alfa Aesar), sodium citrate (Anachemia), sodium borohydride (Sigma Aldrich), and Nafion™ solution (5%; Dupont) were used as received. Aniline (Sigma Aldrich) was passed through a dry alumina column prior to use. Doubly distilled water was used throughout the experiments. All measurements were recorded under a nitrogen atmosphere following purging for 15 min.

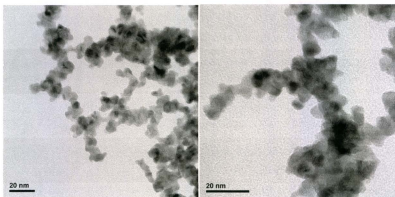


Figure 5-1. Transmission electron microscopy images for Pd nanoparticles coated on a Cu grid.

5.2.2. Synthesis of Pd nanoparticles

$\text{NaBH}_4(\text{aq})$ (1.5 mL; 60 mM) was added dropwise to a stirred solution of $\text{Pd}(\text{NO}_3)_2(\text{aq})$ (10 mL; 3 mM) containing 0.6 mL of 50 mM sodium citrate. The mixture was stirred for a further 2 h and then the grey colloidal Pd nanoparticle solution was stored in a fridge. X-ray diffraction measurements indicated that the average particle diameter was 6.4 ± 0.4 nm. This result is consistent with the particle sizes (5.0 ± 1.3 nm) seen by transmission electron microscopy, figure 5-1, which also confirmed the narrow size distribution previously reported for this synthesis method. This stock solution was diluted by a factor of 10 prior to use with water and Nafion solution to give $26 \mu\text{g mL}^{-1}$ Pd and $1.3 \mu\text{g mL}^{-1}$ Nafion.

5.2.3. Preparation of working electrodes

Glassy carbon electrodes (GC; CH Instruments; 0.071 cm^2) were polished with $0.05 \mu\text{m}$ alumina and rinsed well with water before use. Galvanostatic polymerization ($I = 3.5 \mu\text{A}$, $t = 150$ s) of 0.1 M aniline (purified on a dry alumina column) in 0.5 M H_2SO_4 , 0.5 M CF_3COOH , or 0.5 M $\text{CF}_3\text{SO}_3\text{H}$ was performed to prepare GC/PANI- SO_4 , GC/PANI- CF_3COOH , and GC/PANI- $\text{CF}_3\text{SO}_3\text{H}$ electrodes, respectively. The GC and GC/PANI electrodes were then drop coated with $12.5 \mu\text{L}$ of the diluted Nafion-containing Pd colloid solution to obtain GC/Pd, GC/PANI- SO_4 /Pd, GC/PANI- CF_3COOH /Pd, and GC/PANI- $\text{CF}_3\text{SO}_3\text{H}$ /Pd electrodes with Pd loadings of 3.9×10^{-7} g (ca. $5.4 \mu\text{g cm}^{-2}$) with 5% Nafion by mass relative to Pd. Since this loading of Pd would

correspond to only 150% of a closely packed monolayer of Pd nanoparticles, a high fraction should have been in direct contact with the GC or GC/PANI electrodes.

5.2.4. Instrumentation

An EG&G Model 273A Potentiostat/Galvanostat run by a PC through M270 commercial software was used for voltammetric measurements. A saturated calomel electrode (SCE) and a platinum wire formed the reference and counter electrodes, respectively.

A Model FEI Quanta 400 environmental SEM was used to perform scanning electron microscopy (SEM) measurements. For transmission electron microscopy (TEM), the colloidal Pt nanoparticle solution was diluted with ethanol and sonicated for some minutes. A drop of the mixture was then placed on a 200 mesh copper grid with a carbon support film. The grid was allowed to dry overnight and then observed under a Model JEOL 2011 transmission electron microscope (The Microscopy and Microanalysis Facility, University of New Brunswick). Atomic force microscopy (AFM) measurements were conducted with a Quesant Q-Scope 350 using a smooth glassy carbon plate (SPI Supplies, USA) as the substrate.

5.3. Results and discussion

5.3.1. Characterization of the Pd nanoparticles

Figure 5-2 shows representative SEM images of a GC plate coated with 3.9×10^{-7} g of Pd nanoparticles with 5% Nafion by mass following washing with deionized water to

remove residual salts from the synthesis solution. The view of the complete spot, figure 5-2A, shows that the Pd nanoparticles tend to concentrate in the centre of the GC disk resulting in an uneven distribution of the Pd+Nafion composite. This could originate from the hydrophilic nature of the nanoparticles which is incompatible with the hydrophobic GC substrate. Figure 5-2B displays a selected region (with a high concentration of Pd+Nafion composite) to illustrate the morphology of the composites on the GC electrode. It should be pointed out that control drop coating in the absence of Nafion did not change the distribution significantly.

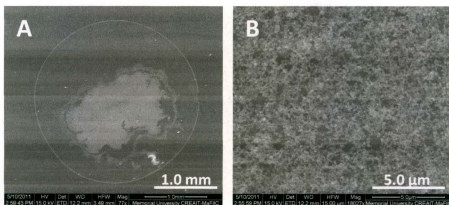


Figure 5-2. SEM images of a GC plate coated with ca. $5.4 \mu\text{g cm}^{-2}$ of Pd nanoparticles + Nafion.

The distribution of the Pd nanoparticles on the GC substrate can be better visualized by means of the atomic force microscopy (AFM) image shown in figure 5-3

(taken from the high concentration area). It can be observed that there are areas with low coverage of the Pd+Nafion composite whereas some other regions have high concentrations of aggregates. The thickness of Pd+Nafion composite in this high concentration area was ca. 40 nm average height (range of 0-94 nm) which would correspond to a total average of ca. 15 nm taking into account the ca. 60% bare region. The Pd mass of 3.9×10^{-7} g would correspond to a total volume of ca. 3.2×10^{-8} cm³ (Pd density = 12.02 g cm⁻³). This volume contains ca. 2.34×10^{11} nanoparticles of 6.4 nm diameter. Taking the Pd particle size 6.4 nm (cross sectional area of $\sim 3.22 \times 10^{-13}$ cm²), and assuming 30% empty area to compensate for the spaces between closely packed nanoparticles on the surface of a GC electrode (area for GC = 0.071 cm²), the mass of 3.9×10^{-7} g will form a coverage with a thickness of ca. 10 nm. Also, having 5% Nafion (w%) content produces a volume of ca. 1.97×10^{-8} cm³ (Nafion density ~ 0.874 g cm⁻³), which forms a layer of ca. 2.7 nm on a 0.071 cm² GC. Hence, one may obtain a total thickness of about 12.7 nm which is equivalent to ca. 150% of a layer of Pd+Nafion composite deposited on the GC electrode.

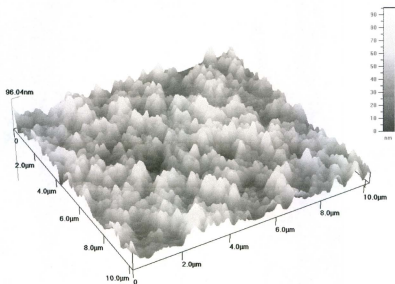


Figure 5-3. AFM (B; $10 \times 10 \mu\text{m} \times 94 \text{ nm}$) images of ca. $5.4 \mu\text{g cm}^{-2}$ of Pd nanoparticles + Nafion on GC.

Figure 5-4 shows the voltammetric response of a GC/Pd electrode ($5.4 \mu\text{g cm}^{-2}$ of Pd nanoparticles) in $0.1 \text{ M H}_2\text{SO}_4$ at a potential sweep rate of 10 mV s^{-1} . Typical for metals such as Pd, the cathodic tail of the voltammogram ($E < 0 \text{ V}$) is dominated by well-defined H adsorption/desorption peaks, which in concert with the H_2 evolution/oxidation current spike at $E < -0.23 \text{ V}$ are indicative of hydrogen electrochemistry at active Pd (0) species. The anodic leg of the CV consisted of oxide formation above $E \sim +0.3 \text{ V}$ which became more pronounced in the final stages of the sweep ($E > +0.6 \text{ V}$). Furthermore, it can be observed that the oxide formation during the anodic scan was followed by a sharp reduction peak in the reverse sweep (at about $+0.42 \text{ V}$) ascribed to oxide stripping.

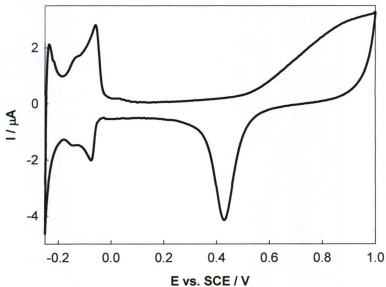


Figure 5-4. Cyclic voltammograms (10 mV s^{-1}) in $0.1 \text{ M H}_2\text{SO}_4$ of a GC electrode coated with ca. $5.4 \mu\text{g cm}^{-2}$ of Pd nanoparticles.

As explained in section 4.3.1, $H_{\text{ads,des}}$ signals of a few metals including Pd can be used to estimate electrochemical active surface area (EASA). Here we use the H_{ads} region (cathodic scan; 0 to -0.15 V) to obtain EASA for Pd ($EASA_{\text{Pd}}$). Background corrected integration of the peak area for the H_{ads} twin signals gives a ca. 0.06 cm^2 active area which would correspond to a utilization value of ca. 20% taking into account a theoretical active area of ca. 0.30 cm^2 for Pd (The geometric area of the Pd particles, estimated from

the mean particles size and mass of Pd applied to the electrode, was ca. 0.30 cm^2). The limited utilization value obtained from the H_{ads} area can be correlated with the uneven distribution of the Pd+Nafion aggregates (see figures 5-2 and 5-3) which would have caused a significant portion of the Pd nanoparticles establishing weak electronic contact with the electrode surface.

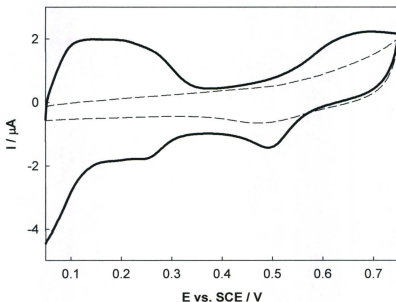


Figure 5-5. Cyclic voltammogram (10 mV s^{-1}) of a GC/Pd electrode in $0.1 \text{ M H}_2\text{SO}_4$ in the presence (solid line) and absence (dashed line) of 0.005 M CuSO_4 .

However, this was further explored by Cu underpotential deposition (Cu UPD) and stripping following the protocol described by Green and Kucernak for Pt

electrodes.²⁹ Figure 5-5 presents CVs of a GC/Pd electrode in the absence and presence of 0.005 M CuSO₄ in 0.1 M H₂SO₄.

Here based on the Cu UPD protocol,²⁹ the electrode was conditioned at +0.75 V for 120 s, and then stepped to +0.05 V for 100 s to deposit approximately a monolayer of Cu. Thereafter, a single cycle CV was conducted in the range of 0.05 to 0.75 V with Cu stripping between 0.05 and 0.4 V on the anodic sweep. The electrochemically active Pd area (EASA_{Pd}) of the electrode can be estimated from the charge (Q) under the anodic portion of the curve between 0.05 and 0.4 V, corrected for the background contribution in the absence of Cu (dashed line in figure 5-5), according to eq. 5-1.³⁰

$$EASA_{Pd} = Q_{Cu\ UPD} / (4.07 \times 10^{-4} \text{ C cm}^{-2}) \quad (5-1)$$

The estimated EASA_{Pd} for the GC/Pd based on the Cu UPD results was ca. 0.11 cm² corresponding to about 35% utilization.

Figure 5-6 presents overlaid cyclic voltammograms of a GC electrode and three types of GC/PANI electrode coated with 5.4 μg cm⁻² Pd nanoparticles in 0.1 M H₂SO₄. The anodic limit was restricted to +0.4 V in order to avoid oxidative degradation (overoxidation) of the PANI films at higher potentials. The larger background currents along with the oxidation and reduction peaks above 0 V indicate the presence of PANI in all of the GC/PANI/Pd electrodes.

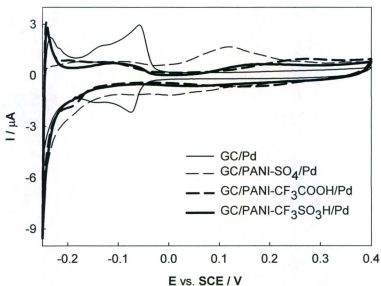


Figure 5-6. Cyclic voltammograms (10 mV s^{-1}) in $0.1 \text{ M H}_2\text{SO}_4$ of GC, GC/PANI- $\text{CF}_3\text{SO}_3\text{H}$, GC/PANI- SO_4 , and GC/PANI- CF_3COOH electrodes coated with ca. $5.4 \mu\text{g cm}^{-2}$ of Pd nanoparticles.

The hydrogen electrochemistry at the GC/PANI/Pd electrodes was appreciably weaker than that at the GC/Pd electrode, providing evidence for inhibitory effects of the PANI layers on $H_{\text{ads}}/H_{\text{des}}$ at the Pd nanoparticles. The $EASA_{\text{Pd}}$ of the GC/PANI/Pd electrodes based on the charge under the H_{ads} waves was less than 50% of that for the GC/Pd electrode, and corresponded to less than 10% utilization of the Pd nanoparticles. Consequently, the Cu UPD methodology described earlier was used to investigate the reliability of these values.

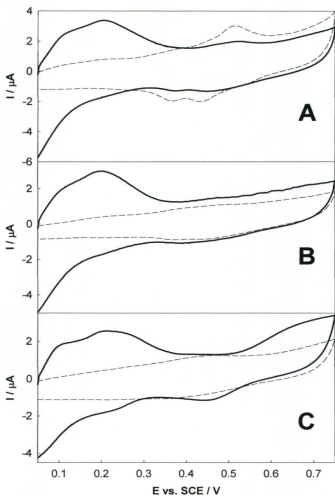


Figure 5-7. Cyclic voltammograms (10 mV s^{-1}) of GC/PANI-SO₄/Pd (A) GC/PANI-CF₃SO₃H (B), and GC/PANI-CF₃COOH (C) electrodes in 0.1 M H₂SO₄ in the presence (solid line) and absence (dashed line) of 0.005 M CuSO₄.

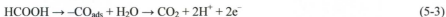
Figure 5-7A-C presents cyclic voltammograms for each of the three GC/PANI/Pd electrodes in the absence and presence of 0.005 M CuSO₄ in 0.1 M H₂SO₄. General characteristics of the CVs were similar to those for the GC/Pd electrode (except for the somewhat larger background) with Cu stripping waves appearing in the anodic portion of the curves between +0.05 and +0.4 V. By integrating the anodic sweeps of the Cu stripping CVs between +0.05 and +0.4 V corrected for the background contribution in the absence of Cu(II), the EASA_{Pd} values for the GC GC/PANI-SO₄/Pd, GC/PANI-CF₃COOH/Pd, and GC/PANI-CF₃SO₃H/Pd electrodes were ca. 0.15, 0.12, and 0.13 cm², respectively. These values represent utilizations (EASA/geometric area) ranging from ca. 40 to 50% for the GC/PANI/Pd electrodes.

It was shown that the utilization values obtained by either of the methods (H_{ads} signals or the Cu UPD protocol) did not exceed 50% for any of the four electrodes. This could originate from clumping of the Pd+Nafion aggregates (SEM and AFM images; figures 5-2 and 5-3) giving rise to 50–65% of the Pd particles not establishing electronic contact with the substrate. However, the electrochemical active area by the Cu UPD procedure gave quite similar results for all the electrodes, in contrast to the different values given by the H_{ads} signals. This clearly suggests that the PANI supports exert an inhibitory impact on the hydrogen electrochemistry at the Pd nanoparticles whereas underpotential deposition of Cu(0) was not affected. This further indicates that general electronic/ionic transport characteristics of the Pd species (i.e. accessibility) were not markedly altered by nature of the supports. However, the Cu UPD results showed somewhat larger utilization values for the GC/PANI/Pd electrodes than that for GC/Pd.

5.3.2. Formic acid oxidation at Pd nanoparticles

Figure 5-8 shows voltammetric oxidation of FA at the GC/Pd and GC/PANI/Pd electrodes. All the CVs typically consist of a large oxidation peak in the forward sweep demonstrating direct oxidation of FA. Interestingly, FA oxidation continued during the backward sweep characterized by a large anodic signal. However, the oxidation current on the cathodic scan could also be in part due to anion adsorption.^{31,32}

Nevertheless, no significant voltammetric feature was seen beyond $E = +0.4$ V when the upper potential was set at +1 V (not shown), so the upper limit was set at +0.4 V in order to prevent possible oxidative degradation of the PANI. On the basis of previous reports on FA oxidation at Pd, the anodic peak should be ascribed to a one-step oxidation of FA at all these electrodes which follows the direct oxidation pathway, eq. 5-2, as opposed to the indirect pathway, eq. 5-3.^{1,33}



However, figure 5-8 clearly shows that all three GC/PANI/Pd electrodes were considerably superior to the GC/Pd electrode in the entire voltammetric range for both the forward and backward scans. Here, the GC/PANI-SO₄/Pd electrode gave the largest current for FA oxidation (slightly better than GC/PANI-CF₃SO₃H/Pd) while GC/PANI-CF₃COOH/Pd displayed the lowest activity of the GC/PANI/Pd electrodes. Furthermore, less positive oxidation onsets (by 50-70 mV) can be detected for the GC/PANI/Pd electrodes (compared to the GC/Pd electrode), which together with their larger limiting

currents elucidate significance of the PANI supports in promoting the reaction at the Pd nanoparticles.

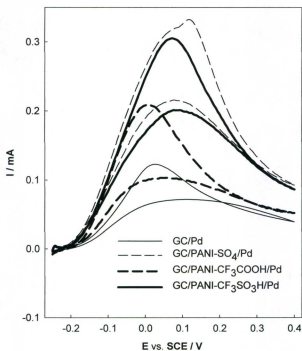


Figure 5-8. Cyclic voltammograms (10 mV s^{-1}) in $0.1 \text{ M H}_2\text{SO}_4 + 0.5 \text{ M FA}$ of GC, GC/PANI-CF₃SO₃H, GC/PANI-SO₄, and GC/PANI-CF₃COOH electrodes coated with ca. $5.4 \mu\text{g cm}^{-2}$ of Pd nanoparticles.

Comparison of the catalytic utilization of the GC/Pd electrode with any of the three GC/PANI/Pd electrodes cannot account for the different FA oxidation activities recorded for these electrodes. In fact, the GC/Pd electrode exhibited larger hydrogen

signals than all the GC/PANI/Pd electrodes whereas it showed considerably lower activity for FA oxidation. As well, the Cu UPD stripping area for the GC/Pd electrode was only slightly lower than that for the GC/PANI/Pd electrodes which also could not explain its lower FA oxidation activity. Therefore, it is suggested that various types of PANI, regardless of their dopant types, had synergetic effects on the oxidation of FA at the Pd nanoparticles. Even so, it is reasonably expected that the presence of such a support material could improve the ionic/electronic properties of the carbon substrate although no explicit evidence was found for such effects.

Further evidence for superiority of the GC/PANI supports to GC was provided by constant potential oxidation of FA at Pd nanoparticles supported on these electrodes. Figure 5-9 presents chronoamperometry of the GC/Pd, GC/PANI-SO₄/Pd, GC/PANI-CF₃COOH/Pd, and GC/PANI-CF₃SO₃H/Pd electrodes at -0.1 V in the presence of 0.5 M FA. Consistent with the voltammetric results, all three GC/PANI/Pd electrodes exhibited markedly larger currents than the GC/Pd electrode, with their activities increasing in the order PANI-CF₃COOH < PANI-CF₃SO₃H < PANI-SO₄. Here, the three GC/PANI/Pd electrodes developed similar patterns with insignificant differences in activities, and followed the trend observed in their comparative voltammetric profiles (see figure 5-8). The GC/PANI-CF₃COOH/Pd electrode showed a larger initial current than GC/PANI-CF₃SO₃H/Pd, but its current decayed more rapidly with time. In contrast, the GC/PANI-SO₄/Pd electrode showed the highest initial current and least rate of decay. We may summarize the stability of the activities of the GC/PANI/Pd electrodes at -0.1 V as increasing in the order PANI-CF₃COOH < PANI-CF₃SO₃H ≈ PANI-SO₄.

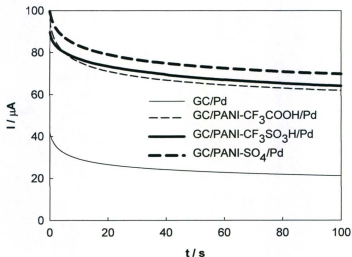


Figure 5-9. Chronoamperometry at -0.1 V for GC/Pd, GC/PANI-CF₃COOH/Pd, GC/PANI-CF₃SO₃H/Pd, and GC/PANI-SO₄/Pd electrodes in 0.1 M H₂SO₄ containing 0.5 M FA.

Chronoamperometric oxidation of FA at the GC/Pd, GC/PANI-CF₃COOH/Pd, GC/PANI-CF₃SO₃H/Pd, and GC/PANI-SO₄/Pd electrodes at 0 V is presented in figure 5-10. Similar to the CAs at -0.1 V, all three PANI-supported electrodes were significantly superior to the GC/Pd electrode. However, there are interesting differences between this set of CAs at 0 V and their counterparts at -0.1 V. While all three electrodes displayed similar initial activities at 0 V, the GC/PANI-CF₃SO₃H/Pd electrode gave the highest stability whereas the current density at the GC/PANI-CF₃COOH/Pd electrode decayed most rapidly over the 100 s timescale.

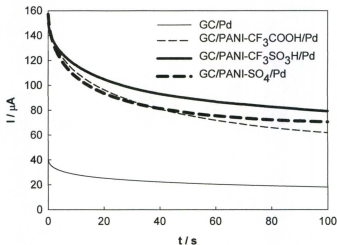


Figure 5-10. Chronoamperometry at 0 V for GC/Pd, GC/PANI-CF₃COOH/Pd, GC/PANI-CF₃SO₃H/Pd, and GC/PANI-SO₄/Pd electrodes in 0.1 M H₂SO₄ containing 0.5 M FA.

Chronoamperometry of the GC/Pd, GC/PANI-CF₃COOH/Pd, GC/PANI-CF₃SO₃H/Pd, and GC/PANI-SO₄/Pd electrodes in the presence of 0.5 M FA at +0.1 V is displayed in figure 5-11. Here, comparative CAs at +0.1 V further showed unambiguous superiority of all GC/PANI/Pd electrodes to the GC/Pd electrode. Moreover, comparison of the three PANI-supported electrodes provided further evidence for higher activity of GC/PANI-CF₃SO₃H/Pd. In fact, the GC/PANI-CF₃SO₃H/Pd, and GC/PANI-SO₄/Pd electrodes both exhibited initial currents of ca. 85 μA, but GC/PANI-SO₄/Pd underwent a more rapid decay pattern resulting in 45 μA at t = 100 s while that for the GC/PANI-SO₄/Pd electrode was 55 μA at t = 100 s. However, consistent with the voltammetric

results, both GC/PANI-CF₃SO₃H/Pd, and GC/PANI-SO₄/Pd were superior to the GC/PANI-CF₃COOH/Pd electrode with appreciably lower initial activity and a current of only 32 μ A at $t = 100$ s. It is obvious that the CAs at this potential typically show lower currents compared to those at 0 V (chronoamperometry was performed sequentially at -0.1, 0, and +0.1 V), presumably due to the deactivation at earlier potentials. In fact, while CAs for fresh electrodes at +0.1 V (not presented) produced the same trend as shown in figure 5-11, they exhibited larger activities than either of the CAs in figures 5-10 and 5-11.

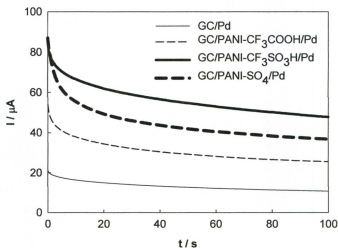


Figure 5-11. Chronoamperometry at +0.1 V for GC/Pd, GC/PANI-CF₃COOH/Pd, GC/PANI-CF₃SO₃H/Pd, and GC/PANI-SO₄/Pd electrodes in 0.1 M H₂SO₄ containing 0.5 M FA.

The comparative decay patterns for all three electrodes at various potentials can be more clearly visualized by normalizing with respect to their corresponding initial activities of 1. Figure 5-12 displays overlaid normalized chronoamperometric profiles of the GC/Pd, GC/PANI-CF₃COOH/Pd, GC/PANI-CF₃SO₃H/Pd, and GC/PANI-SO₄/Pd electrodes at -0.1 V.

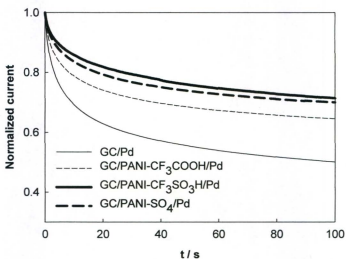


Figure 5-12. Normalized Chronoamperometric profiles at -0.1 V for GC/Pd, GC/PANI-CF₃COOH/Pd, GC/PANI-CF₃SO₃H/Pd, and GC/PANI-SO₄/Pd electrodes in 0.1 M H₂SO₄ containing 0.5 M FA.

Taking the CAs at -0.1 V, one may notice that all of the GC/PANI/Pd electrodes showed more stable long term activities compared to GC/Pd. Here their long term performance patterns roughly follow the trend seen for their comparative activities (see

figure 5-9) except for the GC/PANI-CF₃SO₃H/Pd electrode which gave more stable long term pattern than GC/PANI-SO₄/Pd. Interestingly, the GC/PANI-CF₃SO₃H/Pd electrode gave more stable long term activities than the other GC/PANI/Pd electrodes at all potentials. This may be attributed to the effect of the counter ions used for the polymerization (e.g. PANI with superior electronic/ionic properties) and/or directly to the electrochemical performances of the PANI/Pd composites. At 0 V, figure 5-13, all four electrodes showed similar long term patterns although GC/PANI-CF₃SO₃H/Pd was slightly superior.

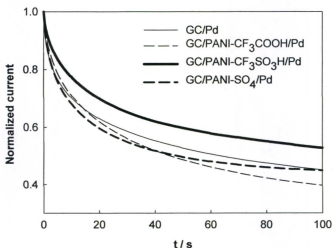


Figure 5-13. Normalized Chronoamperometric profiles at 0 V for GC/Pd, GC/PANI-CF₃COOH/Pd, GC/PANI-CF₃SO₃H/Pd, and GC/PANI-SO₄/Pd electrodes in 0.1 M H₂SO₄ containing 0.5 M FA.

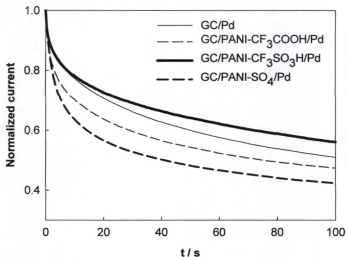


Figure 5-14. Normalized Chronoamperometric profiles at +0.1 V for GC/Pd, GC/PANI-CF₃COOH/Pd, GC/PANI-CF₃SO₃H/Pd, and GC/PANI-SO₄/Pd electrodes in 0.1 M H₂SO₄ containing 0.5 M FA.

Comparison of the long term patterns at +0.1 V (figure 5-14) again indicates better long term performance of the GC/PANI-CF₃SO₃H/Pd electrode; it is noteworthy that the GC/Pd electrode produced a moderately more stable pattern than GC/PANI-CF₃COOH/Pd and GC/PANI-SO₄/Pd. Nevertheless, while repeated experiments (not shown) confirmed the validity of the observed trends, the differences in the long term activities (see figure 5-12), particularly at 0 and +0.1 V, were not sufficiently great to provide a clear explanation of an effect. However, the chronoamperometric profiles in figure 5-12 strongly suggest that the PANI prepared in CF₃SO₃H was a better support,

giving high activity and the best long term stability for FA oxidation at the Pd nanoparticles.

5.3.3. Mechanistic insights

It was discussed in chapter 1 (section 1.1.2.3) that the oxidation of FA can proceed through two pathways; direct (equation 5-2) and indirect pathways (equation 5-3). Furthermore, it was discussed that FA oxidation at Pd essentially follows the direct pathway, which favours complete oxidation of FA. However, as suggested by Liao *et al.*²⁶, the significant increases in the activity for the GC/PANI/Pd electrodes compared to GC/Pd could originate from “more oxygen-donating species formation on the surface area of Pd catalysts” resulting in promotion of FA oxidation. However, they did not provide conclusive evidence for the presence/formation of such oxygen-donating groups. In an early report by Podlovchenco and coworkers,³⁴ it was shown that the effect of PANI was more pronounced on Pd compared to Pt in FA oxidation. Therein, the authors did not clearly address the origin of this promotion, although they suggested that the effect could be due to interaction between Pd and the polymer matrix, facilitated diffusion of formate as counter anion for the protonated $-NH-$ groups (i.e. $-NH_2^+$), or provision of “new active sites for the current-determining reaction of the HCOOH electro-oxidation process”. Moreover, in an attempt to investigate the mechanism of FA oxidation, they employed Tafel plots, which showed that FA oxidation at the pure Pd and PANI-supported Pd electrodes followed the direct pathway (see section 1.1.2.3). On the other hand, Antolini *et al.*²⁷ reviewed several reports on “polymer supports for low-temperature

fuel cell catalysts". In this review, there are a number of papers³⁵⁻³⁷ that ascribe the promotional effects of polyaniline to its ability to provide highly conductive catalyst supports, which can also prevent formation/strong adsorption of the poisoning species (e.g. CO) during the oxidation of organic fuels at either Pd or Pt.

Nevertheless, the actual role of polyaniline as additive material (e.g. as support) to Pd in FA oxidation is still elusive. In this regard, more focussed work is required not only to unveil the interaction between polyaniline and Pd in this reaction, but also to help development of more active catalysts based on conducting polymers such polyaniline for FA oxidation.

5.4. Concluding remarks

By means of cyclic voltammetry and chronoamperometry we explicitly elucidated synergetic effects of PANI supports prepared in the presence of various dopants for FA oxidation at Pd nanoparticles. We employed a drop coating method to load various supports, GC and PANI-modified GC electrodes, with Pd nanoparticles. The use of a preformed Pd nanoparticle solution, along with preparing thin layers of various PANI supports (under slow galvanostatic polymerization condition) allowed direct analogy between various supports in FA oxidation at Pd without observably altering of the structure and morphology of either the support or Pd nanoparticles. It was also shown that all of the GC/PANI/Pd electrodes provided higher FA oxidation currents than the GC/Pd, with the activity increasing in the order PANI-CF₃COOH < PANI-CF₃SO₃H < PANI-SO₄. As a matter of fact, the PANI influenced both the onset of FA oxidation and

the peak current. Therefore, it can be seen that not only does the presence of a thin layer of PANI impart synergetic effects to the oxidation of FA at Pd nanoparticles, but it was also revealed that nature of the dopant played a key role in the activity of the resulting electrodes. A study of the effects of various dopants with different functional groups on the oxidation of FA at Pd nanoparticles could form basins for a sophisticated future work, the fundamentals of which are currently under investigation in our group.

References

1. X. Yu and P. G. Pickup, *J. Power Sources*, 2008, **182**, 124-132.
2. V. E. Kazarinov, V. N. Andreev, M. A. Spitsyn and A. P. Mayorov, *Electrochim. Acta*, 1990, **35**, 1459-1463.
3. M. Weber, J. T. Wang, S. Wasmus and R. F. Savinell, *J. Electrochem. Soc.*, 1996, **143**, L158-L160.
4. S. Ha, R. Larsen and R. I. Masel, *J. Power Sources*, 2005, **144**, 28-34.
5. T. Cheng and E. Gyenge, *J. Appl. Electrochem.*, 2009, **39**, 1925-1938.
6. R. K. Pandey and V. Lakshminarayanan, *J. Phys. Chem. C*, 2009, **113**, 21596-21603.
7. X. Yu and P. G. Pickup, *Electrochim. Acta*, 2010, **55**, 7354-7361.
8. X. Yu and P. G. Pickup, *Electrochim. Acta*, 2011, **56**, 4037-4043.
9. X. Yu and P. G. Pickup, *J. Power Sources*, 2011, **196**, 7951-7956.
10. H. Kita and H.-W. Lei, *J. Electroanal. Chem.*, 1995, **388**, 167-177.
11. W. Liu and J. Huang, *J. Power Sources*, 2009, **189**, 1012-1015.
12. Y. Chen, Y. Zhou, Y. Tang and T. Lu, *J. Power Sources*, 2010, **195**, 4129-4134.
13. W. Zhou, J. Xu, Y. Du and P. Yang, *Int. J. Hydrogen Energy*, 2011, **36**, 1903-1912.
14. R. Wang, S. Liao and S. Ji, *J. Power Sources*, 2008, **180**, 205-208.
15. D. Morales-Acosta, J. Ledesma-Garcia, L. A. Godinez, H. G. Rodriguez, L. Alvarez-Contreras and L. G. Arriaga, *J. Power Sources*, 2010, **195**, 461-465.

16. X.-M. Wang, J. Wang, Q.-Q. Zou and Y.-Y. Xia, *Electrochim. Acta*, 2011, **56**, 1646-1651.
17. X. Yu and P. G. Pickup, *J. Power Sources*, 2009, **192**, 279-284.
18. R. Li, H. Hao, W.-B. Cai, T. Huang and A. Yu, *Electrochem. Commun.*, 2010, **12**, 901-904.
19. X. Yu and P. G. Pickup, *Electrochem. Commun.*, 2010, **12**, 800-803.
20. R. S. Jayashree, J. S. Spindelw, J. Yeom, C. Rastogi, M. A. Shannon and P. J. A. Kenis, *Electrochim. Acta*, 2005, **50**, 4674-4682.
21. Q. Yi, W. Huang, X. Liu, G. Xu, Z. Zhou and A. Chen, *J. Electroanal. Chem.*, 2008, **619-620**, 197-205.
22. H. Gao, S. Liao, J. Zeng, Y. Xie and D. Dang, *Electrochim. Acta*, 2011, **56**, 2024-2030.
23. A. Frydrychewicz, A. Czerwinski and K. Jackowska, *Synth. Met.*, 2001, **121**, 1401-1402.
24. V. Andreev, *Russ. J. Electrochem.*, 2006, **42**, 98-101.
25. V. Andreev, *Russ. J. Electrochem.*, 2006, **42**, 193-196.
26. C. Liao, Z. D. Wei, S. G. Chen, L. Li, M. B. Ji, Y. Tan and M. J. Liao, *J. Phys. Chem. C*, 2009, **113**, 5705-5710.
27. E. Antolini and E. R. Gonzalez, *Appl. Catal., A*, 2009, **365**, 1-19.
28. R. B. Moghaddam and P. G. Pickup, *Electrochem. Commun.*, 2011, **13**, 704-706.
29. C. L. Green and A. Kucernak, *J. Phys. Chem. B*, 2002, **106**, 1036-1047.

30. F. Lan-lan, T. Qian, L. Ming-fang, L. Ling-wen, C. Dong and C. Yan-xia, *Chin. J. Chem. Phys.*, 2010, **23**, 543.
31. M. Arenz, V. Stamenkovic, T. J. Schmidt, K. Wandelt, P. N. Ross and N. M. Markovic, *PCCP*, 2003, **5**.
32. X. Yu and P. G. Pickup, *J. Power Sources*, 2009, **187**, 493-499.
33. E. H. J.M. Feliu, in: W. Vielstich, H.A. Gasteiger, A. Lamm (Eds.), *Handbook of Fuel Cells*, Wiley, New York, 2003, **2**, 679.
34. B. Podlovchenko, Y. Maksimov, T. Gladysheva and E. Kolyadko, *Russ. J. Electrochem.*, 2000, **36**, 731-735.
35. P. O. Esteban, J. M. Leger, C. Lamy and E. Genies, *J. Appl. Electrochem.*, 1989, **19**, 462-464.
36. H. Laborde, J. M. Léger and C. Lamy, *J. Appl. Electrochem.*, 1994, **24**, 219-226.
37. H. Laborde, J. M. Léger and C. Lamy, *J. Appl. Electrochem.*, 1994, **24**, 1019-1027.

Chapter 6

**Support effects on the oxidation of
ethanol at Pt nanoparticles**

Chapter 6. Support effects on the oxidation of ethanol at Pt nanoparticles

This work has been published in part as *Moghaddam, R.B. and Pickup P.G., Support effects on the oxidation of ethanol at Pt nanoparticles, Electrochim. Acta, 2012, 65, 210-215*. The text was written in part by Dr. Peter Pickup.

6.1. Introduction

In the development of fuel cell technology, the electrochemical properties of the catalyst layer play a key role in the design of efficient cells.¹⁻⁴ In this regard, making high activity catalysts has long been a focus in this area.¹⁻⁴ Particularly for direct ethanol fuel cells (DEFCs), which form an important class of fuel cells, Pt-based catalysts have been widely considered.^{1, 2, 5} Here, alloying Pt with metals such as Sn⁶⁻⁸ and Ru^{1, 8} has been shown to remarkably promote the oxidation of ethanol at the anode, which is one of the main factors limiting the performance of DEFCs. In fact, even though Pt is the catalyst of choice for this reaction, the oxidation of ethanol at this catalyst has slow kinetics and also can be detrimentally affected by poisoning intermediates.¹ Efforts in this area have been made not only to improve the electronic properties of Pt based catalysts, but also to facilitate the complete oxidation of ethanol, both of which could increase the catalytic efficiency. To achieve these goals, metals such as W, Pd, Rh, Re, Mo, Ti, Ce have also been examined for use in binary materials with Pt,¹ and all of these have shown superior performances to pure Pt, although not exceeding the performances of Ru and Sn-containing Pt alloys.

The key challenge in developing catalysts for ethanol oxidation is to find systems that can efficiently break the C-C bond so that the complete oxidation to CO₂ can occur. This is an important drawback associated with the PtSn and PtSnRu systems in acidic media. In fact, while they are the most active combinations for ethanol oxidation,¹ they promote incomplete oxidation of ethanol leading to production of acetaldehyde and acetic acid, and therefore low CO₂ yields.^{1, 5, 9} Consistently, by means of a differential electrochemical mass spectrometry (DEMS) analysis on various combinations of Pt with Ru and/or Sn, Wang and coworkers¹⁰ showed that the presence of Sn or Ru or both did not increase the CO₂ yield. As a consequence, this will lower fuel efficiencies in DEFCs¹¹ and result in high levels of byproducts that would need to be destroyed or recycled. Nevertheless, this conclusion was challenged by two more recent reports,^{8, 12} suggesting that addition of Sn or Ru to Pt caused a negative shift in the CO oxidation potential, which led to higher yields of CO₂.

On the other hand, even though ethanol oxidation at pure Pt has a slow kinetics, it actually gives the highest yield of CO₂. Ghumann *et al.* reported a 76% CO₂ yield at Pt (at 100 °C), which to date is the highest CO₂ yield for ethanol oxidation at a moderate temperature.⁹ However, as mentioned earlier, the oxidation of ethanol at pure Pt has unfavourable kinetics. Hence efforts have been made to obtain catalysts with high activities and appreciable C-C bond cleavage efficiency. As an example, Kowal *et al.* synthesized a ternary PtRhSnO₂/C catalyst that splits the C-C bond in ethanol at ambient temperature with close to 50% efficiency.¹³

Methods such as decoration, stepwise deposition, and codeposition have been widely used to combine Pt with Sn and Ru to enhance its catalytic activity.^{1,2,14} Another way to improve the performance of Pt is by modifying the catalyst support. Therefore, it is of great value to investigate whether modified supports (*e.g.* Sn oxide on a carbon substrate) can accelerate the reaction through, for example, synergetic effects (*e.g.* bifunctional mechanism) and/or by enhancing electronic/ionic transport properties.

Consequently, we have studied ethanol oxidation at preformed Pt nanoparticles immobilized on various metal oxides supported on carbon, which allows direct comparisons between supports (various metal oxides) without altering the structure, morphology, and chemical properties of the catalyst. We have recently demonstrated that support effects in electrocatalysis can be unambiguously identified and quantitatively compared by applying small quantities of preformed catalyst nanoparticles onto unmodified and modified glassy carbon electrodes.^{15,16} For example, it was shown that a thin layer of Ru oxide on the glassy carbon strongly promoted the oxidation of methanol at Pt, while a layer of polyaniline had mainly inhibitory effects.¹⁶ In the present study, we investigate the oxidation of ethanol at unsupported and metal oxide supported Pt nanoparticles. As for the oxidation of methanol and formic acid in the previous studies, glassy carbon was used as a control support, while indium-tin oxide (ITO) and thin layers of Ru oxide, Sn oxide, and a mixed Ru-Sn oxide on glassy carbon were prepared for comparison.

6.2. Experimental

6.2.1. Chemicals

Sulfuric acid (Fisher Scientific), anhydrous ethanol (Commercial Alcohols Inc.), KRuO_4 (Alfa Aesar), $\text{SnCl}_4 \cdot 5\text{H}_2\text{O}$ (Fisher Scientific), $\text{H}_2\text{PtCl}_6 \cdot 6\text{H}_2\text{O}$ (Alfa Aesar), potassium hydroxide (ACP Chemical Inc.), sodium citrate (Anachemia), sodium borohydride (Sigma Aldrich), and Nafion™ solution (5%; Dupont) were used as received. All measurements were recorded at ambient temperature under a nitrogen atmosphere following purging for 15 min.

6.2.2. Preparation of Pt nanoparticles

$\text{NaBH}_4(\text{aq})$ (1.5 mL; 120 mM) was added dropwise to a stirred solution of 10 mL of 3 mM $\text{H}_2\text{PtCl}_6(\text{aq})$ mixed with 0.6 mL of 50 mM aqueous sodium citrate. Following stirring for a further 2 h, the resulting grey colloidal Pt nanoparticle solution was stored in a fridge. This stock solution was diluted by a factor of 20 prior to use with water and Nafion solution to give $24 \mu\text{g mL}^{-1}$ Pt and $1.2 \mu\text{g mL}^{-1}$ Nafion. X-ray diffraction measurements indicated that the average particle diameter was 5.0 ± 0.4 nm. This was consistent with the narrow size distribution previously reported for this synthesis method (see figure 4-1 for transmission electron micrographs).¹⁷

6.2.3. Working electrode preparation

Glassy carbon electrodes (GC; CH Instruments; 0.071 cm^2) were polished with $0.05 \text{ }\mu\text{m}$ alumina and rinsed well with water before use. Electrodes were coated with a thin film (*ca.* 25 nm) of hydrous Ru oxide (GC/Ru oxide) as previously described. Spontaneous deposition was also used to prepare GC/Sn oxide electrodes, by immersion of preconditioned ($E = -0.5 \text{ V}$, $t = 300 \text{ s}$ in $0.1 \text{ M H}_2\text{SO}_4$) GC electrodes in a neutral aqueous SnCl_4 solution (0.05 M) for 15 min . Spontaneous codeposition was used to prepare GC/ $\text{Ru}_x\text{Sn}_{1-x}$ oxide electrodes, whereby a preconditioned ($E = -0.5 \text{ V}$, $t = 300 \text{ s}$ in $0.1 \text{ M H}_2\text{SO}_4$) GC electrode was placed in $0.05 \text{ M KRuO}_4 + 0.05 \text{ M SnCl}_4$ (in 0.1 M KOH) for 15 min . The GC, InSn oxide (ITO; Donnelly Corp.), GC/Sn oxide and GC/ $\text{Ru}_x\text{Sn}_{1-x}$ oxide/Pt electrodes were then drop coated with $12.5 \text{ }\mu\text{L}$ of the diluted Nafion containing Pt colloid to obtain GC/Pt, ITO/Pt, GC/Ru oxide/Pt, GC/Sn oxide/Pt and GC/ $\text{Ru}_x\text{Sn}_{1-x}$ oxide/Pt electrodes with Pt loadings of $3.0 \times 10^{-7} \text{ g}$ ($4.3 \text{ }\mu\text{g cm}^{-2}$) with 5% Nafion by mass relative to Pt. The GC/Sn oxide/Pt and GC/ $\text{Ru}_x\text{Sn}_{1-x}$ oxide/Pt electrodes were placed in a concentrated mixture of $\text{HCl} + \text{HNO}_3$ (for 3 days) to dissolve the metal contents. The concentration of the resulting solution was determined by using a model EALN DRC II inductively coupled plasma mass spectrometer (ICP-MS; Axial Field Technology), which gave the following results:

GC/Sn oxide/Pt: Sn = $0.33\text{-}0.34 \text{ }\mu\text{g}$, Pt = $0.39 \text{ }\mu\text{g}$.

GC/ $\text{Ru}_x\text{Sn}_{1-x}$ oxide/Pt: Ru = $1.5 \text{ }\mu\text{g}$, Sn = $0.32 \text{ }\mu\text{g}$, Pt = $0.41 \text{ }\mu\text{g}$.

The $\text{Ru}_x\text{Sn}_{1-x}$ oxide composition was therefore $\text{Ru}_{0.85}\text{Sn}_{0.15}$ oxide, and the Pt loadings were close to the targeted value. Based on the densities of SnO_2 and RuO_2 (6.95

g cm^{-3} and 6.97 g cm^{-3} , respectively), the thicknesses of the Sn oxide and $\text{Ru}_{0.85}\text{Sn}_{0.15}$ oxide films can be estimated to have been *ca.* 9 nm and 40 nm, respectively.

6.2.4. Instrumentation

An EG&G Model 273A Potentiostat/Galvanostat run by a PC through M270 commercial software was used for voltammetric and potentiostatic measurements. A saturated calomel electrode (SCE) and a platinum wire formed the reference and counter electrode, respectively.

A Model FEI Quanta 400 environmental SEM was used to perform scanning electron microscopy (SEM) measurements. For transmission electron microscopy (TEM), the colloidal Pt nanoparticle solution was diluted with ethanol and sonicated for some minutes. A drop of the mixture was then placed on a 200 mesh copper grid with a carbon support film. The grid was allowed to dry overnight and then observed under a Model JEOL 2011 transmission electron microscope (The Microscopy and Microanalysis Facility, University of New Brunswick). Atomic force microscopy (AFM) measurements were conducted with a Quesant Q-Scope 350 using a smooth glassy carbon plate (SPI Supplies, USA) as the substrate.

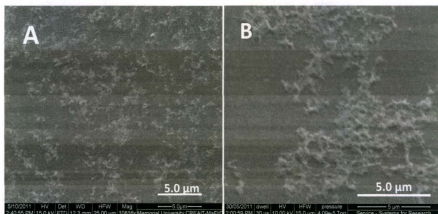


Figure 6-1. SEM image of *ca.* $4.3 \mu\text{g cm}^{-2}$ of Pt nanoparticles + Nafion on GC (A) and ITO (B) plates.

6.3. Results and discussion

6.3.1. Characterization of the nanoparticles and electrodes

Representative scanning electron microscopy images of *ca.* $4.3 \mu\text{g cm}^{-2}$ of Pt nanoparticles drop coated on GC and an ITO plates are shown in figure 6-1. As well, figure 6-2 displays AFM image of the Pt nanoparticles (*ca.* $4.3 \mu\text{g cm}^{-2}$) on a GC plate. As a consequence of the high surface roughness of the ITO plates (used in this work) it was impractical to perform reliable AFM of the Pt nanoparticles on them. Nevertheless, it was discussed previously (see section 4.3.1 for details) that the Pt nanoparticles form uneven structures on GC electrodes (both unmodified and modified), which appears quite

similar to that on an ITO plate. However, the SEM images (figure 6-1A and 6-1B) reveal that aggregation of the Pt nanoparticles on the ITO plate was somewhat more significant.

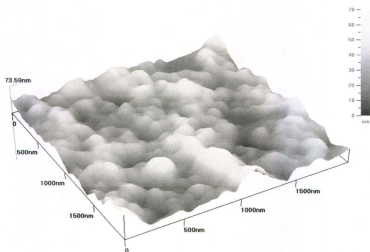


Figure 6-2. AFM ($2 \times 2 \mu\text{m} \times 74 \text{ nm}$) image of *ca.* $4.3 \mu\text{g cm}^{-2}$ of Pt nanoparticles + Nafion on GC.

Cyclic voltammograms of the Ru oxide, Sn oxide, and $\text{Ru}_{0.85}\text{Sn}_{0.15}$ oxide films (no Pt) in 0.1 M H_2SO_4 are shown in figure 6-3. The Ru containing electrodes, Ru oxide and $\text{Ru}_{0.85}\text{Sn}_{0.15}$ oxide, display larger background currents and substantially stronger signals than GC/Sn oxide. Voltammogram of the GC/Sn oxide electrode on the anodic sweep is mainly dominated by a broad oxidation peak centered at $\sim +0.5 \text{ V}$ followed by a rising current above $+0.75 \text{ V}$, both of which likely attributed to the oxidation of the Sn oxide layer, while a single reduction peak at $\sim +0.35 \text{ V}$, presumably the cathodic counterpart of

the anodic peak at +0.5 V, forms the only notable feature of the reverse sweep. The Ru oxide containing electrodes showed qualitatively similar features on both sweeps; however, their corresponding redox peaks were significantly stronger than those observed for the GC/Sn oxide electrode. Moreover, similar under peak areas of the Ru oxide and $\text{Ru}_{0.85}\text{Sn}_{0.15}$ oxide electrodes clearly shows that electrochemistry of the Ru oxide is dominant in both electrodes. This together with appreciably weaker signals of the GC/Sn oxide electrode is consistent with the relative loadings of Ru and Sn in these electrodes (see experimental for details).

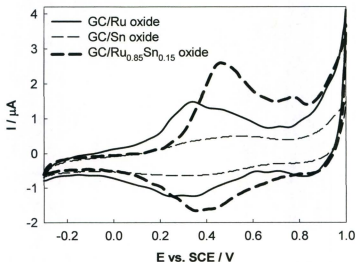


Figure 6-3. Cyclic voltammograms (10 mV s^{-1}) in $0.1 \text{ M H}_2\text{SO}_4$ of GC/Ru oxide, GC/Sn oxide and GC/ $\text{Ru}_{0.85}\text{Sn}_{0.15}$ oxide electrodes.

Figure 6-4 presents comparative cyclic voltammograms of the GC/Pt, ITO/Pt, GC/Ru oxide/Pt, GC/Sn oxide/Pt and GC/Ru_{0.85}Sn_{0.15} oxide/Pt electrodes in 0.1 M H₂SO₄. The forward scan (anodic) for the GC/Pt electrode begins with two peaks at -0.13 and -0.08 V assigned to hydrogen desorption, followed by the onset of Pt oxide (PtO) formation at ~ 0.4 V. A well-defined peak for PtO reduction can be seen at ca. 0.47 V on the reverse sweep, and hydrogen adsorption and hydrogen evolution signals appeared at E < -0.04 V, terminating the cathodic scan. Among the various oxide supports, ITO/Pt had a low background current and its voltammogram was most similar to that of GC/Pt. These features are generally similar for all the other electrodes. Nevertheless, the GC/Ru oxide/Pt, GC/Sn oxide/Pt, and particularly the GC/Ru_{0.85}Sn_{0.15} oxide/Pt show larger background currents, and the signals assigned to hydrogen desorption/adsorption were suppressed in some cases. To compare H electrochemistry on the various supports, electrochemical active areas for all the electrodes were estimated (see chapter 4, section 4.3) based on the H adsorption waves in figure 6-3. On this basis, ca. 0.078, 0.071, 0.055, 0.043, and 0.078 cm², respectively, were obtained for the GC/Pt, ITO/Pt, GC/Ru oxide/Pt, GC/Sn oxide/Pt and GC/Ru_{0.85}Sn_{0.15} oxide/Pt electrodes. These values correspond to electrochemical utilizations (active area/geometric area) ranging from 26% to 46%. However, these values would not show any meaningful trend, and as a result, cannot provide conclusive information about the effects of the various oxides on the H electrochemistry. Moreover, the differences could have originated from experimental uncertainties. In fact, we believe that the differences in the electrochemical active areas based on the H signals are less than the likely experimental uncertainties associated with

the employed preparation methods (e.g. drop coating as well as spontaneous deposition of the metal oxides). Comprehensive study of the effects of different supports (e.g. conducting polymers and various metal oxides) on the electrochemical active area of such Pt nanoparticles requires more focussed work. This would be worthwhile to be explored in future research.

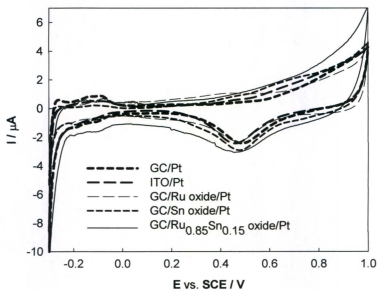


Figure 6-4. Cyclic voltammograms (10 mV s^{-1}) in $0.1 \text{ M H}_2\text{SO}_4$ of GC, ITO, GC/Ru oxide, GC/Sn oxide and GC/Ru_{0.85}Sn_{0.15} oxide electrodes coated with $4.3 \mu\text{g cm}^{-2}$ of Pt nanoparticles.

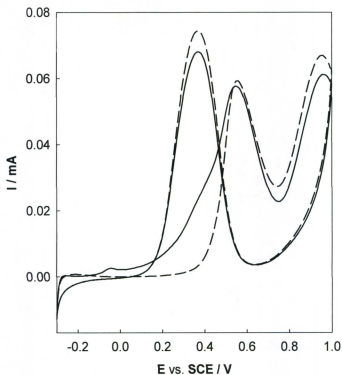


Figure 6-5. Cyclic voltammogram (10 mV s^{-1} ; 1st scan solid, 2nd scan dashed) in $0.1 \text{ M H}_2\text{SO}_4$ containing 0.2 M ethanol of a GC electrode coated with $4.3 \text{ } \mu\text{g cm}^{-2}$ of Pt nanoparticles.

6.3.2. Ethanol oxidation

For each electrode, cyclic voltammetry in the presence of ethanol was conducted immediately following the cyclic voltammetry in $0.1 \text{ M H}_2\text{SO}_4$ shown in figure 6-4. The electrode, initially at -0.3 V , was raised out of the electrolyte solution while ethanol was

added and then immersed into the mixed 0.1 M H₂SO₄ +0.2 M ethanol solution. A nitrogen atmosphere was maintained during this procedure which typically took *ca.* 30 s.

Figure 6-5 shows the first two CV scans of a GC/Pt electrode (4.3 μg cm⁻²) in the presence of 0.2 M ethanol. Inspection of the two scans on their forward legs reveals interesting features. The forward leg of the first scan shows a small wave at -0.05 V, which was followed by a 2nd oxidation onset at about 0 V. The sharp oxidation peak following the early onset at 0 V appears to consist of a very poorly-defined shoulder at about +0.38 preceding a peak at +0.56 V. The strong oxidation signal at +0.56 V is well-known to be, mainly, due to the oxidation of the adsorbed CO species (see section 5.3.3 for mechanistic discussion).^{18,19} The final stage of the first scan on the forward sweep is dominated by a sharp signal at *ca.* 0.95 V, presumably due to the direct oxidation of ethanol. The reverse scan of the first cycle consists of a large anodic peak at 0.37 V. On the second cycle, it is noteworthy that the early oxidation onset observed on the first scan (*ca.* at 0 V) shifted to a much higher value. Here on the forward scan, changes in the E_p and I_p of the dominant oxidation peak (at +0.56 V) were insignificant while the oxidation onset occurred at about +0.3 V, and the preceding shoulder at +0.38 had disappeared. Nevertheless, the original shape and E_p of the peak at +0.95 V were preserved in the second scan although its current increased slightly. The reverse sweep of the second cycle exhibited similar observations to that in the first cycle except for some increase for the current of the signal at +0.37 V. This peak which typically appears on the reverse leg of the oxidation of alcohols at Pt illustrates rapid oxidation of alcohol at the clean Pt produced by reduction of the Pt oxide layer formed at higher potentials.¹⁸

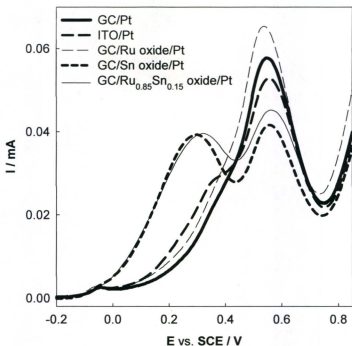


Figure 6-6. First anodic scans of cyclic voltammograms (10 mV s^{-1}) for GC/Pt, ITO/Pt, GC/Ru oxide/Pt, GC/Sn oxide/Pt and GC/Ru_{0.85}Sn_{0.15} oxide/Pt electrodes in 0.1 M H₂SO₄ containing 0.2 M ethanol.

Figure 6-6 displays the first forward scans for the GC/Pt, ITO/Pt, GC/Ru oxide/Pt, GC/Sn oxide/Pt and GC/Ru_{0.85}Sn_{0.15} oxide/Pt electrodes in 0.1 M H₂SO₄ in the presence of 0.2 M ethanol. The reverse scans were not notably influenced by the presence of the oxide layers and therefore are not presented here (see appendix, figures A-15 to A-19: multiple scan CVs for the GC/Pt, ITO/Pt, GC/Ru oxide/Pt, GC/Sn oxide/Pt and GC/

Ru_{0.85}Sn_{0.15} oxide/Pt electrodes). The electrodes show markedly different features over the voltammetric range. The voltammetric profiles are quite similar at their initial stages ($E < -0.05$ V), dominated by a small peak at -0.05 V. At $-0.05 < E < +0.4$ V, the GC/Sn oxide/Pt and GC/Ru_{0.85}Sn_{0.15} oxide/Pt electrodes were distinctly superior to the other electrodes. In fact, it seems that the small wave at -0.05 V for both the GC/Sn oxide/Pt and GC/Ru_{0.85}Sn_{0.15} oxide/Pt electrodes overlapped a rising current, leading to a large oxidation peak at *ca.* 0.3 V. The other Sn oxide-containing electrode, ITO/Pt, showed a small shoulder at $+0.38$ V, which together with the early oxidation peak for the GC/Sn oxide/Pt and GC/Ru_{0.85}Sn_{0.15} oxide/Pt electrodes points to the active role of Sn oxide over this region. In contrast, GC/Pt and GC/Ru oxide/Pt electrodes gave no significant features below $+0.4$ V. Therefore, one may record oxidation onsets of below -0.1 V for the GC/Sn oxide/Pt and GC/Ru_{0.85}Sn_{0.15} oxide/Pt electrodes, compared to *ca.* 0 V for the GC/Pt, ITO/Pt, GC/Ru oxide/Pt electrodes. The early onset for GC/Sn oxide/Pt and GC/Ru_{0.85}Sn_{0.15} oxide/Pt is appreciably lower than the values reported for Pt/C and PtRu/C ($> +0.3$ V vs. RHE $\sim +0.05$ V vs. SCE),²⁰ and comparable to a sophisticated ternary PtRhSnO₂/C catalyst ($> +0.1$ vs. RHE ~ -0.15 V vs. SCE).²¹

Nevertheless, a roughly inverse trend can be seen at $E > +0.4$ V, where the GC/Ru oxide/Pt electrode was somewhat better than GC/Pt, and both gave markedly superior activities to the other electrodes. Over this region, the ITO/Pt displayed intermediate performance (similar to its behaviour at below $+0.4$ V), and gave a significantly stronger signal at *ca.* $+0.55$ V than both the GC/Sn oxide/Pt and GC/Ru_{0.85}Sn_{0.15} oxide/Pt electrodes. For all cases, the dominant peak at $+0.55$ V can likely be ascribed to the

oxidation of ethanol to CO_2 through an adsorbed CO intermediate on the Pt nanoparticles (see section 5.3.3 for mechanism). The height of this peak indicates a rough inverse correlation with the onset of ethanol oxidation, with GC/Pt and GC/Ru oxide/Pt showing the highest currents in the region, while GC/Sn oxide/Pt and GC/Ru_{0.85}Sn_{0.15} oxide/Pt gave the lowest.

Second forward scans for the oxidation of ethanol at the GC/Pt, ITO/Pt, GC/Ru oxide/Pt, GC/Sn oxide/Pt and GC/Ru_{0.85}Sn_{0.15} oxide/Pt electrodes, shown in figure 6-7, depict remarkable changes. At $E < +0.4$ V, currents for all the electrodes showed remarkable decreases relative to the first forward scans. The most pronounced changes occurred with the GC/Sn oxide/Pt and GC/Ru_{0.85}Sn_{0.15} oxide/Pt electrodes, where the peak at *ca.* +0.3 V diminished to a weak shoulder on the main peak at +0.55 V. However, these two electrodes still displayed much better performances at $E < +0.4$ V compared to the other electrodes. At $E < +0.4$ V, the superior performances of the ITO/Pt, GC/Sn oxide/Pt and GC/Ru_{0.85}Sn_{0.15} oxide/Pt electrodes over GC/Pt and GC/Ru oxide/Pt were maintained over multi cycles (see figures A6-1 to A6-5). In this region, the current for the GC/Sn oxide/Pt electrodes continued to decrease significantly, while ITO/Pt showed relatively less decrease. At $E > +0.4$ V on the second scans, the GC/Ru oxide/Pt electrode was still superior to all the other electrodes, while the current for GC/Pt did not change noticeably compared to its first scan, and all the Sn oxide-containing electrodes showed appreciable increases in current with GC/Ru_{0.85}Sn_{0.15} oxide/Pt giving the largest increase.

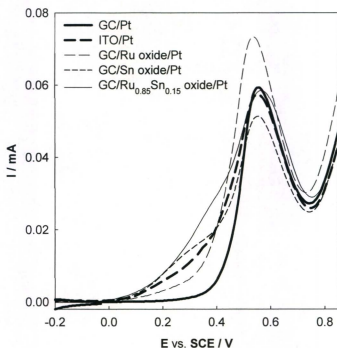


Figure 6-7. Second anodic scans of cyclic voltammograms (10 mV s^{-1}) for GC/Pt, ITO/Pt, GC/Ru oxide/Pt, GC/Sn oxide/Pt and GC/Ru_{0.85}Sn_{0.15} oxide/Pt electrodes in $0.1 \text{ M H}_2\text{SO}_4$ containing 0.2 M ethanol.

To further explore the effects of the various oxide supports, constant potential oxidation of ethanol at various potentials was conducted. A voltammogram of each electrode was obtained in $0.1 \text{ M H}_2\text{SO}_4$ prior to these experiments but, in order to preserve their initial activity, no voltammetry was performed in the presence of ethanol.

Thereafter, sequential chronoamperometry experiments were run at 0, +0.1, +0.2, +0.3, and +0.4 V.

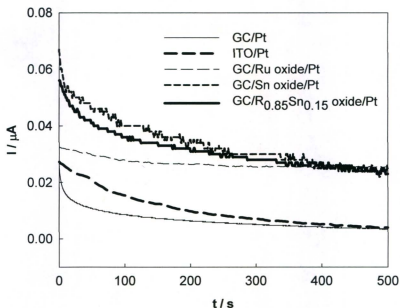


Figure 6-8. Chronoamperometry at 0 V for for GC/Pt, ITO/Pt, GC/Ru oxide/Pt, GC/Sn oxide/Pt and GC/Ru_{0.85}Sn_{0.15} oxide/Pt electrodes in 0.1 M H₂SO₄ containing 0.2 M ethanol.

Figure 6-8 shows chronoamperometry at 0 V for the GC/Pt, ITO/Pt, GC/Ru oxide/Pt, GC/Sn oxide/Pt and GC/Ru_{0.85}Sn_{0.15} oxide/Pt electrodes in the presence of 0.2 M ethanol. The initial activities of the GC/Pt and GC/Ru oxide/Pt electrodes were similar, while GC/Pt decayed rapidly at initial seconds and GC/Ru oxide/Pt showed a gradual decay over the 500 s timescale. In contrast, even though the initial current for the

ITO/Pt electrode was only slightly higher than GC/Ru oxide/Pt, it displayed a much more stable long term operation. The GC/Sn oxide/Pt and GC/Ru_{0.85}Sn_{0.15} oxide/Pt electrodes were substantially superior to all of the electrodes at the initial stages of the chronoamperometry (e.g. $t < 250$ s); however, as a consequence of their more rapidly decaying patterns, they showed quite similar activities to that of the ITO/Pt electrode at $t = 500$ s.

Constant potential oxidation of ethanol at the GC/Pt, ITO/Pt, GC/Ru oxide/Pt, GC/Sn oxide/Pt and GC/Ru_{0.85}Sn_{0.15} oxide/Pt electrodes was also studied at +0.1 V (figure 6-9). Consistent with the CVs shown in figures 6-6 and 6-7, all Sn oxide-containing electrodes gave higher currents than GC/Pt and GC/Ru oxide/Pt, with GC/Sn oxide/Pt displaying the best activity at this potential. The GC/Pt electrode initially gave a higher current than the GC/Ru oxide/Pt electrode but its current decayed more rapidly. This could be rationalized considering the well-known effect of Ru oxide in oxidative removal of the adsorbed CO species. It is discussed in section 6.3.3 that the main adsorbate for Pt-based catalysts in ethanol oxidation is $-\text{CO}_{\text{ads}}$ which can form a strong bond to Pt, and effectively hinder further adsorption of ethanol on the reaction sites. This can result in a significant decay in long term operation of such a system.

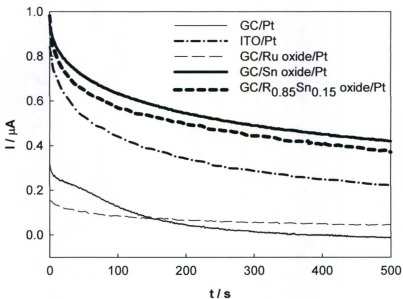


Figure 6-9. Chronoamperometry at +0.1 V for GC/Pt, ITO/Pt, GC/Ru oxide/Pt, GC/Sn oxide/Pt and GC/Ru_{0.85}Sn_{0.15} oxide/Pt electrodes in 0.1 M H₂SO₄ containing 0.2 M ethanol.

Figure 6-10 presents chronoamperometry at +0.2 V for the GC/Pt, ITO/Pt, GC/Ru oxide/Pt, GC/Sn oxide/Pt and GC/Ru_{0.85}Sn_{0.15} oxide/Pt electrodes in the presence of 0.2 M ethanol. The CA responses at this potential produced similar trend to those at +0.1 V, with the Sn oxide-containing electrodes giving superior activities over the 500 s timescale. However, while the GC/Sn oxide/Pt and GC/Ru_{0.85}Sn_{0.15} oxide/Pt electrodes initiated at comparable activities at $t = 0$, GC/Sn oxide/Pt decayed significantly more

rapidly particularly at short times. This could originate from the ability of Ru oxide in the oxidative removal of the adsorbed CO species.

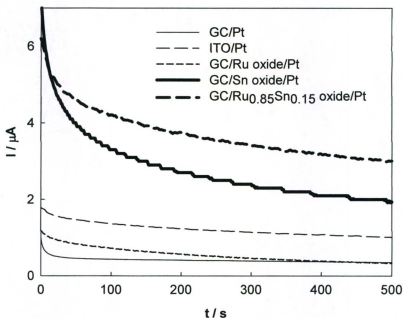


Figure 6-10. Chronoamperometry at +0.2 V for GC/Pt, ITO/Pt, GC/Ru oxide/Pt, GC/Sn oxide/Pt and GC/Ru_{0.85}Sn_{0.15} oxide/Pt electrodes in 0.1 M H₂SO₄ containing 0.2 M ethanol.

Similar to their CAs at +0.1 V, comparison of the GC/Pt and GC/Ru oxide/Pt electrodes at +0.2 V (figure 6-10) provides more evidence for the role of Ru oxide. That is, the GC/Ru oxide/Pt electrode gave a more significant current decrease over the 500 s than GC/Pt, its current decayed less rapidly at initial times ($t < 50$ s). Nevertheless, as the

comparative CVs in figures 6-6 and 6-7 suggested, while the ITO/Pt electrode was less active than the other two Sn oxide-containing electrodes (GC/Sn oxide/Pt and GC/Ru_{0.85}Sn_{0.15} oxide/Pt), it produced the most stable long term operation at 0, +0.1, and +0.2 V.

Even though chronoamperometric oxidation of ethanol at +0.3 V for the GC/Pt, ITO/Pt, GC/Ru oxide/Pt, GC/Sn oxide/Pt and GC/Ru_{0.85}Sn_{0.15} oxide/Pt electrodes (figure 6-11) further followed the same activity trend as at +0.1 and 0.2 V, it provided interesting insights into the significant role of Ru oxide. Herein, initial behaviours of the Ru oxide-containing electrodes (*e.g.* at $t < 150$ s) show that Ru oxide has an activation effect on ethanol oxidation at the Pt nanoparticles. This effect could be attributed to the well-known oxidative removal of the adsorbed intermediates, essentially CO, which were formed at lower potentials.

However, since the ITO/Pt electrode also showed a similar effect to some extent, even though the GC/Sn oxide/Pt electrode did not display such an effect, it would be uncertain to ascribe this feature solely to the effect of Ru oxide. Moreover, comparison of the two most active electrodes, GC/Sn oxide/Pt and GC/Ru_{0.85}Sn_{0.15} oxide/Pt, can further provide evidence for the mechanistic role of Ru oxide; while GC/Sn oxide/Pt gave a higher initial activity, its current decreased much more rapidly than did that of the GC/Ru_{0.85}Sn_{0.15} oxide/Pt electrode. In fact, the rates of decay for both GC/Ru oxide/Pt and GC/Ru_{0.85}Sn_{0.15} oxide/Pt electrodes were quite low, resulting in similar initial and final activities. Furthermore, consistent with the CVs and also CAs at lower potentials, ITO/Pt gave a very stable chronoamperometric pattern (long term operation) at +0.3 V.

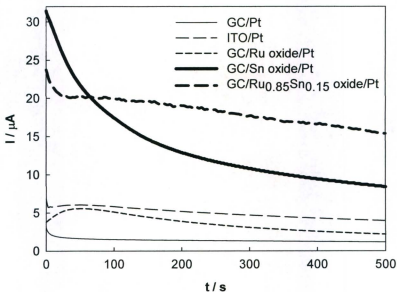


Figure 6-11. Chronoamperometry at +0.3 V for GC/Pt, ITO/Pt, GC/Ru oxide/Pt, GC/Sn oxide/Pt and GC/Ru_{0.85}Sn_{0.15} oxide/Pt electrodes in 0.1 M H₂SO₄ containing 0.2 M ethanol.

Figure 6-12 presents chronoamperometric profiles at a more positive potential of +0.4 V. Similar to the CAs at all other potentials and consistent with the CVs, the GC/Pt electrode gave the lowest activity at all times. For times less than *ca.* 150 s, the electrodes with oxide supports followed the same activity trend as they did at +0.1, +0.2, and +0.3 V. However, the GC/Sn oxide/Pt electrode gave the poorest long term activity, the current of which decayed much more rapidly. As such, the GC/Ru_{0.85}Sn_{0.15} oxide/Pt electrode also had a relatively high initial activity and its decay rate was lower than for

GC/Sn oxide/Pt, signifying the active role of Ru oxide at this potential to stabilize the CA pattern. The ITO/Pt electrode exhibited the lowest decay rate similar to its responses at lower potentials. Nevertheless, while GC/Ru oxide/Pt gave poorer initial current compared to the other single oxide-supported electrode, its decay rate was much lower than GC/Sn oxide/Pt, most likely indicative of the more stabilizing effect of the Ru oxide at high enough potentials.

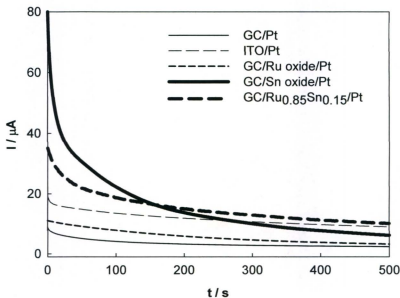


Figure 6-12. Chronoamperometry at +0.4 V for GC/Pt, ITO/Pt, GC/Ru oxide/Pt, GC/Sn oxide/Pt and GC/Ru_{0.85}Sn_{0.15} oxide/Pt electrodes in 0.1 M H₂SO₄ containing 0.2 M ethanol.

6.3.3. Mechanistic insights

As discussed in section 1.1.2.4, adsorption and dehydrogenation of ethanol at Pt (reactions 6-1 and 6-2) yield Pt-O-CH₂CH₃ and/or Pt-CH(OH)CH₃, which can further be dissociated to a mixture of -CH_x and oxygen containing species (reactions 6-3 and 6-4).²²⁻²⁵



Both the adsorbed Pt-CH_x and Pt-CH_yO type species can be further oxidized to adsorbed CO (e.g. reaction 6-5) and then to CO₂ (reaction 6-6).



The oxidative adsorption of ethanol at Pt is generally followed by *in situ* vibrational spectroscopy,²⁵ usually by monitoring the adsorbed CO produced by reactions such as 6-5. Complementary information can be obtained by measuring the CO₂ produced by oxidative stripping of adsorbates by differential electrochemical mass spectrometry (DEMS),²⁴ and from quantum chemistry calculations²⁶. The oxidative adsorption of ethanol on Pt can be completely suppressed by underpotentially deposited hydrogen at low potentials (e.g. 0.06 V vs. RHE²⁴), but produces substantial coverages of CO and other adsorbates at higher potentials.^{22, 24, 25} Oxidation of these adsorbates to CO₂ begins at ca. 0.5 V vs. RHE (~ 0.25 V vs. SCE),²⁴ which coincides approximately with a

decrease in the intensity of the vibrational response due to adsorbed CO.^{22, 25} However, the amount of CO₂ produced corresponds to $\leq 60\%$ of a CO monolayer, indicating the presence of other adsorbates that can not readily be oxidized. For the adsorbed species that are oxidized to CO₂, 2.2-5.9 electrons are involved per CO₂ molecule, depending on the adsorption and stripping potentials.²⁴ This indicates that various oxidizable Pt-CH_x and Pt-CH₂O species are formed during the oxidative adsorption of ethanol on Pt.

Formation of different types of adsorbates during the first and subsequent scans can account for the changes in the voltammograms shown in figures 6-5 through 6-7. A diverse range of one and two carbon adsorbates could form on the clean surface of Pt at the beginning of the first scan. The disappearance/decrease of the voltammetric features at $E < +0.4$ V on the second scan could originate from formation of the strongly adsorbed CO at Pt sites. This hypothesis can also explain the meaningful increase in the CO oxidation peak at +0.55 V on the second scans, typically, for all the oxide-supported electrodes. It is noteworthy that this peak did not increase with cycling for the GC/Pt electrode. As a matter of fact, the dominant species at the Pt sites for the GC/Pt electrode could be Pt-CO, the population of which did not change significantly with cycling. In contrast, for all other oxide-supported electrodes, the CO oxidation peak increased from the first scan to the second, while it remained somewhat unchanged in subsequent cycles.

The small peak seen at *ca.* -0.05 V on the first scan for all electrodes may be due to adsorbed H, while the broad shoulders are presumably due to the oxidation of species such as Pt-O-CH₂CH₃, Pt-CH(OH)CH₃, Pt-CH₃ and Pt-CH₂O formed during the oxidative adsorption of ethanol at the Pt nanoparticles. However, the GC/Pt electrode

obviously showed somewhat weaker activity at the early region ($< +0.4$ V). Wang *et al.*²⁰ suggested that the oxidative adsorption of ethanol at pure Pt does not occur extensively since pure Pt is a better host for underpotentially deposited hydrogen (H_{UPD}). Therefore, pure Pt is more vulnerable to be blocked by the H_{UPD} at very early potentials (e.g. $+0.06$ V vs. RHE). Similarly, the adsorbed CO, forming as the dominant adsorbate during the cathodic sweep of the first scan (*i.e.* during the anodic peak on the reverse scan for all electrodes), can considerably prohibit adsorption of ethanol. Therefore, the broad shoulder seen on the first scans of all the electrodes disappeared since Pt-O-CH₂CH₃, Pt-CH(OH)CH₃, Pt-CH₃ and Pt-CH₂O no longer formed at the beginning of the second scan. The fact that the broad shoulder prior to the $+0.55$ V peak persists to varying extents for the ITO/Pt, GC/Ru oxide/Pt, GC/Sn oxide/Pt and GC/Ru_{0.85}Sn_{0.15} oxide/Pt electrodes (figure 6-7) indicates that the oxide supports facilitate the oxidation of adsorbed CO and/or may play other roles in promoting ethanol oxidation.

Consistent with the well known bifunctional mechanism for CO oxidation at Pt-Ru systems, Ru oxide should accelerate ethanol oxidation through its active role in the oxidative removal of the adsorbed CO, reaction 6-7.



Since Ru-OH forms at lower potentials than Pt-OH, reaction 6-7 occurs at lower potentials than reaction 6-6. It has been previously demonstrated that this occurs for methanol oxidation at GC/Ru oxide/Pt electrodes, where the predominant adsorbate is CO.¹⁶ The shift in the oxidation wave in figure 6-7 for GC/Ru oxide/Pt relative to GC/Pt

is similar to that seen for methanol oxidation, suggesting a similar mechanistic role for the Ru oxide support.

The first scans of the two Sn-supported electrodes, GC/Ru_{0.85}Sn_{0.15} oxide/Pt and GC/Sn oxide/Pt show essentially similar results suggesting a negligible contribution of Ru oxide up to 0.4 V. This is consistent with the fact that GC/Ru oxide/Pt is not significantly superior to GC/Pt up to +0.4 V. However, GC/Ru_{0.85}Sn_{0.15} oxide/Pt is slightly better than GC/Sn oxide/Pt at potentials higher than +0.4 V again consistent with the effectiveness of Ru oxide on the oxidation of CO and/or ethanol at higher potentials. Inspection of the voltammograms of the GC/Ru oxide/Pt electrode at potentials above +0.4 V, where it gives the highest activity, further supports promotional effect of Ru oxide in this region. Moreover, comparison of the second scans of the GC/Ru_{0.85}Sn_{0.15} oxide/Pt and GC/Sn oxide/Pt electrodes provides additional evidence for the effects of Ru oxide at potentials above +0.3 V. GC/Ru_{0.85}Sn_{0.15} oxide/Pt is considerably superior to GC/Sn oxide/Pt.

For ethanol oxidation, it has been reported that PtSn is more effective than PtRu at low potentials while PtRu becomes more effective at higher potentials.^{27, 28} The results shown in figures 6-7, 6-9 and 6-10 are consistent with this, with the GC/Ru oxide/Pt electrode showing the largest currents at potentials above *ca.* 0.4 V (figure 6-6), but all of the Sn oxide-containing electrodes being more effective at 0.4 V and lower. Although we cannot yet provide a full explanation of these results, it does appear that the electronic effect of Sn oxide containing supports contributes to the removal of CO_{ads} at lower potentials than the bifunctional effect of the Ru oxide support. In terms of initial activity

at low potentials, the pure Sn oxide support was better than either of the mixed oxides, which can reasonably be attributed to the higher Sn concentration at the Pt surface. However, Antolini *et al.*⁸ proposed that for ternary systems of PtSnRu, Pt tends to interact with Ru and not with Sn (*e.g.* through a bifunctional mechanism) in the presence of high loadings of Ru. However, in our system, even though the pure Sn oxide support showed appreciably higher initial activities than all other oxide-supported catalysts, its long term performance was inferior to either of the mixed oxides electrodes (ITO/Pt and GC/Ru_{0.85}Sn_{0.15} oxide/Pt). This may suggest that the presence of either In or Ru oxide significantly stabilizes the performance at potentials above *ca.* 0.1 V (see figures 6-10 through 6-12), and makes ITO and Ru_xSn_{x-1} oxide supports attractive for further investigation.

Finally, it is necessary to consider how the oxide supports employed here are able to induce similar bifunctional and electronic effects to those previously documented for PtM alloys and mixed Pt + M oxide catalysts. The bifunctional effects are addressed by work on systems in which the distance between catalyst pairs has been experimentally controlled. For example, Abruna and coworkers were able to demonstrate "electrocatalytic synergy" in the oxidation of CO between an Ru scanning tunnelling microscopy tip and a Pt substrate, via the bifunctional mechanism shown in reaction 6-7.²⁹ CO adsorbed on the Pt was oxidized at lower overpotentials when the Ru tip was brought close to its surface, with density functional theory calculations indicating that a critical distance of less than *ca.* 0.4 nm would be required for reaction 6-7 to occur. Sustained CO oxidation currents were observed due to surface diffusion of CO to the Ru

tip. It is clear from these results that bifunctional oxidation of adsorbed CO on Pt nanoparticles will occur in a sustained fashion whenever there is contact (or even very close proximity) between any regions of the particles and a suitable metal oxide, regardless of whether the oxide is deposited onto the particles³⁰ or whether the particles are deposited on a metal oxide support. In addition, it is possible for particles of two different metals (or an oxide and a metal), such as Pt and Ru, in close proximity to exhibit synergistic effects due to chemical transfer of metal atoms via dissolution and redeposition.³¹

Electronic effects between oxide supports and Pt nanoparticles have been extensively investigated.^{32, 33} For example, in the case of Pt on TiO₂ partial charge transfer from the substrate to Pt has been observed by X-ray photoelectron spectroscopy, which was correlated to increased activity to oxygen reduction.³² In another paper, Miecznikowski and Kulesza reported³³ enhanced ethanol oxidation at a binary catalyst of PtSn nanoparticles supported on WO₃, and ascribed the promotional effects to the stabilizing properties of the W oxide support. Undoubtedly, study of the interaction between various metal oxide supports and catalysts in the oxidation of important organic fuels, such as ethanol, can provide insight into the development of more efficient catalysts, which is a centre of attention in fuel cell technology.

6.4. Concluding remarks

Sn, Ru, and RuSn oxide-modified GC electrodes and a commercial indium-tin oxide plate were compared, as supports, with unmodified GC in the oxidation of ethanol

at preformed Pt nanoparticles. In this regard, the recently developed drop coating method was used to prepare catalysts. This method allows for preparation of layered (*i.e.* insignificant mixing of the support and catalyst layers) rather than mixed structures (*e.g.* alloys), in order to study pure support effects. Voltammetric oxidation of ethanol at these catalysts showed that all the metal oxide-supported electrodes exhibited strong support effects. The Sn oxide-containing electrodes gave higher currents at low potentials ($< +0.4$ V), while GC/Pt and GC/Ru oxide/Pt (and ITO/Pt to some extent) were superior at higher potentials ($> +0.4$ V). As well, chronoamperometry was used to explore long term operation of the electrodes. Therein, it was found that the presence of Ru oxide decreased the rate of decay, while Sn oxide increased activity significantly. Furthermore, comparison of the mixed oxide-supported electrodes with their single oxide counterparts suggests that the promotional effects of the Sn oxide in the presence of a second metal oxide (either Ru or In oxide) decreased, although the long term performance improved in both cases. Finally, on the basis of the electrochemical observations, new mechanistic insights were obtained. It is proposed that Ru oxide promotes the reaction through a bifunctional mechanism, in sharp contrast to the prevailing electronic (ligand) effects for Sn oxide and mixed oxides containing Sn.

References

1. E. Antolini, *J. Power Sources*, 2007, **170**, 1-12.
2. C. Coutanceau, S. Brimaud, C. Lamy, J. M. Leger, L. Dubau, S. Rousseau and F. Vigier, *Electrochim. Acta*, 2008, **53**, 6865-6880.
3. X. Yu and P. G. Pickup, *J. Power Sources*, 2008, **182**, 124-132.
4. X. Zhao, M. Yin, L. Ma, L. Liang, C. Liu, J. Liao, T. Lu and W. Xing, *Energy Environ. Sci.*, 2011, **4**, 2736-2753.
5. S. Rousseau, C. Coutanceau, C. Lamy and J. M. Leger, *J. Power Sources*, 2006, **158**, 18-24.
6. G. Li and P. G. Pickup, *J. Power Sources*, 2007, **173**, 121-129.
7. X. Zhang, H. Zhu, Z. Guo, Y. Wei and F. Wang, *J. Power Sources*, 2011, **196**, 3048-3053.
8. E. Antolini, F. Colmati and E. R. Gonzalez, *Electrochem. Commun.*, 2007, **9**, 398-404.
9. A. Ghumman, G. Li, D. V. Bennett and P. G. Pickup, *J. Power Sources*, 2009, **194**, 286-290.
10. H. Wang, Z. Jusys and R. J. Behm, *J. Power Sources*, 2006, **154**, 351-359.
11. F. Vigier, S. Rousseau, C. Coutanceau, J.-M. Leger and C. Lamy, *Top. Catal.*, 2006, **40**, 111-121.
12. E. M. Cunha, J. Ribeiro, K. B. Kokoh and A. R. de Andrade, *Int. J. Hydrogen Energy*, 2011, **36**, 11034-11042.

13. A. Kowal, M. Li, M. Shao, K. Sasaki, M. B. Vukmirovic, J. Zhang, N. S. Marinkovic, P. Liu, A. I. Frenkel and R. R. Adzic, *Nat Mater*, 2009, **8**, 325-330.
14. C. Lamy, A. Lima, V. LeRhun, F. Delime, C. Coutanceau and J.-M. Leger, *J. Power Sources*, 2002, **105**, 283-296.
15. R. B. Moghaddam and P. G. Pickup, *Electrocatalysis*, 2011, **2**, 159-162.
16. R. B. Moghaddam and P. G. Pickup, *Electrochem. Commun.*, 2011, **13**, 704-706.
17. J. Yang, J. Y. Lee and H. P. Too, *Anal. Chim. Acta*, 2006, **571**, 206-210.
18. J. Jiang and A. Kucernak, *J. Electroanal. Chem.*, 2005, **576**, 223-236.
19. P. Inkaew, W. Zhou and C. Korzeniewski, *J. Electroanal. Chem.*, 2008, **614**, 93-100.
20. Q. Wang, G. Q. Sun, L. H. Jiang, Q. Xin, S. G. Sun, Y. X. Jiang, S. P. Chen, Z. Jusys and R. J. Behm, *PCCP*, 2007, **9**.
21. M. Li, A. Kowal, K. Sasaki, N. Marinkovic, D. Su, E. Korach, P. Liu and R. R. Adzic, *Electrochim. Acta*, 2010, **55**, 4331-4338.
22. F. Vigier, C. Coutanceau, A. Perrard, E. M. Belgsir and C. Lamy, *J. Appl. Electrochem.*, 2004, **34**, 439-446.
23. K. B. Kokoh, F. Hahn, E. M. Belgsir, C. Lamy, A. R. de Andrade, P. Olivi, A. J. Motheo and G. Tremiliosi-Filho, *Electrochim. Acta*, 2004, **49**, 2077-2083.
24. H. Wang, Z. Jusys and R. J. Behm, *Fuel Cells*, 2004, **4**, 113-125.
25. R. B. Kutz, B. Braunschweig, P. Mukherjee, R. L. Behrens, D. D. Dlott and A. Wieckowski, *J. Catal.*, 2011, **278**, 181-188.
26. H.-F. Wang and Z.-P. Liu, *J. Am. Chem. Soc.*, 2008, **130**, 10996-11004.

27. W. J. Zhou, B. Zhou, W. Z. Li, Z. H. Zhou, S. Q. Song, G. Q. Sun, Q. Xin, S. Douvartzides, M. Goula and P. Tsiakaras, *J. Power Sources*, 2004, **126**, 16-22.
28. H. Li, G. Sun, L. Cao, L. Jiang and Q. Xin, *Electrochim. Acta*, 2007, **52**, 6622-6629.
29. L. Zhuang, J. Jin and H. D. Abruna, *J. Am. Chem. Soc.*, 2007, **129**, 11033-11035.
30. W.-P. Zhou, S. Axnanda, M. G. White, R. R. Adzic and J. Hrbek, *J. Phys. Chem. C*, 2011, **115**, 16467-16473.
31. B. Wickman, Y. E. Seidel, Z. Jusys, B. Kasemo and R. J. Behm, *ACS Nano*, 2011, **5**, 2547-2558.
32. A. Lewera, L. Timperman, A. Roguska and N. Alonso-Vante, *The Journal of Physical Chemistry C*, 2011, **115**, 20153-20159.
33. K. Miecznikowski and P. J. Kulesza, *J. Power Sources*, 2010, **196**, 2595-2601.

Chapter 7

Summary

Chapter 7. Summary

The first approach of this thesis (chapter 2) demonstrates the significance of electrochemical impedance spectroscopy (EIS) for probing the polymerization of pyrrole on a porous carbon black (CB) support. For example, for a potentiodynamic deposition regime, it was found that the polymerization initially occurred evenly all over the CB structure, after which it continued mainly on top of the CB layer. Furthermore, EIS was also employed to characterize the properties and structures of carbon black/polypyrrole (PPCB) composites prepared under different polymerization conditions. Potential-controlled polymerizations (i.e. potentiodynamic and potentiostatic) led to formation of PPCB films with large particle sizes and high resistances, while a slow galvanostatic polymerization resulted in PPCB composites with highly homogeneous structures and very low resistances. This study is important for designing polypyrrole-modified supports/materials for use in energy conversion devices such as fuel cells and capacitors, and can also be used as a guideline for preparing composites of other conducting polymers with various porous carbon structures.

In the second approach (chapter 3), we developed extended reaction zone (i.e. 3-dimensional electrodes) anode catalysts for formic acid oxidation. In consideration of the high conductivity and stability of polyaniline (PANI) over the useful operation potential of a formic acid fuel cell (i.e. ~ -0.1 to $+0.1$ V vs. SCE), this conducting polymer was chosen as a support for incorporation of Pd, which is the most active catalyst for formic acid (FA) oxidation. Therein, spontaneous deposition of Pd onto carbon fiber paper polymerized with PANI under potentiodynamic, potentiostatic, and galvanostatic

conditions produced CFP/PD-PANI/Pd_{SP}, CFP/P-PANI/Pd_{SP} and CFP/G-PANI/Pd_{SP} electrodes, respectively. CFP/G-PANI/Pd_{SP} and CFP/PD-PANI/Pd_{SP} showed the highest and lowest activities while CFP/P-PANI/Pd_{SP} gave intermediate results. Impedance studies on the PANI supports showed that CFP/PD-PANI, CFP/P-PANI, and CFP/G-PANI all had low resistances at +0.1 V suggesting that these polymers should be conductive at this potential. Furthermore, transmission electron microscopy gave the smallest Pd particle size for CFP/PD-PANI/Pd suggesting that this composite should be more active than the other two in FA oxidation. However, inspection of the impedance behaviours of the CFP/PANI supports at slightly negative potentials (e.g. -0.1 V) unveiled the source of the remarkable differences in FA oxidation activities of the resulting CFP/PANI/Pd composites. On this basis, it can be proposed that the low conductivity of CFP/PD-PANI at low potentials could have been detrimental in two ways: 1) formation of a poorly structured CFP/PD-PANI/Pd composite since the spontaneous deposition of Pd was performed at a reduced CFP/PD-PANI film; 2) the high resistance of the CFP/PD-PANI at -0.1 V is coincidental to the FA oxidation onset observed in the cyclic voltammograms.

The final parts of this thesis are focussed on the oxidation of methanol (chapter 4), formic acid (chapter 5), and ethanol (chapter 6) at preformed Pt or Pd nanoparticles drop coated at various PANI and metal oxide (MO) modified glassy carbon (GC) electrodes. In fact, we aimed at observation of support effects (i.e. synergetic as opposed to the possible promotional effects of structure, distribution, etc.) through depositing thin support layers on GC, and use of preformed catalyst particles that can be physically

applied on those supports. In this way, diffusion of the catalyst particles into the supports will be negligible and formation of layered structures can be expected. For methanol oxidation at Pt, Ru oxide modified GC (GC/Ru oxide) showed a very clear effect, which was presumably due to the well-known bifunctional mechanism (i.e. promotion of the oxidation of $-\text{CO}_{\text{ads}}$ species in the presence of Ru-OH at lower potential compared to an unmodified GC), while a PANI modified GC did not significantly contribute to the reaction at Pt. In contrast, adoption of this facile method to formic acid oxidation at Pd showed that the same PANI support (made in H_2SO_4) dramatically promoted the reaction; furthermore, we electrodeposited PANI at GC in two other media (CF_3COOH and $\text{CF}_3\text{SO}_3\text{H}$) to assess the validity of the results. Taking into account their lower oxidation onsets as well as substantially higher currents than GC/Pd, it can be unambiguously concluded that all the PANI supports had strong synergy for FA oxidation at Pd. Moreover, normalizing chronoamperometric FA oxidation at these supports and at an unmodified GC electrode drop coated with Pd showed that all PANI supported Pd electrodes had superior long term performances than GC/Pd. Having these results in hand, we extended this method to ethanol oxidation at Pt, which is a more complicated catalytic system. Therein, various MO modified supports were compared with an unmodified GC electrode. It was found that all the oxide supported Pt electrodes gave superior activities to GC/Pt, with Sn oxide containing electrodes being substantially active at low potentials (e.g. $< +0.4$ V vs. SCE) and Ru oxide containing electrodes giving superior results at higher potentials. Additionally, new mechanistic insights were

obtained, based on which we suggested that the effect of Sn oxide on ethanol oxidation at Pt is electronic while Ru oxide acts in a mechanistic fashion.

The fundamental and primary results of this thesis can be used as starting points for more sophisticated studies. In this respect, we may provide a list of the research topics that are either currently under investigation or being planned for future work:

1. Investigation of the structural evolution for the polymerization of aniline on various high surface area carbonaceous supports (e.g. carbon black) in order to obtain carbon-PANI (CB/PANI) composites that possess large area/volume ratio, stability, and good electronic/ionic conductivity. These composites can be used as support materials for incorporation of catalyst particles for the oxidation of organic fuels.
2. Mass production of carbonaceous materials modified with various MO (e.g. Ru oxide or Sn oxide) and supporting catalyst particles to be used in the anodes of alcohol fuel cells. As an instance, we prepared Ru oxide modified CB and chemically loaded it with Pt nanoparticles (particle size ~ 5 nm). This CB/Ru oxide/Pt composite gave appreciably superior results to a commercial PtRu/C powder in methanol oxidation. Furthermore, in the light of the results obtained in chapter 6 for ethanol oxidation at GC/RuSn oxide/Pt, mass production of CB/RuSn oxide/Pt composites for use in direct ethanol fuel cell (DEFC) was performed in collaboration with another group member (David James), who is currently extending the approach.
3. Mechanistic studies are of high importance in fuel cell technology since they can provide valuable insights into the development of more active catalysts. Techniques such as surface enhanced infrared absorption spectroscopy (SEIRA),¹ online analysis of

products,² and differential electrochemical mass spectrometry (DEMS)³ are suitable tools for this purpose. Using SEIRA, the effects of various PANI supports on the mechanism of formic acid oxidation at Pd nanoparticles are being explored in our group. This can further be extended to methanol and ethanol oxidation at Pt.

References

1. A. M. Hofstead-Duffy, D.-J. Chen, S.-G. Sun and Y. J. Tong, *J. Mater. Chem.*, 2012, **22**, 5205-5208.
2. A. Ghumman, G. Li, D. V. Bennett and P. G. Pickup, *J. Power Sources*, 2009, **194**, 286-290.
3. F. A. Viva, M. M. Bruno, M. Jobbagy and H. R. Corti, *J. Phys. Chem. C*, 2012, **116**, 4097-4104.

Appendix

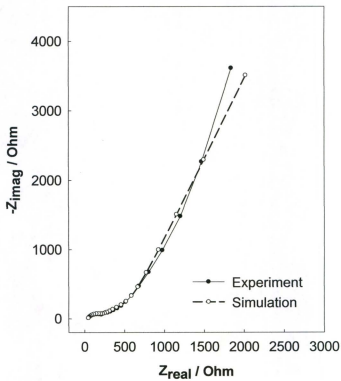


Figure A-1. Comparison of experimental and simulated (ZView2, Scribner Associates Inc.) impedance data for PPCB-cv2 at -0.1 V.

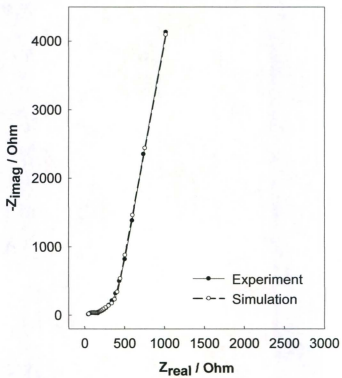


Figure A-2. Comparison of experimental and simulated (ZView2, Scribner Associates Inc.) impedance data for PPCB-cv2 at +0.3 V.

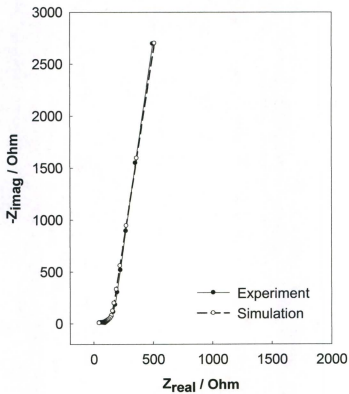


Figure A-3. Comparison of experimental and simulated (ZView2, Scribner Associates Inc.) impedance data for PPCB-cv4 at +0.3 V.

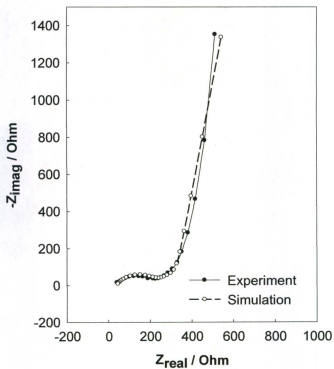


Figure A-4. Comparison of experimental and simulated (ZView2, Scribner Associates Inc.) impedance data for PPCB-cv6 at -0.1 V.

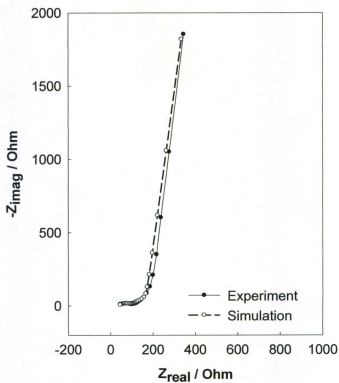


Figure A-5. Comparison of experimental and simulated (ZView2, Scribner Associates Inc.) impedance data for PPCB-cv6 at +0.3 V.

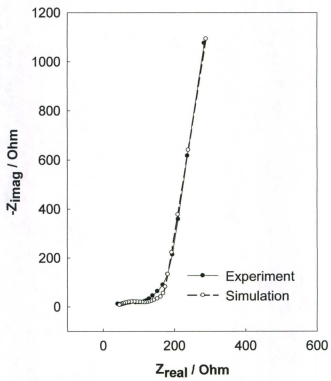


Figure A-6. Comparison of experimental and simulated (ZView2, Scribner Associates Inc.) impedance data for PPCB-cv8 at -0.1 V.

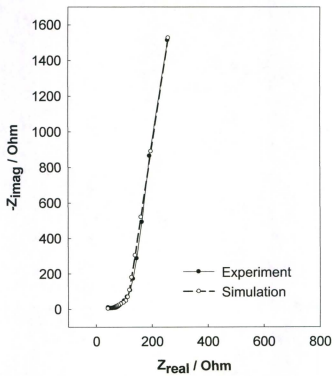


Figure A-7. Comparison of experimental and simulated (ZView2, Scribner Associates Inc.) impedance data for PPCB-cv8 at +0.3 V.

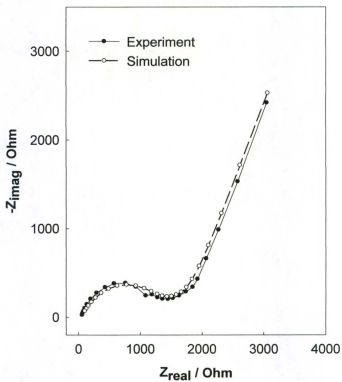


Figure A-8. Comparison of experimental and simulated (ZView2, Scribner Associates Inc.) impedance data for PPCB-cp at -0.3 V.

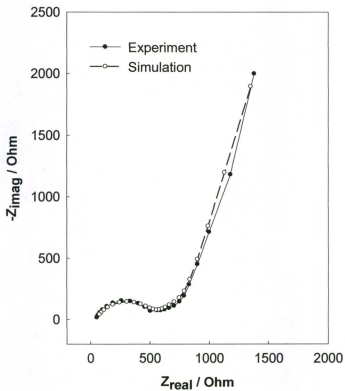


Figure A-9. Comparison of experimental and simulated (ZView2, Scribner Associates Inc.) impedance data for PPCB-cp at -0.1 V.

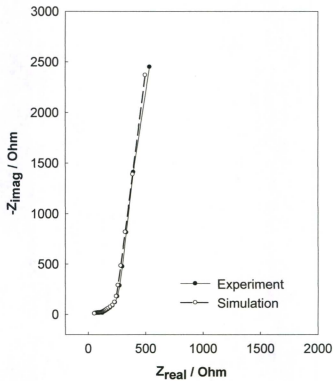


Figure A-10. Comparison of experimental and simulated (ZView2, Scribner Associates Inc.) impedance data for PPCB-cp at +0.3 V.

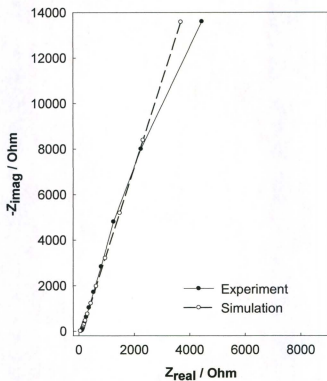


Figure A-11. Comparison of experimental and simulated (ZView2, Scribner Associates Inc.) impedance data for PPCB-cc2 at -0.5 V.

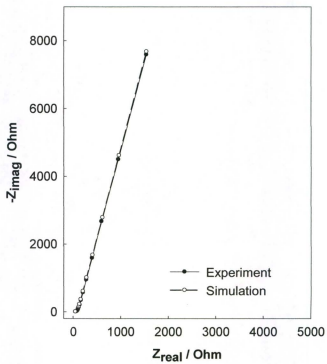


Figure A-12. Comparison of experimental and simulated (ZView2, Scribner Associates Inc.) impedance data for PPCB-cc2 at -0.3 V.

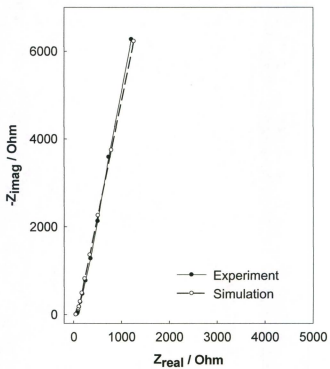


Figure A-13. Comparison of experimental and simulated (ZView2, Scribner Associates Inc.) impedance data for PPCB-cc2 at -0.1 V.

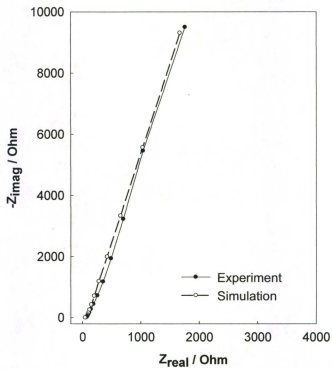


Figure A-14. Comparison of experimental and simulated (ZView2, Scribner Associates Inc.) impedance data for PPCB-cc2 at +0.3 V.

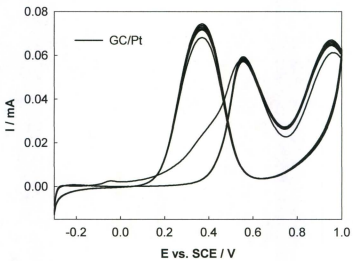


Figure A-15. Multiple scan CVs (10 mV s^{-1}) for a GC/Pt electrode in $0.1 \text{ M H}_2\text{SO}_4$ containing 0.2 M ethanol.

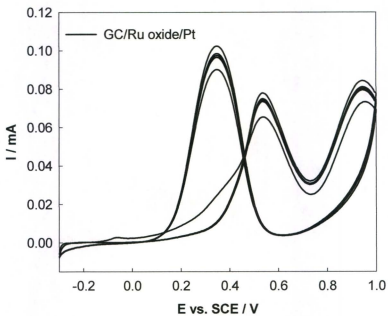


Figure A-16. Multiple scan CVs (10 mV s^{-1}) for a GC/Ru oxide/Pt electrode in 0.1 M H_2SO_4 containing 0.2 M ethanol.

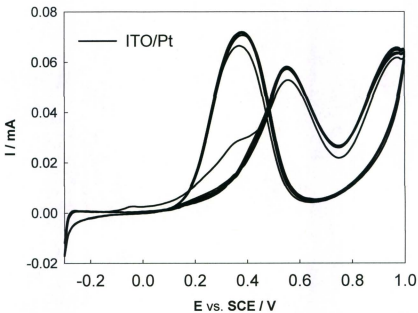


Figure A-17. Multiple scan CVs (10 mV s^{-1}) for an ITO/Pt electrode in $0.1 \text{ M H}_2\text{SO}_4$ containing 0.2 M ethanol.

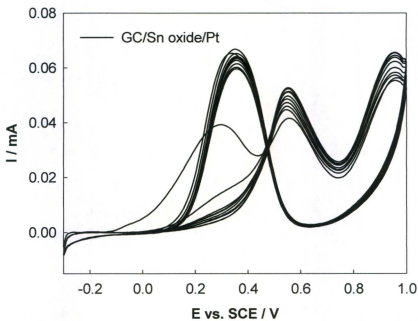


Figure A-18. Multiple scan CVs (10 mV s^{-1}) for a GC/Sn oxide/Pt electrode in 0.1 M H_2SO_4 containing 0.2 M ethanol.

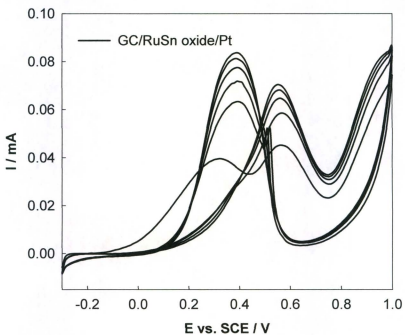


Figure A-19. Multiple scan CVs (10 mV s^{-1}) for a GC/Ru_{0.85}Sn_{0.15} oxide/Pt electrode in 0.1 M H₂SO₄ containing 0.2 M ethanol.



